Amorphous Silicon for the Application in Integrated Optics

Vom Promotionsausschuss der
Technischen Universität Hamburg-Harburg
zur Erlangung des akademischen Grades
Doktor-Ingenieur (Dr.-Ing.)
genehmigte Dissertation

von

Alexander Harke

aus Hannover

2010

1. Gutachter: Prof. Dr. Jörg Müller
2. Gutachter: Prof. Dr. Ernst Brinkmeyer

Tag der mündlichen Prüfung: 15. Februar 2010

URN: urn:nbn:de:gbv:830-tubdok-8670

Danksagung

Diese Arbeit entstand im Rahmen meiner Tätigkeit als wissenschaftlicher Mitarbeiter am Institut für Mikrosystemtechnik der Technischen Universität Hamburg-Harburg. Bei dem Leiter dieses Institutes, Herrn Prof. Dr. Jörg Müller, möchte ich mich herzlich für die vielseitige und spannende Aufgabenstellung bedanken. Durch seinen Reichtum an Ideen und Erfahrung hat er immer wieder neue Impulse für diese Arbeit gegeben.
Allen ehemaligen Kollegen, insbesondere Herrn Marc Schober, Frau Julia Amthor, Herrn Oliver Horn, Herrn Gerrit Schoer und Frau Krassimira Koleva, möchte ich für die angenehme Arbeitsatmosphäre danken. Herrn Balaji Ponnam und Herrn Timo Lipka danke ich für die wertvollen Beiträge durch Ihre Studien- und Diplomarbeiten und wünsche Herrn Lipka viel Erfolg bei der Fortführung der Forschungsarbeiten.
Ebenfalls bedanken möchte ich mich bei Herrn Prof. Dr. Ernst Brinkmeyer für die Übernahme des Korreferats. Auch allen Mitarbeitern des Instituts optische Kommunikationstechnik, insbesondere Herrn Dr. Michael Krause, möchte ich an dieser Stelle für Ihre Unterstützung, die hilfreichen Diskussionen und die fruchtbare Zusammenarbeit in den gemeinsamen Projekten danken.
Für die Raman - Spektroskopie und die Zusammenarbeit danke ich Herrn Dr. Josef Kovacs und Herrn Jan Hampe vom Institut für optische und elektronische Materialien. Herrn Stefan Hansen vom Institut für Mikroproduktionstechnik der Universität Hannover danke ich für die Durchführung der Planarisierungsprozesse.
Abschließend gilt mein besonderer Dank auch meiner Familie, insbesondere meiner Frau Hai Lin, für das Verständnis und die Unterstützung.

Alexander Harke
Hamburg, Februar 2010

Contents

Chapter 1

Introduction

Amorphous silicon, as well as amorphous silicon alloys are already being used in many applications, mainly utilizing the possibility of fabricating large area thin films with sufficient semiconducting properties. These applications include photovoltaic cells, TFT-displays or photocopiers. Decades of research have been dedicated to the understanding of the electronic properties resulting from atomic order, doping, as well as the unique role of hydrogen in this material.
The structural disorder results in high electron scattering, band-tails with localized states and defects. Bound hydrogen, as it is present e.g. in plasma deposited material from SiH_4 precursor gas, saturates dangling bonds of silicon and effectively reduces defect density. It is responsible for even more phenomena, which differentiate hydrogenated amorphous silicon (a-Si:H) from crystalline silicon (c-Si), and finally allows the fabrication of an amorphous material with still reasonable electrical as well as (being in focus of this work) optical properties.
Recently, with the thriving of silicon photonics, a new field of possible application for a-Si:H has been opened up. Several reasons can be given for the upcoming of silicon photonics.
While some pioneering works in this field go back to the early 90th [1], it is only now, due to the enormous progress in lithography, that cost effective integration of compact optical waveguides from SOI is feasible. On top of that, the demonstration of GHz-modulation of infrared light in silicon using the free carrier plasma effect in an MOS-structure [2] represents an important breakthrough. Light amplification and lasing with the Raman effect [3] has been achieved, and also infrared light detection is possible, e.g. with hybrid integration of photodiodes or direct epitaxy of Ge or SiGe alloys.
Mainly two fields of technology are expected to benefit from the progress. In op-

tical communication technology, cheaper and more efficient devices might reduce costs, or open up new applications. On circuit boards in chip-to-chip or on-chip communication, optical lines may help to solve the communication bottleneck in high-performance integrated circuits [4].
Furthermore, niche applications in sensor technology and metrology, such as gas sensing [5, 6] are possible.
The main potential of amorphous silicon in integrated optics is in on-chip integrated optical communications. Temperatures of typically 200 to 400 °C for plasma-enhanced chemical vapor deposition (PECVD) allow the deposition on a wide range of substrates and facilitate integration of silicon optical waveguides also within the back-end of integrated circuits in future. Vertical optical coupling between waveguides, as well as fiber coupling within small wafer areas are thinkable.
Silicon and silicon alloys are studied for the application in Raman lasers [7]. If material properties such as carrier lifetime and Raman gain spectrum can be engineered this way, the integrated Raman laser might gain in performance, as is can be seen in already established Raman fiber lasers [8].

Overview

The objectives of this thesis are to study optical properties of amorphous silicon and to test the feasibility of novel concepts of its application in integrated optics.
The physics of amorphous semiconductors together with a summary of characteristics of amorphous silicon is presented in chapter 2. A brief review of the state of the art in silicon photonics in general and also the application of amorphous silicon in this field can be found in chapter 3.
The following chapters deal with design, fabrication and characterization of a-Si thin films, waveguides as well as new concepts of a-Si application. Chapter 4 introduces the fabrication processes used in this work. Chapter 5 explains the metrology used here for thin film characterization with special respect to their application on a-Si thin films.
Results of these measurements are presented in the following chapters 6 and 7. In chapter 6, the properties of a-Si films depending on different deposition parameters and methods are presented, and in chapter 7, the effect of different thermal post-treatments are studied.
Finally, chapter 8 presents the design and characterization of integrated optical waveguides. New concepts of integrated optical devices, such as three dimensional tapers, stacked or slotted waveguides and directional couplers are realized.

Chapter 2

Properties of amorphous silicon

For a general understanding of how the disorder in amorphous silicon influences its properties and differentiates it from c-Si, the physics of amorphous semiconductors is briefly reviewed in this chapter.
Insights from many decades of research and industrial application of amorphous silicon are presented. The materials' properties, which depend on different methods of preparation, doping or postprocessing, are summarized. The impact of the structural disorder on electronic and optical properties is explained.

2.1 Physics of amorphous semiconductors

The periodicity plays a central role for the description of crystalline semiconductors. Therefore, it is initially astonishing, that disordered material can also exhibit semiconducting properties. As we will see, this is a result of the short-range order, which is more important for the general behavior of a solid than the long-range periodic potential.
According to the Bloch theorem, a periodic potential results in a solution for the electron's wave function, which itself consists of a plane wave times a function with the periodicity of the lattice. With the Pauli principle this results in the characteristic dispersion relation for energy and momentum $E(\mathrm{k})$. From this relation, one can determine many important properties.
The effective mass of electrons and holes is determined by the curvature of the conduction- and valence-bands, respectively. The band gap energy represents the distance between conduction band minimum and the maximum of the valence band, and the existence of a displacement in k of these extrema determines the type of the

semiconductor (direct or indirect). In a direct semiconductor no additional momentum is necessary for recombination of electrons at the conduction band minimum, which facilitates efficient radiative recombination.
The atomic structure in the amorphous material is mainly defined by type and strength of its atomic bonds, which in case of covalent bonds as in Si, gives a coordination that results in a near range order. Silicon, after sp^3-hybridization of its s- and p-orbitals, has four valence electrons which can form four bonds with its next neighbors. In contrast to the crystalline state, where each atom's bonds form an ideal tetrahedron, in the disordered solid the bonds usually deviate in length and angle. Some bonds may not be saturated, so called "dangling bonds", which ultimately cause defect states in the band gap.
In case of crystalline materials, defects are e.g. vacancies or interstitial atoms in the lattice. In the amorphous state, as atom locations are not clearly defined, these definitions are meaningless. The defects present here are "coordination defects", i.e. defects exist if covalent bonds (see equation 2.1) are not saturated. The optimum number Z of covalent bonds for a main group element with a number of N valence electrons is given by

$$\mathrm{Z} = 8 - \mathrm{N} \ (\text{for } \mathrm{N} \geq 4) \qquad \text{or} \qquad \mathrm{Z} = \mathrm{N} \ (\text{for } \mathrm{N} < 4). \tag{2.1}$$

2.1.1 Effects of a disturbed periodic potential

In a crystalline material the electronic wave function is in phase with the periodic potential. However, in the amorphous state it immediately runs out of phase along any direction. This causes strong scattering of electrons. Depending on the level of perturbation, the scattering length is reduced to its lower limit, which is given by the atomic spacing. In that case, the electronic wavefunction is localized.
This spacial confinement of the electron implies, because of Heisenbergs uncertainty principle, that the momentum is not known. Therefore, energy bands in amorphous semiconductors cannot be described by the dispersion relation $E(\mathrm{k})$, but only by the density of states $N(\mathrm{E})$. As a consequence, the conservation of momentum selection rules for recombination and generation of charge carriers do not apply in amorphous semiconductors, and the distinction between direct and indirect band gap is lost. Instead, transitions can only occur between states which overlap in real space. The density of states of an amorphous semiconductor is presented in Fig. 2.1.
Compared to the sharp band edges in the crystalline case, extended band tails exists. The disorder potential in amorphous semiconductors is usually such that localized states exist at the band edges, while spatial extended states exist beyond.

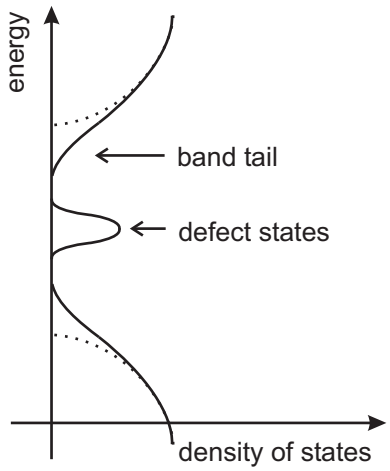

Figure 2.1: Density of states of an amorphous semiconductor (solid line) compared to a crystalline semiconductor (dashed line).

The mobility edge is defined at an energy E_C, which separates the localized states from the extended states (see Fig. 2.2). Localized states do not contribute to the material's conductivity at zero temperature, whereas extended states do.

2.2 Deposition of a-Si:H

It is possible to deposit amorphous silicon using a variety of different process technologies. Among these are physical ones, such as reactive sputtering with argon and hydrogen, as well as chemical processes, such as plasma-enhanced chemical vapor deposition (PECVD) or low-pressure chemical vapor deposition (LPCVD).
Clearly nowadays PECVD with silane (SiH_4) precursor gas prevails as the standard deposition process, because it gives the best results in terms of electrical material properties [9–11]. Low defect densities and high deposition rates can be achieved with this technology. The PECVD system used in this work is described in chapter 4.2.
Silane thermally decomposes above approximately 450°C. Hence, it is possible to thermally activate the deposition process as it is done in case of the LPCVD. At such elevated temperatures (above 400°C), hydrogen is driven completely out of the films, resulting in unsaturated bonds and ultimately in a high defect density. Deposition temperatures above 600°C are used to deposit poly-crystalline or epitaxial layers. In order to study layers with a range of degrees of disorder, LPCVD is also used in this work (see chapter 4.1.1).

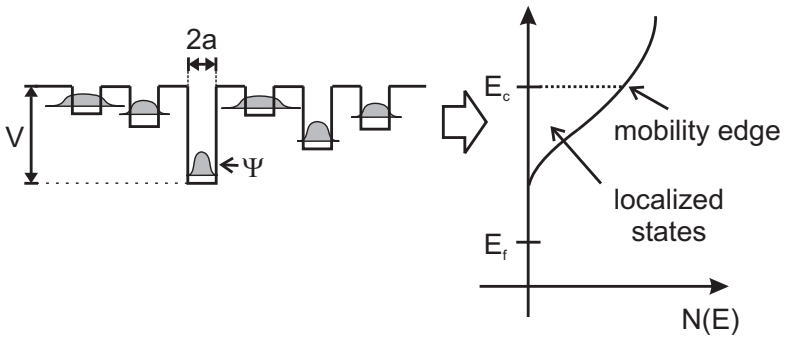

Figure 2.2: Band tail states derived from a disorder model: A distribution of quantum wells defines a distribution of electron wave functions Ψ, which result in localized or spatial extended states.

In the case of PECVD, the activation energy for silane decomposition originates from inelastic collisions with electrons in a plasma (see chapter 4.1.2). Thus, process temperatures are lower (typically 200-400°C), and hydrogen remains in the material, which saturates bonds and reduces defect density.

2.2.1 Growth mechanisms

Chemical reactions, which occur in the plasma and at the film surface, are very complex. A multitude of parameters influence the reaction kinetics. Still, some general implications can be derived in order to describe how the final material properties are influenced by the growth process. The identified silane dissociation reactions and corresponding activation energies are [9]:

$$SiH_4 \rightarrow SiH_2 + H_2 \qquad (2.2\,\text{eV}) \qquad (2.2)$$

$$SiH_4 \rightarrow SiH_3 + H \qquad (4.0\,\text{eV}) \qquad (2.3)$$

$$SiH_4 \rightarrow Si + 2H_2 \qquad (4.2\,\text{eV}) \qquad (2.4)$$

The resulting radicals SiH_2 and Si spontaneously react with SiH_4. To sustain a stable plasma, usually a pressure of $0.1 - 1\,\text{Torr} (= 13.3 - 133.3\,\text{Pa})$ is used in PECVD systems, which corresponds to a free path length of the gas molecules of $0.1 - 0.01\,\text{mm}$. Therefore, secondary reactions in the gas phase are likely, which consume SiH_2 and Si but not SiH_3.
The hydrogen content of typical a-Si:H layers is in the range of 10%. Clearly there is a discrepancy in the amount of hydrogen present in the radicals, and as this is too high, some of the hydrogen must be removed during the film growth. While

the radicals bond to dangling Si-bonds at the film surface, hydrogen is continuously removed from the surface. Weak Si bonds, even within the layer, are saturated by hydrogen and by choosing an elevated temperate of 200-400°C, which promotes hydrogen diffusion, layers with low defect densities can be produced.
During film growth, any new Si-radicals bound to the surface shadow the amorphous network underneath. Hence, it is a little more likely for the next incoming radicals to be bound to this radical, rather than next to it. As a result, the films tend to grow in chains.
Furthermore, in case the surface mobility is decreased, a columnar structure of the films can result. The surface mobility is influenced by parameters such as the plasma power. Also, argon dilution of the precursor gas decreases the surface mobility by increasing the density of higher order radicals, because secondary energy transfer processes from argon to silane promote the creation of these radicals.
A high Ar content and a high plasma power tend to produce columnar structures, whereas more silane and low power give non-columnar layers with lower defect densities. However, the transition between the two regimes is gradual.
The hydrogen in the growth process facilitates the reorganization of weak Si bonds and, by eliminating these bonds, tends to increase the order in the Si network. In case additional hydrogen is used to dilute the silane precursor gas, the deposition rate is reduced and reorganization of the bonds during film growth can be promoted to such an extend, that micro crystalline layers result. Unlike in the case of the columnar and non-columnar regimes, the transition between amorphous and micro crystalline is abrupt [9].

2.3 Structural order of the silicon network

The Si bond energy of 2.5 eV is much higher than the disorder energy of ≈ 0.1 eV present in typical a-Si:H layers. As a consequence, the deviation in bond length is rather small, and the bond angle disorder is in the range of 10°. Due to the strong covalent bonds, the amorphous network is rigid and over-coordinated and builds up internal compressive stress during the growth process. For high quality material with low defect densities, the stresses are actually the highest, typically in the range of 200 MPa [9] ($\leq$ 400 MPa [10]). In material with a columnar structure and higher defect density, the stress is usually lower, because of possible relaxation effects along voids and columnar boundaries.
However, the contribution of different thermal expansion coefficients of the deposited a-Si:H and substrate material is usually negligible compared to the structural effect

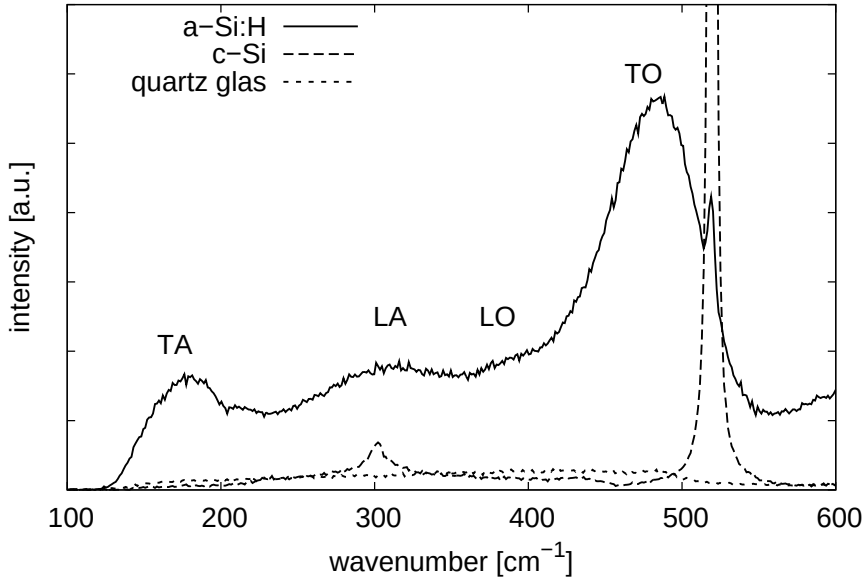

Figure 2.3: Comparison of Raman spectra from amorphous and crystalline silicon.

of over coordination.

2.4 Lattice vibrations and phonon spectra

Because the vibrational modes in a solid are next to atomic masses determined by their bond length and bond angle force constants, the phonon density of states in amorphous Si can be expected to be broadened compared to c-Si due to the bond disorder.

A common method of measuring the phonon characteristics in a solid is Raman spectroscopy (see chapter 5.4). As the technique is based on photon - phonon interaction, the resulting Raman spectrum is not only influenced by the phonon density of states, but also by the rule of momentum conservation.

Due to the negligible photon momentum, this rule exclusively allows transitions at the k=0 point of the phonon dispersion relation into the upper point of the transversal optical (TO) band. The Raman spectrum of c-Si therefore shows a single peak at $520\,\mathrm{cm}^{-1}$ (see Fig. 2.3), which represents this transition.

As described in chapter 2.1.1, the momentum selection rules are relaxed in amorphous materials, which allows all phonons to contribute to a Raman spectrum. The phonon density of states is thus directly reflected in the Raman spectrum. The

different phonon modes can be identified, which are termed transversal and longitudinal acoustic (TA, LA) or optic (TO, LO).
Hence, instead of the single peak at the upper point of the TO band, a broader peak at the lower wavenumber around $480\,\mathrm{cm}^{-1}$ is measured for amorphous Si. The broadening of the TO band can also be used to measure the degree of disorder in the material [12].

2.5 The role of hydrogen

Due to its small radius, hydrogen can diffuse within, out of, or into the material. It has a coordination of one and forms strong covalent bonds with silicon. As mentioned in 2.2, hydrogen removes weak Si-Si bonds from the growing film and gives a more ordered network. Because such a process is especially effective with sufficient H-diffusion, the lowest defect densities are obtained at elevated deposition temperatures.
However, hydrogen is also responsible for the instability of a-Si:H at higher temperatures and is completely removed from the a-Si:H network above 400°C.
In comparison, the effects of H in c-Si and a-Si are similar due to the same covalent bond properties. Defect passivation and dopant passivation occur both in the crystalline as well as the amorphous state.
The intrinsically much higher defect density and the network reconstruction initiated are the reasons for the significance of hydrogen in amorphous silicon.

2.6 Electronic density of states in a-Si

The general appearance of the density of states distribution in amorphous semiconductors can be derived from a model, in which the periodic potential with random distribution of energy is inserted into the Schroedinger equation (see chapter 2.1).
The broadening of the density of states distribution, the existence of band tails, the localization of the band tail states, the reduction of scattering length to atomic distances and the loss of momentum conservation are the effects of disorder. More specifically, for amorphous silicon the density of states can also be extracted from the chemical bond theory (see Fig.2.4).

Measurements of the photoemission spectrum reveal the actual density of states, and coarse measurements with x-ray photoemission show, that the bands are very much alike the crystalline ones [9, 10]. This is because the bands are approximately

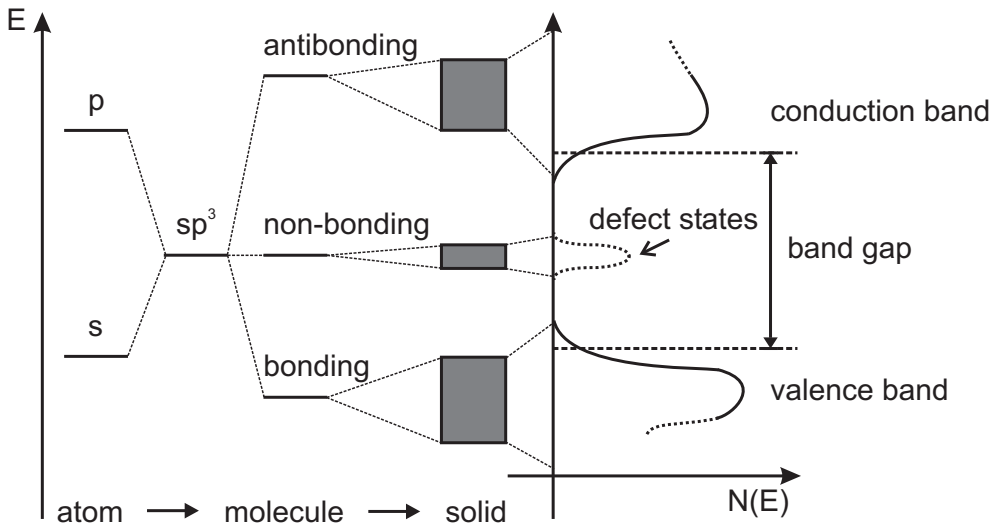

Figure 2.4: The density of electronic states in amorphous Si originates in the chemical bonds.

10 eV wide and the disorder energy is two orders of magnitude lower (≈ 0.1 eV). Nevertheless, the states close to the band edges are most important for the optical and electrical properties. Measurements by photoemission spectroscopy with a finer energy resolution show an exponential band tails in addition to the linear band edges. Furthermore, electrical measurements can determine the rate of excitation of trapped carriers during electronic transport, which give a measure of the energy distribution of localized band tail states. The band tail is characterized by the slope E_0 of the absorption caused by the band tail states, called the "Urbach edge" (see chapter 2.8).
For amorphous silicon, the valence band tail width is ≥ 42 meV, whereas the conduction band tail is less susceptible to disorder (≤ 35 meV) [11]. These energies increase with bonding disorder and defect density in the material, therefore smaller values reflect better film qualities. Due to the band tails, the optical band gap energy is usually defined in terms of extrapolation of the density of states and has a typical value for a-Si:H of $1.7 - 1.8$ eV. The mobility gap, which is defined as the energy difference between the mobility edges (see chapter 2.1), is generally larger.

2.7 Defects

The high density of defects in pure a-Si without hydrogen is the reason for its lesser importance for any technical applications. In a-Si:H the defect density is reduced, but still a number of defects are present.
The density of these defects and all materials' properties are determined by the growth process and possible postprocessing. Hence, a well developed and controlled process is an essential basis for the application of amorphous silicon in electronic or optical applications.
Defects can be characterized by their energy levels and different charge states, which are determined by the atomic bonding structure of the defect. Due to the broadening of the defects' energetic states a smaller number of distinct defects can be identified in a-Si.
Besides coordination defects, which can have a net charge when an electron is added at a dangling bond, impurity defects can also be present. Unlike in c-Si, their states are broader and, because the coordination in the amorphous matrix is only in average 4-fold, but must not necessarily be so for a single atom, the state of an impurity defect might even merge into a band. This complicates the activation of "desired impurities", i.e. dopants.
A special defect type only found in a-Si:H is the hydrogenated microscopic void, which does not necessarily have an impact on the electronic states, if the atoms around the void have a similar distribution of bonding disorder than in the bulk amorphous network. For optical applications, any voids in the material are undesirable, because they represent a local change in refractive index and thus increase scattering loss.

2.7.1 Doping

The most common way to insert dopants into a-Si:H is to add phosphine or diborane to the precursor gases during deposition.
Theoretically, the rules for chemical bonding state, that all atoms in a random amorphous network bond according to their number of valence electrons (see 8-N rule chapter 2.1). Thus, substitutional doping should in principle not be possible.
However, it was first realized and reported by Spear and LeComber in 1975 [13], although the doping efficiency is very low compared to crystalline Si. For example, in the case of n-doping with phosphine, roughly 1% of the dopant is in the fourfold state [9]. Most of the remaining dopants ($\approx 90\%$) are compensated by defects,

because the dangling bond density is also increased by doping. About 90% of the remaining electrons are trapped in localized band tail states. The electronic density of states in doped a-Si:H in comparison to c-Si has dopant states forming a band broadened by disorder and overlapping partially with the intrinsic band tail states. Altogether in terms of free electron density, the doping efficiency is about 10^{-4}.
Due to the also lower carrier mobility, the maximum conductivity for doped a-Si:H is more than five orders of magnitude lower than in c-Si.

2.8 Optical transitions

The mechanism of carrier generation by optical absorption can be used to determine the band gap energy and band tail slope from spectroscopic measurements. The imaginary part of the complex dielectric permittivity $\varepsilon = \varepsilon_1(\omega) + j\varepsilon_2(\omega)$ is proportional to the absorption coefficient:

$$\alpha(\omega) = \frac{2\pi\varepsilon_2(\omega)}{n \cdot \lambda} \tag{2.5}$$

As the momentum conservation in the amorphous material is not relevant, the connection of the electronic density of states with the complex dielectric permittivity can be obtained by an integration of the valence- and conduction band density of states, which allow a transition of a certain energy $\hbar\omega$,

$$\varepsilon_2(\omega) = 4\pi^2 e^2 a^3 R^2(\hbar\omega) \cdot \int N_V(E) N_C(E + \hbar\omega) dE \tag{2.6}$$

where R is the reduced average of the dipole matrix elements.
Therefore, the band tails are directly reflected in the dielectric function. Compared to crystals, no singularities in $\varepsilon_2(\omega)$ resulting from the sharp band edges exist. Also, no excitonic states can exist.
Close to the band edge, some transitions involve localized states. In that case, the spacial overlap of the involved states has to be taken into account, as the transition probability exponentially decreases with distance.
Experimental investigation of the absorption spectrum of a-Si:H by photo current measurements reveals an absorption edge that can be separated into three regions [14]. High energy transitions between extended valence-band and the conduction-band states result in a high absorption ($\alpha \approx 10^3 - 10^4\,\mathrm{cm}^{-1}$) with a parabolic spectral response,

$$\alpha(\hbar\omega) \propto -(\hbar\omega - E_0)^2 \tag{2.7}$$

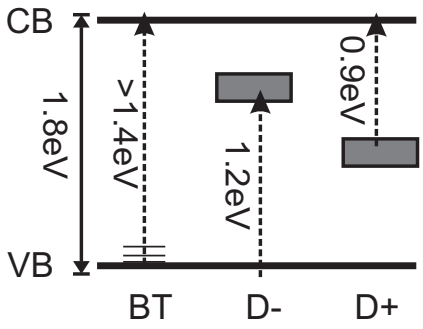

Figure 2.5: Optical Transitions with relevance for the infrared spectrum. The band tail absorption (BT) and neutral dangling bonds' acceptance (D-) or release (D+) of an electron.

where E_0 is usually termed the optical energy gap. For lower energies close to the band gap, the decrease in absorption is better described by an exponential function.

$$\alpha(\hbar\omega) = \alpha_0 \exp\left[(E - \hbar\omega)/E_U\right] \tag{2.8}$$

The exponential tail is called "Urbach edge" and E_U the "Urbach energy". It is usually in the order of $50 - 100\,\mathrm{meV}$ for a-Si:H. Transitions between localized band-tail states and extended states occur in this regime.
The remaining absorption involves structural defects at even lower energies closer to the center of the band gap.
Absorption of near-infrared light corresponding to energy levels in within the band gap is of interest for an application in integrated optics. Thus, structural defects have to be taken into account.

2.8.1 Absorption due to defects

A linear relation of dangling bond density (measured by ESR spin density) to the optical absorption around 1.2 eV is observed in a-Si:H [15, 16]. The factor of proportionality, which represents the mean optical cross section, is around $10^{-16}\,\mathrm{cm}^2$.
The two possible transitions of neutral dangling bonds from a neutral state (filled with a single electron) to a positively charged state (by passing the electron into the conduction band) or negatively charged state (by accepting an electron from the valence band and creating a hole) correspond to the optical absorption.
Different transitions have been identified in modulated photo current measurements and the thresholds of transition are approximately 0.9 eV for the conduction band transition and 1.2 eV for the valence band transition [14]. This means for an optical gap of approximately 1.8 eV, the energy levels in the forbidden gap created by dangling bonds are located at 0.9 eV and 0.6 eV with respect to the conduction band edge.

The difference between the two values is termed the effective electronic correlation energy, and is caused by Coulomb potential, lattice relaxation energy, electron-photon interaction and re-hybridization energy.
The positions of the dangling bond states and the transitions with energies lower than the optical gap energy are outlined in Fig. 2.5.

2.9 Electrical Properties

2.9.1 Conductivity

Conductivity is a quantity in which several carrier properties are integrated and averaged. The energy dependent carrier density $N(E)$ and mobility $\mu(E)$ are included in the calculation of the conductivity σ,

$$\sigma = \int N(E)e \cdot \mu(E) \cdot f(E,T)\, dE \tag{2.9}$$

where $f(E,T)$ is the Fermi function and e the elementary charge.
Therefore, the dominant conduction path is determined by density of states, carrier mobility and Fermi function. These quantities are again determined by defect and dopant densities in the material and temperature as a surrounding condition. Dependent on these parameters, three conductions mechanisms occur in amorphous semiconductors:

Hopping conduction at the Fermi level

In materials with high defect densities, this is the dominant conduction mechanism. The Fermi level is pinned by the defect states to the band gap center, which suppresses any conduction due to carriers in the band tails. The defect density is large enough for significant tunneling to occur between localized defect states.
In high quality a-Si:H, hydrogen reduces the defect density and avoids this effect.

Band tail conduction

At elevated temperatures conduction by hopping of localized states from site to site is possible.

Table 2.1: Conductivity prefactor σ_0 and activation energy E_σ for a-Si:H [9].

material	σ_0 $[\Omega^{-1}cm^{-1}]$	E_σ $[eV]$
undoped, low defect density	10^4	0.9
undoped, high defect density	2300	0.85
n-type	1-10	0.1-0.2

Extended state conduction

Carriers can be thermally activated from the Fermi level above the mobility edge. Due to the difference between Fermi energy and mobility edge, which is $\approx 1\,\mathrm{eV}$ in the case of undoped a-Si:H and not less than $\approx 0.1\,\mathrm{eV}$ in n-type a-Si:H, this is usually overlapped by band tail conduction.
All conduction mechanisms also show that local chemical bonds in the amorphous silicon play an important role rather than the long range periodic potential.

Due to the nature of the conduction mechanisms, the conductivity σ of a-Si is thermally activated:

$$\sigma(T) = \sigma_0 \exp(-E_\sigma/kT) = \sigma_0 \exp[-(E_{CE} - E_F)/kT] \tag{2.10}$$

At room temperature, i.e. below the temperature where structural changes start to occur, the conductivity prefactor σ_0 and activation energy E_σ depend on defect and dopant density (see Tab. 2.1). The simple model of a sharp mobility edge with the conductivity prefactor is adequate at room temperature and above. However, other effects like the difference between thermopower and conductivity energies, as well as the behavior at low temperatures cannot be explained.

2.9.2 Carrier mobility

The mobility of free charge carriers is greatly reduced in the amorphous state due to localization and scattering. The mobility μ is related to the mean free time τ_m or mean free path λ_m,

$$\mu = \frac{q \cdot \tau_m}{m^*} = \frac{q \cdot \lambda_m}{m^* \cdot \upsilon_{th}} \tag{2.11}$$

where m^* is the effective mass and $\upsilon_{th} = \sqrt{3kT/m^*}$ is the thermal velocity.
In crystalline silicon the mobility is $\mu_c \approx 1000\,\mathrm{cm}^2/\mathrm{Vs}$, which corresponds to a scattering length of $\lambda_m \approx 100\,\mathrm{nm}$. In amorphous silicon the mobility is three orders of

magnitude lower, which corresponds to a scattering length in the order of the atomic spacing [9].
Usually, the mobility is determined by electrical sweep-out measurements. As the measurement time exceeds the average trapping time for carriers, the reduced drift mobility is measured.
Values for the drift- and corresponding free carrier mobilities (calculated by a multiple trapping model) in a-Si:H are presented in Tab. 2.2. Doped a-Si:H generally has lower mobilities than undoped a-Si:H.

2.9.3 Recombination kinetics

Charge carriers recombine mainly via two successive steps schematically shown in figure 2.6. First, the electron or hole loses energy by many small and frequent transitions within the band, as the density of free states is high. This process is termed "thermalization". It is on a timescale of 10^{-12} s as long as the carrier is within the extended states (1a: fast thermalization), but slows down to 1-10 ps when the carrier reaches the mobility edge and occupies the localized states (1b: slow thermalization). Then, the charge carrier eventually recombines.
Three main recombinations path exist. Direct tunneling to a tail state (A) close by is the dominant mechanism for low defect densities and low temperatures.
Recombination via a defect (B) state is dominant for temperatures above 100 K or defect densities above $10^{17}\,\mathrm{cm}^{-3}$. Reason for this effect is a much higher recombination rate for the phonon-assisted recombination via defects compared to the rate of radiative direct recombination. At temperatures where the mobility is high enough, the carriers predominantly recombine via defect states, although their density is lower than the density of the band tail states. The time scale for radiative tunneling is in the broad range of $10^{-8} - 10^{-2}$ s with a peak at $10^{-3} - 10^{-4}$ s. The carrier lifetime at room temperature in material with a low defect density is mainly influenced by the recombination via defects and is in the order of 10^{-6} s [10]. Because of the rapidity of the thermalization compared to the subsequent recombination mechanisms, virtually all carriers recombine from the localized states.
Furthermore, thermal re-excitation of the carrier can occur (C) at high temperatures.

2.10 Interfaces

The material properties in thin films and moreover in three dimensional microstructures such as waveguides, or even nanowires, are significantly influenced by the

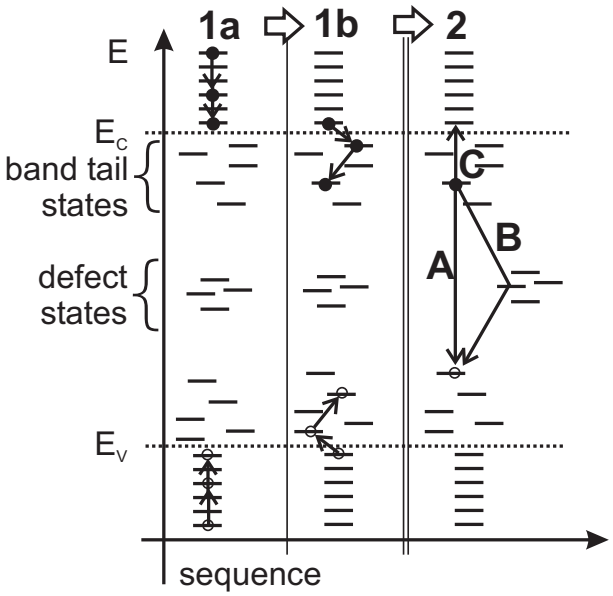

Figure 2.6: Sequence of recombination processes: Initially fast (1a) and slow (1b) thermalization occurs. Then the electron-hole pair recombines directly (A), or via a defect state (B), or is thermally excited (C).

surfaces and interfaces. Surface states can act as recombination centers or traps, and surface charges can cause band bending. In the case of interfaces, the work function of the materials additionally influence the band bending.

2.10.1 Surface recombination

The recombination kinetics is altered at a surface or interface, because a high density of recombination centers is usually present. The surface recombination rate is then governed by the diffusion of carriers to the surface. The concentration gradient extends only about the diffusion length into the material.
As in amorphous Si the diffusion length is relatively small, this effect is far less pronounced compared to crystalline Si.

2.10.2 Metallic contacts

When a metal is brought in contact with a semiconductor, generally the formation of a Schottky barrier occurs due to the charge transfer across the interface in order to align the Fermi energies. This is also the case for a-Si:H and the properties of the

resulting Schottky contacts are much alike the case of crystalline Si.
The dependence of barrier height on work function is usually weaker than one would expect from the ideal Schottky barrier model because of additional interface charges. In the case of undoped, low defect-density a-Si:H, the depletion width without external bias is about $1\,\mu$m [9].
Ohmic contacts can be fabricated with high doping levels. The Schottky barrier is removed by an in-situ doping level at a flow ratio of 10^{-2} PH_3 to SiH_4 precursor gases [17]. Chemical reactions can also be used to influence the barrier. Palladium or platinum form stable silicides above 200 °C, whereas gold or aluminum promote non-uniform crystallization of a-Si:H films.

2.10.3 Multilayers

The deposition techniques used to fabricate high-quality a-Si:H films at low temperatures give the opportunity to create multi-layer structures with negligible atomic inter-diffusion (despite hydrogen). Smooth and abrupt interfaces can be obtained simply by changing the gas composition during the deposition process. In multilayers fabricated this way, recombination at surface states can reduce carrier lifetime.
On the other hand, when a sequence of doped and undoped layers is deposited, which spatially separates the carriers after generation ("nipi - structure", [18]), the lifetimes can be significantly enhanced.

2.11 Thermal stability

Hydrogen can diffuse in the rigid Si matrix at elevated temperatures of 100 °C to 300 °C [19] and is responsible for reversible metastable phenomena (see chapter 2.11.1). At even higher temperatures (400 °C and above), hydrogen is desorbed out of the material and consequently the density of defects increases. When the temperature exceeds 600 °C, the material starts to crystallize and the hydrogen is almost completely removed.
For thin films or even complex micro-structures such as optical waveguides, further aspects have impact on the crystallization. Not only the bulk crystallization energy, but also the surface and interface free energies have to be taken into account. Boundary conditions such as the substrate materials, film-substrate adherence, deposition parameters or film thickness all influence the crystallization process.

2.11.1 Effects of metastability

In a-Si:H annealed at temperatures below the onset of crystallization, a long range order cannot be achieved. However, in the short and medium range atomic order, reversible effects of equilibration exist.
The defect density increases with quench temperature and rate in (undoped) a-Si:H, but can be again reduced by a thermal annealing [9]. This effect can be described by an reaction of two weak bonds to form one defect.
However, in the medium range order of high quality a-Si:H with low defect densities, no such effect is detected. The band tail slope measured on the basis of carrier drift mobility does not change due to annealing or quenching. Only for materials with high defect densities and extended band tail deposited at temperatures lower than optimum, a reduction of defect density and band tail slope can be achieved by thermal annealing.
The observed reduction of defects obeys a stretched exponential relaxation, which is typical for glasses. This behavior can be attributed to a glass-like network of bonded hydrogen within the rigid Si network in a-Si:H. Material with high defect densities releases specific heat at anneal temperatures of 120-180 °C. The small amount of heat released ($\approx 1.5\,\mathrm{mcal/g \cdot K}$) indicates, that only hydrogen participates in the structural change [20].
Furthermore, defects can be created by external excitation. For instance, illumination, current flow or energetic particles cause reversible defects, which are stable in undoped a-Si:H at room temperature, but can be removed at 150-200 °C. Due to light induced defects, a decrease of photoconductivity during illumination and lower dark conductivity after illumination is observed ("Staebler and Wronski effect", [21]). Sunlight illumination of several hours creates a defect density of $\approx 10^{17}\,\mathrm{cm^{-3}}$. The low creation and annealing rates indicate a structural change as the root cause, rather than only a change of charged states. In applications such as solar cells or thin film transistors (TFT), these effects can cause significant degradation.

2.12 Chapter summary

The properties of amorphous silicon as they have been outlined in this chapter are promising for optical application. The band gap of 1.7-1.8 eV and the low defect density, at least for high quality plasma-deposited hydrogenated silicon, are prerequisites for a material with low optical losses for highly integrated optical devices. However, the possible thermal and optical degradation has to be taken into account for future applications.
Table 2.2 summarizes some of the characteristics of a-Si:H.
The possibility exists to engineer materials' properties by changing the degree of disorder or the hydrogen content, either by deposition methods and parameters or also by different post-treatments. It is to be considered, when the feasibility of an application in integrated optics is studied.

Table 2.2: Typical properties of undoped a-Si:H at room temperature [9–11].

Property	Typical values
optical band gap	$1.7 - 1.8\,\mathrm{eV}$
valence band tail slope	$42 - 50\,\mathrm{meV}$
conduction band tail slope	$\approx 25\,\mathrm{meV}$
density of states at Fermi level	$5 \cdot 10^{14}\,\mathrm{eV^{-1}cm^{-3}}$
hydrogen content	$8 - 15\,\%$
intrinsic stresses	$\leq 400\,\mathrm{MPa}$
electron drift mobility	$\geq 1\,\mathrm{cm^2V^{-1}s^{-1}}$
hole drift mobility	$\geq 8 \cdot 10^{-3}\,\mathrm{cm^2V^{-1}s^{-1}}$
electron lifetime	$\geq 0.2\,\mu\mathrm{s}$
hole lifetime	$\geq 1.0\,\mu\mathrm{s}$
dark conductivity	$10^{-11} - 10^{-10}\,\mathrm{Scm^{-1}}$
conductivity activation energy	$0.7 - 0.9\,\mathrm{eV}$

Chapter 3

Silicon Photonics

The state of the art in silicon photonics is reviewed in this chapter. Starting with an introduction on optical waveguides, passive elements such as couplers or resonators are briefly described. Progress in light modulation, detection and generation in Si is summarized.
Finally, approaches to on-chip electronic-photonic integration and the application and state of the art of amorphous silicon in integrated optical devices is presented.

3.1 Introduction

The potential of Si with respect to optical applications was already envisioned in the 1980th [22]. The transparency and high refractive index of Si in the infrared spectral range which is used for communication, makes it possible to design waveguides and any passive optical devices based on waveguides as the building blocks, e.g. filters, splitters or combiners. The accomplishments in silicon microelectronics fabrication technology also provide the means for practical implementation.
In the last decades, the progress in this field of technology has been immense. The ability to produce smaller and smaller feature sizes in highly integrated circuits together with the vast potential of optical communication networks, provided the computation and communication capacities, which are the basis of the internet.
However, it was about the turn of the millennium when research in the field saw an remarkable upturn. One of the reasons for this were the improvements in lithography, which made it possible to produce sub-micron feature size necessary for photonic devices in a cost-effective way [23]. Further reasons are the progress in infrared light modulation, generation and detection in silicon:
With the demonstration of electro-optical GHz-modulation by charge accumulation

and depletion in MOS capacitors by Liu et al. [2], the integration of optical modulators with electronics on a single silicon substrate became possible.
The demonstration of a silicon laser using the effect of Raman amplification in c-Si [3] in a way defies the limitation of the indirect band-gap. Though with this approach electrical pumping like in III/V-semiconductors is still impossible, the optically pumped Raman laser open up a range of possible future applications in sensing or communications [24].
Hybrid integration of III-V-based lasers or photodetectors is another way to overcome the limitations of Si. Lately, also with direct hetero - epitaxy of Ge or SiGe alloys, even integrated with amorphous Si waveguides [25], a remarkable detector performance has been achieved.
Altogether the above mentioned milestones give a technological base, while the possible benefits and new applications drive the current strive for fully integrated electronic - photonic integrated circuits ("EPIC") [26].
Already a number of introductions and reviews about the topic exist [27–36], which are altogether more complete than the brief summary presented here.

3.2 Waveguides

Integrated optical devices are often characterized as "active" or "passive", where "active" denotes devices, in which light generation, detection or modulation, i.e. any form of electro-optical or also all-optical conversion, occurs. "Passive" circuits on the other hand simply utilize the characteristic of light as an electromagnetic wave. For instance, waveguides, resonators or gratings are used to build e.g. filters, couplers or multiplexers. Most commonly, these passive devices are build from amorphous thin films such as silicon-oxinitride (SiON), because it is a transparent insulator with a refractive index that can be set during deposition by changing the O to N ratio between n = 1.46 for SiO_2 and n = 2.0 for pure Si_3N_4 [37].
In this section, the theoretical fundamentals of waveguides and resonators are briefly presented, then special aspects with respect to Si as a waveguide material are discussed.
Finally, the state of the art of passive devices fabricated in SOI technology is shown and the problem of efficient light coupling into small silicon waveguides is addressed.

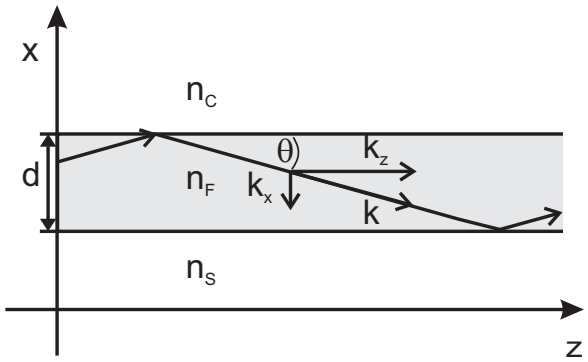

Figure 3.1: Light propagation due to total internal reflection in a planar waveguide.

3.2.1 Waveguide theory

Waveguiding in dielectrics is based on total internal reflection at interfaces of materials with a higher refractive index to one with a lower index.
A multitude of books exists, which present waveguide theory in detail (see e.g. [28, 38, 39]). Thus, only a brief summary is presented in order to gain insight into the consequences of using silicon as a waveguide material.
Figure 3.1 depicts a film of an optically dense material with refractive index n_f and thickness d sandwiched between cladding (n_c) and substrate (n_s) materials.
Because of $n_f > n_{c,s}$, a beam of light with wavevector $\vec{k}$ can propagate in this film along the z-direction due to total internal reflection.
Two conditions must be fulfilled in order to achieve loss-less propagation.
First, the angle of propagation Θ must be smaller than the critical angle for total internal reflection Θ_c:

$$\Theta < \Theta_c = \arccos \frac{n_{c,s}}{n_f} \tag{3.1}$$

Second, the resonance condition for the cavity existing in the x-direction must be met. With the film thickness d, a revolution of the wave in the cavity leads to the so called characteristic equation,

$$(2dn_f) \cdot (k \sin \Theta) - \Phi_c - \Phi_s = 2\pi \cdot m \tag{3.2}$$

where $\Phi_{c,s}$ are the polarization dependent phase discontinuities upon reflection at the two interfaces.
The second condition is only met for discrete propagation angles corresponding to solutions specified by the natural number $m = 1, 2, ...$, representing the modes of the waveguide.

The phase differences $\Phi_{c,s}$ in the characteristic equation 3.2 are polarization dependent. This implies a polarization dependence of the modes, which are split up into TE (transversal electric) or TM (transversal magnetic). The denotation indicates, that electric or magnetic field components, respectively, exist only perpendicular to the propagation direction. However, this statement is only correct for slab waveguides, and therefore in two dimensional waveguides the modes are commonly referred to as "quasi-TE" or "quasi-TM".
Looking at the propagation direction z, the propagation angle and film refractive index are usually expressed by the effective index n_{eff}:

$$\mathrm{n}_{eff} = \mathrm{n}_f \cdot \cos\Theta \tag{3.3}$$

One can now see, that each mode with its corresponding propagation angle and effective index travels at a different speed in z-direction, resulting in inter-modal dispersion. In order to avoid this bandwidth-limiting effect, waveguides are usually designed to allow the propagation of a single mode only.
For given refractive indices of the applied materials, this means to reduce the waveguide dimensions, so that one of the fundamental modes is allowed to propagate. In the case of a Si waveguide ($n_f = 3.46$) sandwiched between SiO_2 ($n_{c,s} = 1.46$), this results in a film thickness of less than 300 nm. Materials with lower refractive index differences allow the design of larger waveguide dimensions, as it is generally the case for fiber optics.
For any practical applications, waveguides need to guide light in both dimensions perpendicular to the propagation direction. The analytical calculation of the waveguide modes is possible only under simplifying assumptions, for example with the effective index approach [38]. In practice, these two dimensional problems, as well as the simulation of complex devices, are solved numerically. In this work, a full-vectorial finite-difference mode solver [8] is applied to design waveguides and couplers presented in chapter 8.
One can already conclude from the simple consideration of a film waveguide, that the choice of Si as a waveguide material with high index differences thus require sub-micron dimensions, in order to meet the single mode condition. Hence, state-of-the-art lithography and fabrication technologies are necessary for fabrication.
With these prerequisites available, highly integrated optical circuits can be achieved, because high-index differences also allow for high waveguide curvatures.

3.2.2 Propagation losses

Coupling losses

Optical losses in waveguides occur due to different reasons.
If influences of materials and fabrication are omitted, i.e. the waveguide surface is perfect and the materials are ideally transparent, losses can occur due to design.
Light intensity in the waveguide can be decreased by coupling to a high-index material in the vicinity of the waveguide. For example, losses into the substrate occur, if the insulation layer between Si substrate and waveguide is insufficient.

Curvature losses

Additional losses occur, if the waveguide is curved.
Curvature losses are higher, if the mode is less confined, i.e. a larger part of the evanescent field is beyond a critical curvature radius, where the phase velocity of the wave would have to exceed the phase velocity in the material. Therefore, this fraction of the wave is not guided and radiates out. By using a waveguide design with high index differences, the mode is more tightly confined in the waveguide. Hence, smaller curvature radii can be fabricated without intolerable losses.
Generally, losses increase exponentially with decreasing curvature radii [38]. To calculate curvature losses, in practice numerical methods have to be applied [40].

Material absorption

If a material is not ideally transparent, the refractive index possesses an additional imaginary part $\bar{\mathrm{n}} = \mathrm{n} + j\alpha$, and absorption occurs. This reduces the optical power P along the propagation direction exponentially according to Lambert-Beer law:

$$\mathrm{P} = \mathrm{P}_0 \cdot \exp^{-\alpha z} \tag{3.4}$$

This is for instance the case in silicon for the infrared wavelength band around $1.5\,\mu$m, if a density of defects creates energy levels in the band gap. In that case, the absorption edge extends towards longer wavelength (inter-band absorption).
Also present in semiconductors is the free carrier absorption (FCA). A density of free electrons N_e or holes N_h absorbs light. An expression for the approximate change of absorption can be derived from from the Drude model. Based on the results by Soref et al. [41, 42], a formula, which expresses the linear relation to carrier density N and quadratic relation to wavelength λ, can be derived [43],

$$\Delta\alpha(\lambda) = \bar{\varrho} \cdot \lambda^2 \cdot \mathrm{N} \tag{3.5}$$

where $\bar{\varrho} = 6.0 \cdot 10^{-10}$ represents the FCA efficiency.
Carrier concentrations above $10^{18}\,\mathrm{cm}^{-3}$ start to have significant impact on absorption in Si for the relevant wavelength range around $1.5\,\mu$m.
For insulators without any free carriers, such as SiON CVD films, material absorption can result from molecule groups, such as NH or OH, with vibrational modes in resonance with the near infrared.

Scattering losses

Imperfect sidewalls and surfaces with a certain roughness, or also inhomogeneities in the material with local refractive index differences cause scattering losses.
An analytical approach to calculate scattering loss for a given waveguide geometry is presented by Payne and Lacey [44], who formulate an expression for the upper boundaries of absorption α caused by scattering. It is found assuming a Gaussian ($\kappa = 0.76$) or exponential ($\kappa = 0.48$) roughness autocorrelation function. The waveguide is described by normalized parameters and its surface roughness, defined by the correlation length and the mean square deviation σ^2.

$$\alpha = \frac{\sigma^2}{\mathrm{n}_f \mathrm{k}_0 \cdot (\mathrm{d}/2)^4} \cdot \kappa \tag{3.6}$$

The approach is based on slab waveguides with a thickness d, but also represents a valid approximation for two dimensional waveguides, when used with the effective index method as a way of simplification.
Waveguides fabricated from silicon are most sensitive to potential scattering, because of their high refractive index and, also owing to this fact, their small dimensions.
For example, a 300 nm thick slab waveguides with a mean square roughness of $\sigma = 2\,\mathrm{nm}$ results in losses up to $\alpha = -18\,\mathrm{dB/cm}$. This implies a well controlled fabrication of the waveguides in order to minimize any roughness.

3.2.3 Silicon waveguides

The two most common types of waveguides made from silicon are presented in figure 3.2. Rib waveguides (a) were fabricated in the earlier days of Si photonics research from c-Si based on SOI [45], and also in amorphous Si rib waveguides were fabricated first [46, 47].
Rib waveguides have an effectively lowered index difference due to the partly etched sides. If the correct proportions of the width W, height H and etched depth h are chosen, single mode propagation can be achieved for dimensions much larger than

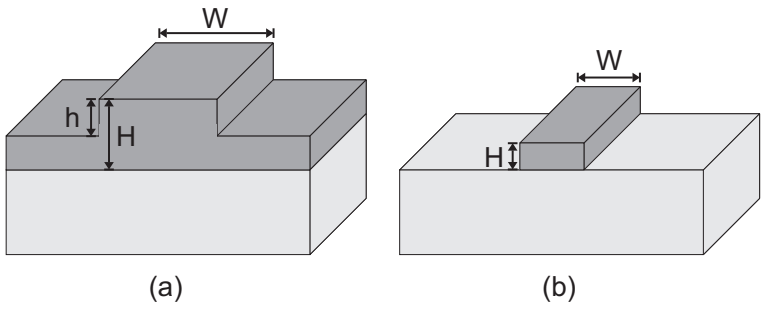

Figure 3.2: Waveguide types commonly used in Si photonics: (a) rib waveguide, (b) strip waveguide.

in the case of strip waveguides.
The condition for single-mode operation has been first proposed by Soref et al. [1]. The ratio of the remaining slab to the rib height r =(H−h)/H must have a minimum value according to:

$$\frac{\mathrm{W}}{\mathrm{H}} \leq 0.3 + \frac{r}{\sqrt{1-r^2}} \qquad (\text{for } 0.5 \leq r < 1) \tag{3.7}$$

Typically, rib waveguides with a width in the range of $1 - 10\,\mu$m are fabricated, whereas the width of strip waveguides is in the order of a few hundred nm with a height of typically around 250 nm.
Therefore, an advantage of the rib design is the reduced requirements on fabrication technology. The structures can be defined by i-line lithography, whereas for submicron features either steppers with excimer laser sources, or e-beam lithography must be applied. The latter can be used for research purposes only, due to their limited capacity. Possible scattering losses, which often occur due to rough sidewalls, are also reduced by the rib design, which also reduces the requirements for the applied etch process.
The polarization dependence of waveguides can be problematic for practical applications [48]. It can be avoided by design for rib waveguides [49], whereas it can only be avoided for strip waveguides by symmetry, i.e. a square cross-section.
On the other hand, disadvantages of the rib waveguides are weak guidance, resulting in much larger bending radii and thus less compact devices.
Also, the demand for thick Si layers, also in the order of μm, is a clear disadvantage, because it can only be met by additional epitaxial growth on SOI wafers or by bonded wafers, which usually have wide specifications for the layer thickness. Hence, they are not well suited for optical applications.

Furthermore, some novel waveguide concepts exist, which have been developed with respect to special applications such as sensing. For example, free standing waveguide fabricated by an underetching technique have been applied for gas sensing [5, 6], or slotted waveguides have been fabricated to enable modulation by electro-optic polymers [50].

3.2.4 Coupling into Si waveguides

The small dimensions of Si waveguides make an efficient coupling of light into these waveguides very difficult. Due to the extreme mismatch between core diameters of an optical fiber ($9\,\mu$m) and waveguides (e.g. strip waveguides $\leq 0.3\,\mu$m), simple butt-coupling as it is commonly used in combination with other waveguide types, is not feasible with small Si waveguides. Therefore, effort has been spent for the development of taper structures with high coupling efficiencies.
A vertical approach with grating couplers is presented by Roelkens et al. [51], and high coupling efficiencies are achieved. Vertical fiber alignment has the advantage of functioning without any sawing and facet preparation, such as polishing and anti-reflection coatings. On the other hand, packaging of such products will be a future challenge.
Horizontal approaches, where the fiber is in-line with the waveguide, and thus careful facet preparation is necessary, have also been implemented successfully. Inverse tapers with larger polymer waveguides on top yield low incoupling losses [52]. Long inverse tapers also give good results without polymer cladding [53].
However, as long as tapers are formed by lithography, they are constrained to one dimension, i.e. only the width, as the height cannot be tapered. In order to produce 3D-tapering, for example gray-scale lithography has been applied [54, 55].
Also deposition of a-Si has been used to fabricate 3D-tapers. Janz et al. [56] deposited a graded-index layer of a-Si by PECVD, which was structured by lithography and dry-etching. Using shadow-masks during deposition of a-Si, 3D-tapers have been fabricated without the subsequent etch step [57, 58]. Transmission losses as low as 0.5 dB have been reported using a 3D-taper fabricated with shadow masks during sputter-deposition of a-Si [59].
A concept of a shadow-mask made from a double-side polished Si-wafer [60], which allows a fabrication of longer tapers made from PECVD hydrogenated a-Si instead of sputtered a-Si, which has advantages due to the better optical quality as explained in chapter 2, is presented in more detail in chapter 8.4.1.

3.3 Passive devices

3.3.1 Directional couplers

A directional coupler consists of two waveguides, which are in close proximity to each other. The evanescent fields of each waveguide's mode extends into the other. If light is propagating in one of the waveguides, it is coupled into the other one and then may in turn couple back into the first waveguide. Along the propagation direction, the optical power is moving from one waveguide to the other, much like the kinetic energy in a mechanical coupled pendulum.
Optical power is coupled completely in the case of a symmetrical coupler between equal waveguides over the power exchange length L_C. At the location $L_C/2$ half of the optical power is coupled into the second waveguide, which means a 3 dB-coupler can be designed, if the waveguides are split up at this point.
The power exchange length is the most significant parameter of a directional coupler and can be calculated analytically under simplifying assumptions (see e.g. [38]).
It can also be found by regarding the two weakly coupled waveguides as one waveguiding structure and calculating its modes. Usually by application of a numerical mode solver, one finds two orthogonal eigenmodes (also called "supermodes"), which are characterized by their different effective indices n_1, n_2.
Hence, the different propagation velocities result in a phase difference along propagation direction. The coupling is complete at a phase difference of π, and the expression 3.8 for the power exchange length is obtained [61].

$$L_C = \frac{\lambda}{2(n_1 - n_2)} \tag{3.8}$$

When fabricated based on SOI, directional couplers need to be designed in one Si layer, and in consequence the waveguides must be placed side by side.
When deposited amorphous Si is used in combination with planarization techniques, also directional couplers consisting of waveguides on top of each other are thinkable (see chapter 8.5.1), adding the vertical dimension into the design, and making higher integration densities of optical ICs possible.
Directional couplers can be fabricated from silicon with larger rib waveguides [62], or also from smaller strip waveguides, which demand much higher accuracy in lithography [63].

3.3.2 Multimode interference couplers

The multimode interference coupler (MMI) is based on a multimodal region, with a number of monomode input and output waveguides at its two ends.
Due to the superposition of all propagating modes in the MMI, multiple images of the input port are created at certain length of the MMI [64]. If the MMI is designed in a way, which creates images at the position of the single mode output waveguides, the device can be used for coupling, splitting or combining optical signals.
MMIs based on Si waveguides have already been implemented (see e.g. [65]). In comparison to directional couplers, they have less rigorous demands on structural resolution of the applied lithography and etching processes.

3.3.3 Mach-Zehnder interferometer

An integrated Mach-Zehnder interferometer (MZI) consists of two 3 dB couplers (directional couplers, MMIs or Y-junctions). One splits the incoming signal into the two arms of the interferometer, the other combines the signals after traveling two different ways. For a difference in optical path length between the two arms, the two signals have a phase difference Φ at the combiner. This can lead to complete reflection of the signal for destructive interference ($\Phi = \pi$) or, in the case of constructive interference, complete transmission of the signal to the output.
Therefore, MZIs are often used to build waveguide switches or optical modulators (see chapter 3.4).

3.3.4 Resonators

Interference is also the fundamental principle in resonators, which are often used as wavelength filters in optical applications.
Here, the two kinds of resonators commonly used in integrated optics are briefly described.

Fabry-Perot resonators

A Fabry-Perot resonator consists of two coplanar reflecting interfaces in a distance L.
Light is reflected multiple times back and forth between the two planes. Hence, the phase difference of the ligthwave after one revolution is $\Delta\Phi = \omega 2\mathrm{L}/\mathrm{c}$, where ω is the angular frequency. The Airy-function (3.9) describes the spectral transmittance of

the Fabry-Perot-resonator,

$$\frac{\mathrm{I}_T}{\mathrm{I}_0} = \frac{(1-R)^2}{1+R^2-2R\cos(\Delta\Phi)} \tag{3.9}$$

where R is the reflectivity of the interfaces, I_T the transmitted power and I_0 the input power.
The spectral distance between the transmission peaks are the free spectral range (FSR) of the resonator.

$$\mathrm{FSR} = \frac{\mathrm{c}}{2\mathrm{L}} \tag{3.10}$$

The relation of the linewidth $\delta\nu$ to the FSR is termed the finesse F, which is depends only on the reflectivity R.

$$\mathrm{F} = \frac{\mathrm{FSR}}{\delta\nu} = \frac{\pi\sqrt{R}}{1-R} = 2\pi \cdot N = \frac{\mathrm{c}}{2\mathrm{L}} \cdot 2\pi\tau \tag{3.11}$$

The finesse also describes the number of round trips N in a resonator, or the intensity decay time τ of the intensity build-up in the resonator after the input is switched off.
Devices based on Fabry-Perot resonators have been fabricated not only based on SOI (see e.g. [66]), but also in a-Si, where the large thermo-optic coefficient can be used to tune the filters [67].
Because of the small channel spacings of 50 GHz in dense wavelength division multiplex systems, filters with small bandwidth are necessary. This means to aim for a high finesse and FSR, which is difficult to achieve with Fabry-Perot based devices. Due to advantages in performance and easier implementation, ring resonators designed from waveguides and directional couplers as building blocks are commonly applied for filtering in integrated optics.
Because of the high refractive index difference in the case of c-Si or a-Si waveguide material, care must be take to avoid undesired reflections in the integrated optical circuits. This can for instance occur at fiber coupling, MMI in- or outputs or any waveguide imperfections, and may result in parasitic Fabry-Perot resonances.

Ring resonators

A ring resonator consist of a closed loop waveguide with two couplers for input and output. The loop has usually either the form of a circle or, in order to facilitate directional coupling, a racetrack. The lightwave travels around the loop, so that interference occurs after a distance of the ring circumference is traveled. This way,

the equations 3.10 for the FSR and 3.11 for the finesse are also valid for the ring resonator, replacing $2\mathrm{L} = \mathrm{L}_R = 2\pi r$.
The number of round trips in the resonator N and finesse F is mainly determined by the waveguide losses and coupling efficiencies instead of the reflectivity. As a performance indicator, commonly the Q factor is used rather than the finesse. The Q-factor is given by:

$$Q = \omega_r T_R \frac{\mathrm{F}}{2\pi} \tag{3.12}$$

Here, $T_R = 2\mathrm{L}_R/\mathrm{c}$ is the time for one revolution and ω_r is the resonant angular frequency.
For rib waveguides, Q factors of 119000 have been demonstrated [68], and also for smaller strip waveguides equally high values have been shown [69]. For small Si strip waveguides, ring resonators with Q-factors of 3000 have been demonstrated [69]. Dumon et al. [70] fabricated ring resonators with deep-UV lithography and measured Q-factors of $\geq$3000.

3.3.5 Bragg gratings

Bragg gratings consist of periodic modulations in the effective index along a waveguide. They are spectral filters, designed to transmit, reflect or scatter certain wavelength bands. Therefore, Bragg gratings are important for couplers or multiplexers.
The effective index changes can be produced either by lithography and etching, which means a periodic height difference of the rib, side-wall or cladding of a waveguide is created. This method is applicable on almost all integrated optical waveguide materials, and has been implemented in Si photonics with rib waveguides as well as with small photonic wires [71–73]. Due to tolerances in the order of nm and structure sizes of $\leq 150\,\mathrm{nm}$, which are required for narrow-band filters fabricated from Si, commonly e-beam lithography or deep-UV lithography [74] is applied.
Alternatively, the periodic index can be produced by a variation of the material refractive index itself, as it is done for instance in fiber Bragg gratings. In order to apply this on Si photonics, a realization with amorphous silicon as waveguide material is possible, because morphology and hydrogen content of the material can be altered by physical treatments. These parameters have significant impact on the refractive index.
Using a femto-second laser treatment on a-Si to transform a-Si into a micro - crystalline phase, gratings were fabricated by Lee et al. [75]. A Bragg grating has also

been fabricated on SOI using periodic trenches filled with a-Si, which has been recrystallized into poly-Si in order to improve its optical properties [76].

3.3.6 Photonic crystals

In contrast to Bragg gratings, the periodicity in photonic crystals is extended to two or even three dimensions.
Silicon is well suited for the fabrication of photonic crystals, because high refractive index differences result in high selectivity between transmitted wavelength and reflected wavelength in the forbidden gap, as the wavelength band, which cannot propagate, is termed.
Photonic crystals (PhC) allow for higher integration densities of wavelength selective devices, compared to devices based on total internal reflection described in the previous sections.
Due to the more straight forward processing compatible with CMOS fabrication [77], the common type of PhCs is a two-dimensional structure fabricated in SOI by lithography (a-beam or deep-UV) and dry etching.
A variety of applications have been shown and a review can be found for instance in [78].
The fabrication of photonic crystals in amorphous silicon possesses some potential advantages over c-Si. Layers deposited in low-temperature PECVD processes can be grown on almost any substrate. As proposed in [47], in combination with low index substrates, this would allow almost the same refractive indices above and below the PhC Si layer. Hence, this favorable symmetric approach would be possible without e.g. any fragile suspended PhCs. Also, in combination with planarization techniques, the fabrication of three dimensional PhCs is possible.
Two-dimensional PhCs from amorphous silicon have been already successfully implemented to fabricate optical filters [79].

3.4 Modulation

Optical modulation in integrated optics is usually achieved by a reversible refractive index change in a material, which is embedded in a waveguide of an interferometric or resonant structure.
Several mechanisms can result in refractive index changes. Most commonly, the electrooptic effect of $LiNbO_3$ is used because of the high electrooptic constant of this material. The low power consumption and high speed of this effect driven by

an applied electric field makes it ideal for high speed modulation.
However, in silicon other effects have to be exploited. Because of its crystal symmetry, Si does not exhibit a linear electrooptic effect, and higher order electrooptic effects are too weak to be effectively applied for signal modulation [80].

Free carrier plasma dispersion effect

Liu et al. [2] demonstrated GHz modulation by using the free carrier plasma dispersion effect. The charge density is controlled by a metal - oxide - semiconductor (MOS) structure embedded in a waveguide.
Various designs of devices not only based on MOS, but also on bipolar pin-diodes capable of achieving modulation by controlling the carrier concentration have since been shown, reaching even higher modulation frequencies [81].

Hybrid integration

Another way of working around the inefficient electrooptic effect in Si, in order to create an electric field modulated device based on SOI, is the hybrid approach. Polymers with high electrooptic coefficients are applied around Si waveguides, interacting with the evanescent field.
For instance, slotted waveguides are fabricated, which necessitate small feature size and fabrication tolerance. Hence, sophisticated fabrication technologies such as e-beam lithography must be applied. The advantage of this approach is, that it allows the application of polymers in the slot along the center of the waveguide, where the optical intensity can be designed to be at maximum. Thus, it has the potential to yield a high integration density [50].
An alternative fabrication method for horizontally slotted waveguides, fabricated by deposition of a a-Si:H and SiON layer stack, is presented in chapter 8.6.

Franz-Keldysh effect

A change of optical absorption in a semiconductor due to an applied external electric field is termed the “Franz-Keldysh-effect”.
A strong band bending can facilitate excitation of electrons from valence into the conduction band, resulting in an additional tail of the spectral absorption edge.
High frequency modulation can be achieved in a SiGe alloy with a band gap especially designed to maximize the electrooptic absorption due to the Franz-Keldysh effect [82, 83].

Thermooptic effect

Another way to achieve modulation in silicon is to exploit the thermooptic effect. As the thermooptic coefficient in Si is $\frac{\delta n}{\delta T} = 1.86 \cdot 10^{-4}\,\mathrm{K}^{-1}$ [84], a moderate temperature variation of a few degrees can be sufficient to achieve modulation, which allows for the implementation of thermooptic devices for switching or tuning.
In amorphous silicon, the thermooptic coefficient is higher ($2.1 \cdot 10^{-4}\,\mathrm{K}^{-1}$, [46]) and a modulation frequency up to MHz-range has been demonstrated [85].

3.5 Detection

Optical absorption with electron-hole pair generation in semiconductors usually occurs for photons with a wavelength λ corresponding to a photon energy higher than the bandgap energy E_g:

$$\lambda \leq \frac{\mathrm{h} \cdot \mathrm{c}}{E_g} \tag{3.13}$$

The bandgap energy of Si is $E_g = 1.1\,\mathrm{eV}$ and allows an absorption up to a wavelength of $\lambda = 1.15\,\mu\mathrm{m}$.
Si detectors are used for the visible spectrum or short haul communication at the near infrared around 850 nm, whereas InGaAs or Ge detectors are used for the important communication windows around 1300 nm or 1550 nm. The bandgap of Ge corresponds to a wavelength of $1.88\,\mu\mathrm{m}$ and the bandgap of the ternary InGaAs can be tailored by material composition.
In order to fabricate detectors for telecommunication wavelength in or on Si, despite the transparency of Si, several approaches are studied intensively. In general, these can be subdivided into attempts to sensitize the material e.g. by introduction of optical dopants, applying hetero - epitaxial growth of SiGe alloys, or using approaches of hybrid integration of InGaAs.

Hybrid integration of III-V semiconductors

Detectors (and also emitters) based on III-V-semiconductors can be combined with Si photonics, for example by placing them in pre-etched grooves and soldering [86, 87], or by using self-alignment of the soldering process [88].
In general, the use of discrete, well-controlled and matured fabrication technologies is an advantage of the hybrid approach and results in potentially top-performance devices.

On the other hand, technical requirements, especially due to the alignment accuracy, result in relatively high costs.

Epitaxial SiGe heterostructure

Ge or SiGe alloys can be fabricated by epitaxial growth on Si substrates. The absorption edge of these materials is at a longer wavelength compared to Si, at the same time the refractive index is higher, which also makes evanescent coupling a possible option.
A 4.2% lattice mismatch between Si and Ge crystals complicates the relization of SiGe heterostructures. A high number of defects can build up, if a certain layer thickness is reached, which is unfortunately much smaller than required for efficient detectors.
Several approaches to overcome this limitation have been pursued. For example, Ge buffer or seed layers [89, 90], cyclic annealing [91] or low-temperature deposited poly-Ge [92] have been used successfully to improve material characteristics.
One aspect, which shows how far SiGe - heterostructures are developed in comparison to other approaches, are the implementation in CMOS process flows with SOI substrates and waveguides [93].
Also amorphous Si waveguides are used to facilitate light coupling into the Ge detectors [25], and the device is fabricated using a standard 180 nm CMOS process. The SiGe is grown in trenches, which are etched into a layer stack containing the amorphous Si waveguide. Finally, the structure is planarized using a CMP process.

Incorporation of optical dopants

Erbium is mainly used as an optical dopant. Er in a Si matrix can be electrically activated and emits light at around $1.5\,\mu$m due to transitions in its $4f$-shell. It can also generate electron-hole pairs by photon absorption. This process is due to an interaction of the excited Er with Er defect-related excitonic energy levels [94].
Detectors based on SOI waveguides fabricated by Er-implant are reported to operate with an external quantum efficiency of 10^{-3} [94]. The difficulties connected with this approach are the high dopant levels needed in an integrated optical application in order to achieve reasonable absorption, which on the other hand always causes lattice defects and clustering of Er atoms. This degrades the electrical properties because of enhanced recombination and scattering of charge carriers.

Incorporation of defects

Lattice defects in Si are known to extend the absorption edge towards longer wavelength, but on the other hand also deteriorate electrical performance.
Therefore, it is a topic in research, whether a window suitable for device fabrication can be found. This requires the incorporation of mid-bandgap defect levels in a controlled way, in order to facilitate Shockley-Read-Hall generation of carriers [95]. Such devices with enhanced bandwidth are reported using a bombardment with He or Si ions and subsequent annealing [96, 97].

3.6 Light generation

Silicon is an indirect semiconductor, i.e. the minimum electronic state of the conduction band and the maximum state of the valence band are not at the same value of momentum. Any recombination with light emission has to be phonon mediated, which makes this process very improbable and consequently non-radiative recombination processes dominate. Hence, silicon is an inefficient light source.
The great potential for building passive devices and integrating photonic with electronic functionality have driven efforts to find a way to create an efficient silicon light source. Several approaches have been investigated. Next to the hybrid integration of III/V-based devices (see also previous chapter on light detection), different ways to modify the properties of silicon by quantum confinement in Si nanostructures, as well as Erbium doping, or a combination of both have been investigated [98, 99].

Quantum confinement

In order to achieve quantum confinement of electronic states in silicon, different nanostructures have been fabricated. Si nanocrystals, Si/SiO_2 superlattices or porous silicon have been used to enhance optical emission.
Ng et al. [100] used a Boron implant to create quantum confinement by a local strain field at dislocation loops. This approach has the advantage of being fully compatible with standard CMOS fabrication.

Erbium doping

By Erbium doping of Si, it is possible to achieve light emission at room temperature [101]. However, due to the presence of non-radiative recombination channels in Erbium doped Si lattice, the quantum efficiency remains limited.

Therefore, Er doping has been investigated in combination with quantum confinement, in order to enhance the interaction cross-section of Er by a resonant coupling of nanocrystal states [98, 99].

Raman amplification

A substantially different approach, which led to the demonstration of a silicon Raman laser [3], is the use of stimulated Raman scattering.
The Raman effect is a phonon - photon interaction, where an incoming photon is absorbed, while a photon with lower energy and a phonon are created under the conservation of energy and momentum. Also, the cancellation of an existing phonon and incoming photon is possible, creating a photon of higher energy. The two described spontaneous processes lead to the Stokes and anti-Stokes spectral lines, respectively. In Raman spectroscopy (see chapter 5.4), back-scattered light is spectrally analyzed in order to extract the Stokes lines stimulated by a laser source. Conclusions on materials' structure can be drawn from the spectral data.
Stimulated Raman scattering occurs when photons at both, the original "pump" wavelength and the longer Stokes wavelength are present. Dependent on the rate of the interactions, more photons of the Stokes wavelength can be created. Light intensity at the Stokes line I_s is amplified along a propagation direction Z according to the formula,

$$\frac{\delta I_s}{\delta z} = g_R \cdot I_p \cdot I_s \tag{3.14}$$

where I_p is the pump intensity and g_R is the Raman gain.
The effect has been exploited in amplifiers or lasers based on fused silica fibers. In these amorphous materials, the gain spectrum is relatively wide ($\approx 6\,\mathrm{THz}$), which makes it possible to create tunable devices. On the other hand, the relatively low gain coefficient necessitates a long interaction distance of typically several kilometers. In crystalline silicon, the Raman gain coefficient is approximately $10^3 - 10^4$ times higher than in amorphous silica. In addition, the high refractive index contrast results in much smaller modal fields, consequently creating much higher intensities. These two properties together allow for chip-size Raman amplifiers and lasers to be fabricated in Si photonics. The gain spectrum is only about 100 GHz wide due to the crystalline order, and it is located 15.6 THz below the pump frequency.
Recently, progress has been made in the reduction of free-carrier absorption, which is a gain-limiting effect. At high optical intensities, carriers in the waveguide are created by two-photon absorption. Rong et al. [102] demonstrated a continuous-wave Raman silicon laser and reduced carriers by creating the waveguide in the

depletion region of a pin-diode.
Furthermore, there is a strive to widen the possible gain spectrum. SiGe has been implemented in order to gain more flexibility [7]. Still, the application of Si alloys or structurally modified silicon in order to engineer the Raman gain spectra remains to be investigated.

3.7 Electronic - photonic integration

The possible integration with CMOS circuitry is a tremendous advantage and therefore a main reason for the thrive of Si photonics.
In any single optical function realized in Si, it can be outperformed by alternative materials: III/V-semiconductors for light generation and detection, Er-doped fiber amplifiers for signal regeneration or $LiNbO_3$ for modulation. But none of these materials possess the potential of on-chip integration with electronics, while at the same time exploiting the existing mature and industrialized technology for CMOS fabrication. Two approaches for on-chip integration of electronics and photonics exist:

Front - end integration

One is to integrate the optical waveguides and devices into the front end of a CMOS chip. The waveguides are made of c-Si in one layer with the MOSFETs.
Advantages of this approach are a possible realization of active devices, because implantation and high-temperature annealing can be applied. Using SiGe alloys or exploiting the Raman-effect to achieve optical gain is also possible.
However, disadvantages of this approach exists. Coupling light into the device is generally an issue. Butt - coupling is technologically difficult because of the involved polishing process, and wafer - level testing of the device is not possible. In addition, it would open up a way for mobile - ion contamination of the MOSFETs, which makes its application in electronic - photonic integrated circuits almost impossible. Thus, coupling orthogonal to the surface using holographic lenses is used as an alternative.
However, no metal lines are allowed above the relatively large lens area because of absorption. Thus, a significant additional wafer area is needed.
A number of devices have been demonstrated already. A 10 Gb/s photonic modulator and wavelength division multiplexer demultiplexer integrated with electronics on a single die has been fabricated in SOI technology [103].

A 10 GHz optoelectronic oscillator has been implemented [104]. Optical oscillators, which are usually realized with extensive discrete setups, outperform other high-frequency oscillators, such as frequency multiplied quartz oscillators because of their low phase noise.
Also, a 20 Gb/s optical transceiver has been integrated with electronics in a standard 0.13 μm CMOS SOI technology [105].

Back - end integration

The second approach to electronic - photonic integration is to place optical waveguides into the back - end, in a level with metal and interconnection layers of the device.
This approach is enabled by amorphous silicon as a waveguide material, which is plasma deposited and compatible with typical back - end process temperatures.
Advantages of the approach are a higher possible integration density, no process integration issues in the front - end, as well as more flexibility in finding coupling and packaging solutions.
The feasibility of small a-Si waveguides, their compatibility with planarization techniques and potential for back - end integration has been demonstrated [26, 47, 106].
Due to the disadvantages and advantages of one or the other approach, great potential also lies in the combination of both: amorphous silicon waveguides integrated in the back - end can be used to fabricate couplers, waveguides and filters, which transport the optical signal into and out of the chip and distribute it to the active devices integrated in its front - end.

3.8 The role of amorphous silicon

In the previous paragraphs, a summary of the state of the art in silicon photonics with special focus the application of a-Si is given.
Due to its compatibility with back - end CMOS processes, a-Si is becoming essential for electronic - photonic integration. A development, which was also initiated by the demonstration of low-loss single mode a-Si:H waveguides [47].
Due to its transparency and high refractive index close to the one of c-Si, amorphous silicon can be a replacement for c-Si in all kind of passive devices. For instance, it has been implemented in photonic wires and ring resonators fabricated by standard CMOS processes [107] and also in photonic crystals [79] or arrayed waveguide gratings [108].
Low temperature deposition processes allow for greater flexibility in design, the application of any substrate layers and the fabrication of stacked devices.
Furthermore, material properties such as a high thermooptic coefficient of amorphous silicon can be exploited [109, 110].
However, a lower thermal and optical stability, poorer electrical properties and lower Raman gain compared to c-Si impede the realization of active devices.
In this work, the applicability of a-Si for silicon photonics is investigated, and novel concepts exploiting the materials flexibility are developed, such as horizontally slotted waveguides (see chapter 8.6) or three dimensional taper concepts (see chapter 8.4.1).
Deposition processes are studied with respect to their influence on optical material properties (see chapter 6), and thermal post-processing is studied to further engineer materials properties (see chapter 7).

Chapter 4

Fabrication processes

This chapter firstly introduces the possible deposition techniques for amorphous silicon. The advantages and disadvantages of the different methods are briefly discussed in order to justify the investigation of only chemical methods of deposition in this work. The deposition systems used are then described in detail.
The characteristics of the obtained films are presented in chapter 6 after an introduction of the metrology applied for thin film characterization (see chapter 5).
In order to fabricate optical waveguides and devices, processes for lateral structuring are necessary. The applied lithography and etching processes are also described in detail in this chapter.

4.1 Deposition processes

Amorphous silicon can be deposited by chemical vapor deposition (CVD) as well as physical processes (PVD). In physical deposition processes such as thermal evaporation or sputtering, a vapor of the material to be deposited is created by heating or ion bombardment, respectively. No chemical reaction is involved. All materials, which are not chemically too complex, can be deposited physically.
However, these methods are mainly used for metals, because the high kinetic energies involved create bond defects in all covalently bonded materials, which is unfavorable for material quality. Another characteristic of physical deposition processes is a relatively poor step coverage.
Chemical vapor deposition processes use precursor gases, which are transformed into a solid layer by a chemical reaction. Different methods are either characterized by their pressure range (atmospheric or low pressure), or the way of providing the activation energy for the chemical reaction. This can be done thermally, optically or

by using a plasma as energy source.
Also CVD can be used for a variety of materials. For the deposition of silicon usually silane (SiH_4) is used as precursor gas. The basic chemical reaction involved is:

$$SiH_4(g) \rightleftharpoons Si(s) + H_2(g) \tag{4.1}$$

Whereas the actual subprocesses are much more complex. The silane forms a range of daughter molecules such as SiH or SiH_2, which adsorb to the surface.
The transport processes of the precursors to the proximity of the substrate surface and the desorption and removal of products are also complex and need to be well controlled.
In practice, low pressures or dilution with hydrogen or a noble gas are used to prevent early reaction in the gas phase, which may create particles and results in a poor film morphology and quality.
Hence, the most common technology for thermally activated CVD is low pressure chemical vapor deposition (LPCVD) (see 4.1.1), usually carried out at a pressure range from 10 Pa to a few hundred Pa. Also the gas flows and ratios need to be considered in order to produce a uniform film. If higher pressures are used, silan is usually diluted by hydrogen, because it also prevents nucleation in the gas phase and helps to control the process, while the hydrogen itself does not decompose in significant quantity under typical process conditions.
The films obtained by LPCVD under thermal equilibrium conditions are amorphous or poly-crystalline dependent on process temperature. As already described in chapter 2.2, they contain almost no hydrogen, which can result in a high defect density. For amorphous silicon, the best material quality in terms of low defect density and electrical performance is usually obtained from PECVD material. It incorporates a high fraction of hydrogen, because of the relatively low deposition temperatures under non-equilibrium conditions.
On the other hand, the deposition at higher temperature with LPCVD is a standard process used in CMOS fabrication in order to deposit the gate electrodes. The material contains more unsaturated bonds and a high defect density, but is more temperature stable.
The physical deposition of Si with sputtering processes is rarely used for technical applications. Not only the achievable film quality, but also the deposition rates are lower than in chemical deposition methods.
Therefore, in this work only the chemical deposition methods PECVD and LPCVD are further investigated.

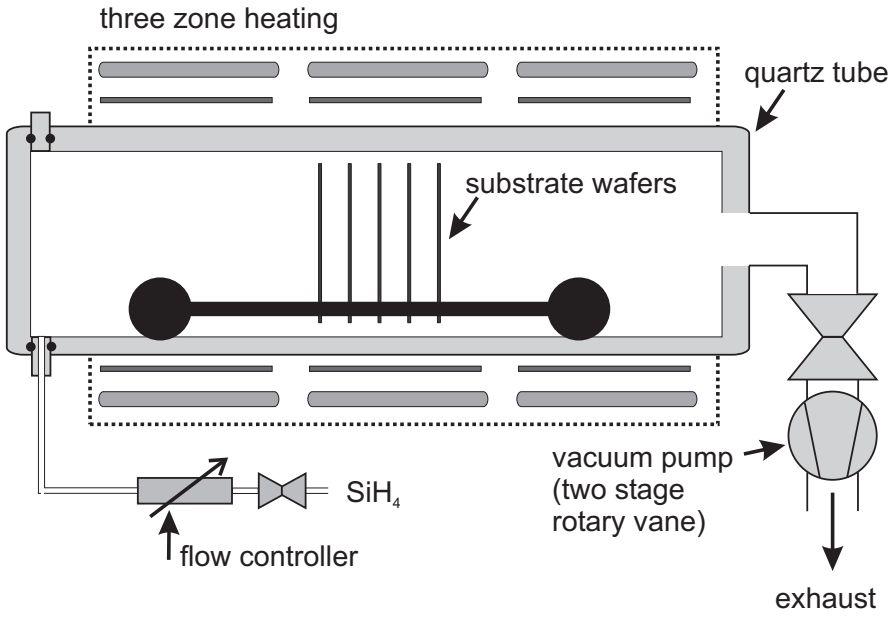

Figure 4.1: Schematic drawing of the LPCVD system.

4.1.1 LPCVD

Low pressure chemical vapor deposition (LPCVD) is commonly used to deposit highly doped poly-Si for gate electrodes and is a standard process in IC fabrication. LPCVD systems usually consist of a heated furnace to thermally supply the activation energy for the chemical reaction. To achieve a better film quality, the deposition is carried out at a low pressure.
Figure 4.1 presents a schematic of the system used in this work. It consists of a quartz tube oven with a three - zone heating system. The tube is evacuated by a two - stage rotary vane pump and the process pressure is adjusted by the silane gas flow. No gases other than SiH_4 are used. The process is carried out under reaction rate limited conditions in order to get a reasonable uniformity. The system represents the most common type of hot-wall systems used to grow poly-silicon.

4.1.2 PECVD

Plasma enhanced, or (equally termed) plasma assisted chemical vapor deposition (PECVD) systems usually consist of a reaction chamber, in which a well controlled precursor gas mixture at a low pressure is present. A high frequency electric field is applied between two electrodes and a plasma is ignited. The kinetic energy trans-

fered by collisions in the plasma delivers the activation energy for a chemical reaction, which transforms the gaseous precursors into solid products. These cause a film growth on a substrate within the reactor. A thermal non - equilibrium, where the actual substrate temperature is lower than the temperature of the accelerated and excited particles in the gas phase, allows for a deposition at reduced temperature compared to a thermal activation of the reaction.
In the deposition of Si from SiH_4 the temperature for thermal activation is above 500 °C, whereas for PECVD usually 200-300 °C is chosen to facilitate hydrogen diffusion and to improve film quality, compared to a deposition at room temperature. A variety of substrates can be used at these temperatures. Another feature of this deposition method is the feasibility to deposit effectively on large areas. Hence, PECVD is used in fabrication of TFT-displays and solar panels. It is often used for the deposition of insulation layers in back - end processes of IC fabrication, where relatively low deposition temperatures are needed in order to leave metal strip lines and front - end devices intact.
The PECVD system used in this work is schematically presented in Fig. 4.2. It consists of a parallel plate reactor with a grounded substrate electrode and a floating powered top electrode. The substrate electrode can be electrically heated up to 400 °C. The plasma generator operates at a frequency of 380 kHz and with a maximum power of 500 W. This design results in a low self-bias voltage to avoid exposure of the substrate to ion bombardment. High kinetic energies are known to result in high defect densities in a-Si:H films [9], as it is the case for PVD films.
The available precursor gases are SiH_4, NH_3, N_2O, N_2 and Ar. This configuration allows for the deposition of a-Si:H with SiH_4 with Ar as a possible dilutor. By addition of NH_3, N_2O or N_2, the deposition of SiO_xN_y with tunable stoichiometry is possible.
In any application of PECVD, the creation of particles is a major concern. To remove material deposited on the sidewalls and shower head of the reactor, a regular cleaning process is used, which uses fluorine based chemistry. Here, CF_4 with O_2 are used for this process. The oxygen prevents polymerization of CF_4, increases the fluorine radical concentration and therefore increases the etch rate.
The gas composition is controlled by setting constant gas flows, and the pressure is automatically controlled by adjusting the pump power with a butterfly valve. The vacuum pump system used is a multi-stage dry pump, equipped with an additional Roots blower delivering a total throughput of 500 m^3/h and a minimum pressure of $\approx 3 \cdot 10^{-3}$ mbar. Typical process parameters used for a-Si:H deposition can be found in chapter 6.3, table 6.1.

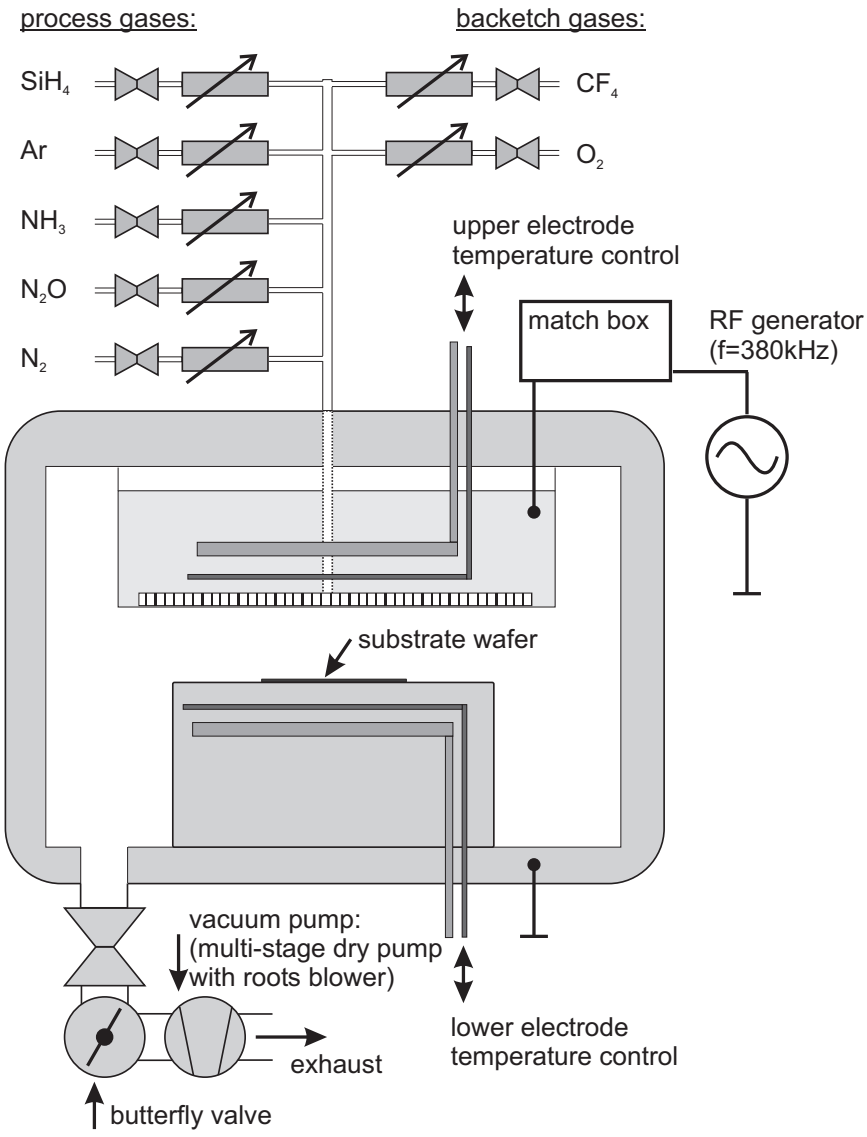

Figure 4.2: Schematic drawing of the PECVD system.

4.2 Lithography

To fabricate waveguides with lateral guidance, a pattern needs to be transfered into the waveguiding layer or cladding layer. This is done by lithography and etching. This subchapter first gives an overview of available lithography technologies with their specific advantages and disadvantages with respect to the special demands of integrated optics. The lithography systems used and processes developed in this work are described.

4.2.1 E-beam

For the development of silicon photonics , e-beam lithography is by far the most frequently used technique (see e.g. [78]). It offers flexibility to research and test different structures and offers a high resolution which meets the demands of creating nanometer scale structures.
However, being a serial process with long writing times, it is not suitable for volume production.

4.2.2 Projection

Deep - UV projection lithography at a wavelength of $\lambda = 248\,\mathrm{nm}$ is already successfully used for the fabrication of photonic crystals and nanowires [77]. It is a method suitable for mass production, and the resolution of state-of-the-art steppers is shown to be sufficient, although being on the edge with the demands of nanophotonics.
On the other hand, the disadvantages of this method are high initial costs, which require a large volume to amortize.

4.2.3 Nano - imprint

An alternative fabrication method is the currently emerging nanoimprint - lithography [111, 112]. The underlying principle of this method is to emboss the structure into a polymer using a stamp. Two ways of hardening the polymer before removing the stamp are used. “Hot embossing” with a thermoplastic or “UV-nanoimprint” with a UV-curing polymer. The latter technique necessitates a transparent stamp material, whereas the first usually uses a silicon wafer as stamp. Long heat and cool down cycles and possible inaccuracies due to the thermal expansion of materials are, on the other hand, the disadvantages of thermal imprint.
Structures down to 5 nm linewidth and 14 nm pitch [113] are reported.

Table 4.1: Process parameters for photolithography.

process step	parameters
bake	5 min at 140 °C hotplate under vacuum
spin-coat	primer TI-prime at 4500 rpm for 20 s
bake	2 min at 120 °C hotplate
spin-coat	photoresist AZ1505 at 4500 rpm for 20 s
pre-bake	60 s at 100 °C hotplate
exposure	dose 15 mJ/cm^2
post-exposure bake	30 s at 90 °C hotplate
develop	NaOH 0.5 % for 18 s at 25 °C
rinse	5 min in DI-water

Nanoimprint has already been applied for optical applications. E.g. Chaix et al. [114] demonstrated the nanoimprint of optical grids on 200 mm wafers, Belotti et al. [115] and Borel et al. [116] fabricated photonic crystals be UV-imprint with a soft mold. Compared to the other lithographic technologies, nanoimprint is still on experimental level. Molds are not readily available and it will have to be proven, that a contact method despite its problems concerning adhesion, particles and mold wear-out, will be suitable for a high volume production.

4.2.4 Contact

Mask aligners, which operate in contact mode, i.e. the mask is pressed against the resist-coated wafer during exposure, can produce small features with comparatively inexpensive equipment. Due to particle and mask wear-out problems, contact lithography is suitable for development or small volume production only.
Contact mask aligners (*Karl Suess MA4* or *EVG 620*) are used in this work. Both contact printers are capable of evacuating the gap between mask and resist - coated wafer and use the i-line ($\lambda = 365$ nm)of an mercury arc lamp. The EVG 620 can alternatively use deep-UV ($\lambda = 290$ nm).
To achieve highest possible resolution, a photoresist with very low viscosity (*MicroChemicals AZ1505*) is chosen. This photoresist results in a 500 nm layer thickness when spin coated at 4000 rpm. In practice, structures down to 500 nm are fabricated with this set up. The detailed process parameters are given in table 4.1.
After an initial bake to dry the wafer surface, a spin-on primer (*MicroChemicals Ti-prime*) is used to improve the adhesion of the photoresist. The pre-bake after the

Table 4.2: Process parameters for a-Si etch.

etch step:	
platen power, coil power	8 W, 120 W
step time, overrun	8 s, 1 s
SF_6 flow	65 sccm
passivation step:	
platen power, coil power	1.5 W, 120 W
step time, overrun	6 s, 0.5 s
C_4F_8 flow	55 sccm
start and end phase	etch
pressure	≈ 1.33 Pa (≈ 10 mTorr)

spin-coat of the resist prior to exposure is necessary to drive out solvents from the resist. A 30 seconds post-exposure bake is found to be sufficient to remove standing waves at the resist side-walls. After the development, the wafers are rinsed and spin-dried. Care has to be taken to remove all traces of developer by a long rinse in deionized (DI-)water before etching, because roughness of sidewalls and etched surface results from possible NaOH remains.
No further post-bake is done as resist stability at the successive etch step is not an issue here due to He-cooling and generally short etch process times.

4.3 Etching

After masking with photoresist, the pattern is etched into the silicon using a plasma etch tool (*Advanced Silicon Etch, ASE^{TM})* made by *Surface Technology System (STS)* [117, 118]).
The system is equipped with an inductively coupled plasma (ICP) etch chamber and helium backside cooling. Due to the ICP, a high density plasma can be obtained at low pressures, which helps to increase etch rate and improve uniformity. The possibility of independent adjustment of the ICP power and also the capacitively incoupled platen power, allows control of the density of reactive species without changing the bias voltage. Therefore, physical and chemical etch parameters can be controlled independently.
The principle of *ASE^{TM}* is to use separate alternating sidewall passivation and etch steps. During a passivation step, a flourcarbon polymer is deposited on the complete wafer surface using C_4F_8 precursor gas. In a successive etch step, this polymer is

Table 4.3: Process times for different etch depth.

etch depth [nm]	cycles	process time [s]
220	5	78
380	9	134
900	18	260

removed by an increased ion bombardment selectively from the horizontal planes, but not from the sidewalls. The SF_6 used in the etch step creates a high density of fluor radicals which reacts with silicon to form SiF_4, a gaseous end-product. A sequence of passivation and etch steps allows for high aspect ratios and etch rates. Thus, the technology is often applied for MEMS applications.
Here, the large variety of parameters which can be altered to influence the etch profiles, e.g. gas compositions of etch- and passivation step, etch times and ratio, incoupled platen and coil-powers, are used to develop a suitable process for creating waveguides from amorphous silicon films. The special requirements for such a process are: smooth sidewalls in order to reduce optical scattering losses in waveguides, a high uniformity and a low mask erosion because of the thin photoresist.
A more detailed description of *STS ASE*^{TM} can be found in [118].
The process parameters used are listed in Tab. 4.2. Comparatively low power setting are chosen to get an etch rate, which is suitable for the targeted etch depth and results in stable process times. The passivation is less pronounced, because for this application a slight isotropic etch, rather than notching or ripples at the sidewalls can be accepted.
It is found that a-Si and c-Si show a similar etch behavior, but a-Si shows a slightly higher etch rate. The process times and corresponding etch cycle numbers used for a-Si etch are presented in Tab. 4.3. One etch plus one passivation step is considered an etch cycle. Due to a break-through effect, the relation etch depth vs. time is not entirely linear.
An SEM image of the a-Si:H sidewalls resulting from the etch process described, is presented in figure 4.3.

Table 4.4: Process parameters for an anti-reflective coating.

SiH_4 flow	6 sccm
N_2 flow	982 sccm
NH_3 flow	136 sccm
pressure	73 Pa (=550 mTorr)
plasma power	80 W

4.4 Coating

The waveguiding structures fabricated by deposition, lithography and etching need to be protected against mechanical damage or dirt. This can be done by coating the device with a material, which must be optically transparent.
Here, PECVD silicon-nitride is used. It can be deposited with the system described in chapter 4.1.2. The refractive index obtained can be controlled by the process gas composition. A high flow of N_2O compared to silane produces mainly silicon oxide with a low refractive index. Using more NH_3 and N_2 shifts the stoichiometric composition towards silicon nitride with a refractive index up to n = 2. When a high fraction of silane is used, the refractive index can be raised even higher by creating a silicon-rich nitride layer.
However, losses in the critical infrared spectrum occur in the materials due to resonances with overtones of vibrations of Si-N bonds. These losses can be reduced by optimized process conditions [37].
With the waveguide concept used in this work, a-Si:H waveguide core material with a refractive index of $n_{aSi} \approx 3.5$ is used.
As the cladding layer can also be used as anti-reflective coating (ARC) on the side facets at the same time, the refractive index was tuned to a value of n= 1.87 by adjusting the deposition parameters. This refractive index value is found using Rayleigh formula,

$$n_{ARC} = \sqrt{n_{aSi} \cdot n_{air}} \tag{4.2}$$

where the refractive index of the surrounding air is $n_{air} = 1.0$.
The film thickness is 207 nm, representing a quarter wavelength in the ARC for a corresponding vacuum wavelength of $\lambda = 1550$ nm.

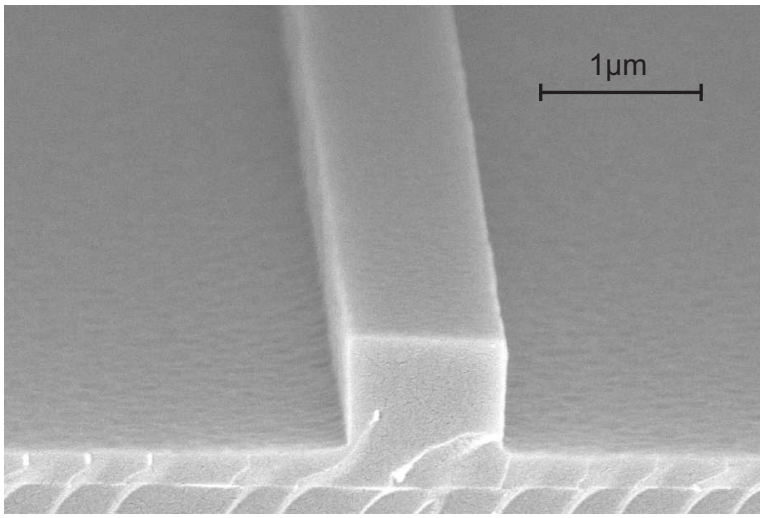

Figure 4.3: SEM image of etched a-Si:H sidewalls.

4.5 Mechanical preparation

Prior to the deposition of anti-reflective coatings, the dies need to be separated from the wafers. This is usually done by sawing and subsequent polishing of the side surface, which reduces optical loss when butt-coupling or end-fire coupling is used. For experimental purposes, cleaving of the dies is possible. In that case, care must be taken to align the waveguides with the crystals planes of the Si substrate. Cleaving of the wafer is then eased due to the crack propagation along lattice planes. A smooth surface can be obtained without a complex polishing process.
An example of a cleaved waveguide end facet (without ARC) is given in the SEM picture figure 4.3.

4.5.1 CMP

Chemical mechanical polishing (CMP) has become the standard method for planarization of wafer surfaces in back-end processes of ICs.
Multiple metal layers are separated by dielectrics and interconnects, often by chemical vapor deposited silicon oxide or nitride, as it is also used to clad the waveguide structures. Therefore, it is almost self-evident to use CMP also for global planarization of waveguide structures to allow multiple waveguide layers to be deposited on one wafer and furthermore to achieve a process integration of optical waveguides with CMOS processes.

Glasses are usually planarized using a slurry containing an alkaline suspension of SiO_2 particles and an etching agent. The size of the abrasive particles, typically ranging between $0.01 - 0.15\,\mu$m, as well as other parameters such as pad pressure and rotational speed, are usually a trade-off between removal rate and surface roughness.
Results of trials using CMP for planarization on optical waveguide layers are presented in chapter 8.5.

Chapter 5

Metrology for thin films

For the characterization of thin films, several methods are applied.
Ellipsometry is used to determine optically layer thickness or refractive index.
Fourier transform infrared spectroscopy (FTIR) is used to detect chemical bond types and chemical composition of the films. Furthermore, X-ray diffraction (XRD) and Raman spectroscopy are used to gain insight into the structural composition of the materials.
This chapter briefly introduces these measurement techniques with respect to their application on amorphous silicon. The results of the measurements are presented in the following chapters 6 and 7.

5.1 Ellipsometry

The change of polarization of light upon reflection on the sample surface is measured by ellipsometry.
As seen in figure 5.1, first a beam of linear polarized light, then, after insertion of a quarter wave plate into the beam, circular polarized light is reflected by the sample surface. In both cases, the reflected beam is analyzed by a rotating polarizer in front of a suitable detector. From the resulting sinusoidal intensity graphs, the Stokes parameters Ψ and Δ are obtained, where Ψ defines the relative change of amplitudes and Δ the phase shift upon reflection of light with polarization perpendicular (E_p) and parallel (E_s) to the plane of incidence.

$$\frac{E_p}{E_s} = \tan(\Psi) \cdot \exp(j \cdot \Delta) \tag{5.1}$$

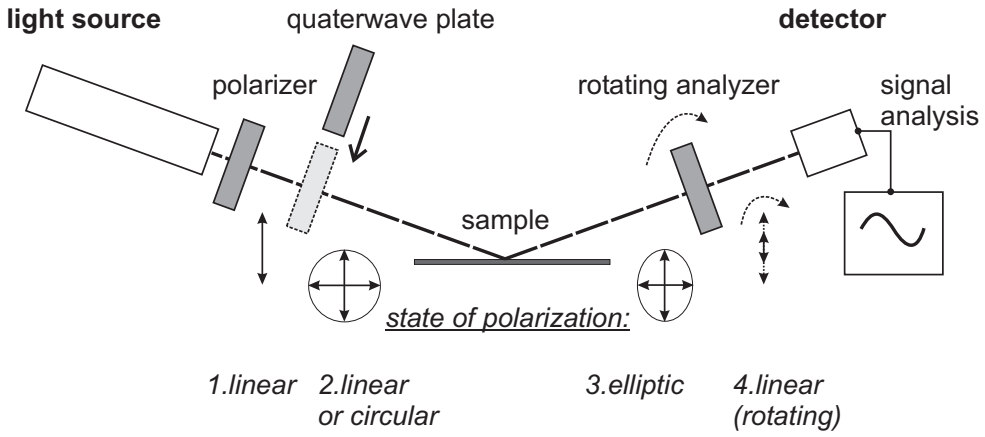

Figure 5.1: Setup of a basic ellipsometer.

By performing an iterative model analysis, i.e. calculating the stokes parameters of a layer stack with unknown thickness or refractive index parameters, the derived Ψ and Δ values are matched with the model, and so far unknown parameters are determined [119].
Care has to be taken to reduce the error of the measurement, which occurs periodically at certain wavelength. Due to the low transmission of a layer with an optical thickness of half the wavelength ($\lambda/2 = d \cdot n$), the error for the obtained refractive index or thickness one obtains under these conditions is high. To obtain reliable data, the optical thickness for ellipsometric measurements should, if possible, be chosen around approximately a quarter wavelength.
Also, the films should be homogeneous and isotropic, in order to agree with the model applied. The measurement error in layer thickness due to roughness is in the range of the roughness itself [119].
The possibility of measuring absorbing layers, such as semiconductors or metals in the visible wavelength range, is very limited. Either the complex refractive index or the thickness can be determined, if one or the other is known, and if the layer is thin enough to get a sufficient intensity from the reflections at lower interfaces.
Ellipsometry can be done using monochrome light sources, as well as scanning a wavelength range (spectroscopic ellipsometry).

5.1.1 Ellipsometry on silicon

Ellipsometry is commonly done at visible wavelength, for example at the 633 nm of a HeNe - Laser. As silicon is not transparent in this wavelength range, measurements

are complicated by a complex refractive index as already mentioned above.
It is difficult to obtain reproducible measurements at that wavelength, even for thin films. Therefore, an ellipsometer (*Horiba Jobin-Yvon PZ2000*) equipped with infrared diode laser sources of 1534 nm and 1303 nm wavelength is used.
Next to the transparency of silicon, further advantages are gained by using these wavelength. As optical communication is intended as a possible future application, the data obtained is valid for wavelength located in the c-band and o-band of the optical fiber transmission windows.
Besides that, the longer wavelength also extends the range of layer thickness, which can be measured until the periodicity of the obtained stokes parameters has to be taken into account. If the optical thicknesses of layers extend half the measurement wavelength ($T \geq \lambda/(2n)$, the obtained results are virtually the same as for a layer, which is smaller by that amount.
The high refractive index of silicon compared to glasses facilitates the measurement, in case a glass such as SiO_2 is used as a substrate layer. Because the standard substrate is a silicon wafer, an additional layer becomes necessary. Here, thermally grown oxide is used.
To determine all parameters for the model accurately, the silicon oxide layer thickness and refractive indices are always measured at all available wavelength prior to deposition. Measurements of amorphous or poly-silicon on wafers without any glass layer were found to be inaccurate due to the low refractive index difference to the silicon substrate.
For the layers as well as etch processes used here, surface roughness is found to be insignificant for the ellipsometric measurements.

5.2 FTIR

Fourier transform infrared spectroscopy (FTIR) is a method to analyze the chemical composition of a material.
Light of a broad-band IR source is split up in a Michelson interferometer. One beam is passed through the sample, which can be in solid, liquid or gaseous state, and recombined with the reference beam on the detector to obtain the interferogram. By conducting a Fourier analysis, the obtained data can be transformed into the wavelength range.
The excitation of vibrations in chemical bonds causes characteristic absorption peaks, and the chemical composition can be derived.
Customarily in spectroscopy the obtained signal is plotted versus a wavenumber,

and the measurement range is usually about 5000 to 150 cm^{-1} wavenumbers.
The intensity decay follows the Lambert-Beer law,

$$\mathrm{T} = \frac{\mathrm{I}}{\mathrm{I}_0} = 10^{-\sigma \cdot N \cdot d} \tag{5.2}$$

with T being the transmittance, σ the absorption cross section, N the density of absorbers and l the optical path length.
With a known absorption cross section and optical path length (i.e. sample thickness), the concentration of an absorbing bond can be determined from the absorption $A = \sigma \cdot N \cdot d$ by integration of an absorption peak.

5.2.1 FTIR on thin amorphous Si films

Thin films need to be deposited on a substrate. As FTIR spectra are usually obtained in transmission, it is important to use a substrate, which does not significantly absorb any spectral region of interest.
For the characterization of thin amorphous silicon films, we chose high ohmic, p-doped, double-side polished wafers without any further interface layers. The wafers are cleaned by a dip in hydrofluoric acid prior to deposition. Wafers with a rough backside reduce the signal due to scattering. Low-ohmic, n-doped wafers reduce the signal by absorption. Oxide layers on the wafer surface may deteriorate the obtained spectra due to absorption of Si-O bonds, as well as additional Fabry-Perot resonances.
For the measurements in this work, a FTIR - interferometer type *Perkin-Elmer 1800* is used.
The information derived from FTIR on amorphous silicon layers mainly contains the types of the present Si-H bonds. A list of molecular groups, their vibrational modes and corresponding wavenumber is presented in Tab. 5.1.
Their density can also be derived because corresponding absorption cross-sections can be found in literature (see Tab.5.2).
In addition, from the FSR of Fabry-Perot resonances of the layer, one can determine the refractive index or the layer thickness, if one or the other is known.
A typical FTIR spectrum of an a-Si:H film is presented in Fig.5.2.

Table 5.1: Vibrational modes and wavenumber of Si-H bonds [10].

group	vibrational mode	wavenumber [cm^{-1}]
SiH	rocking	630
SiH	stretching	2000
SiH_2, SiH_3	bending	$880 - 905$
SiH_2, SiH_3	stretching	$2090 - 2140$

Table 5.2: Absorption cross-sections for Si-H bonds' absorption bands.

absorption band at wavenumber	absorption cross-section	citation
$630\,cm^{-1}$	$1.6 \cdot 10^{19}\,cm^{-2}$	[120]
$2000 - 2100\,cm^{-1}$	$1.4 \cdot 10^{20}\,cm^{-2}$	[121]
$800 - 900\,cm^{-1}$	$2.0 \cdot 10^{19}\,cm^{-2}$	[121]

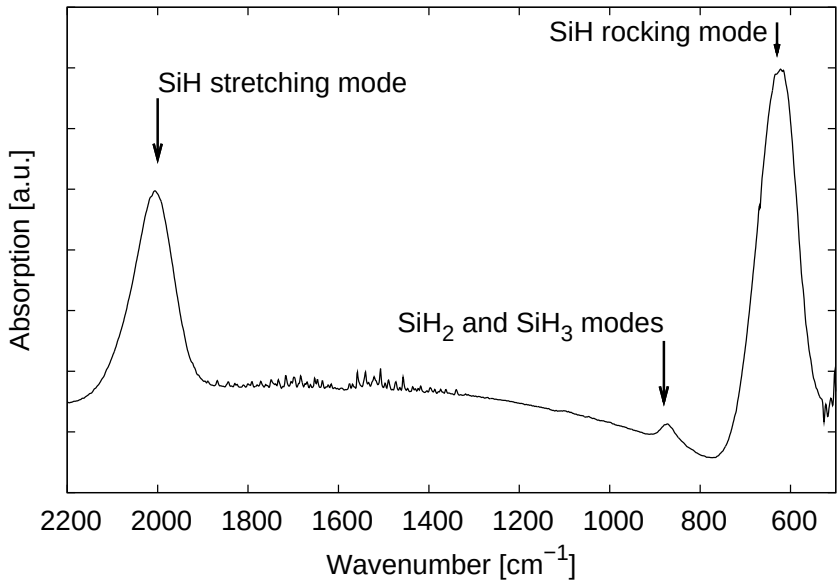

Figure 5.2: Typical FTIR spectrum of a-Si:H.

5.3 XRD

The interatomic distance in a solid is in the order of 10^{-10} m. To analyze its atomic order, an electromagnetic wave of a wavelength, which is just as short, must be used. This corresponds to photon energies of several keV ($\hbar\omega \approx hc/10^{-10}\,\mathrm{m} \approx 12.3\,\mathrm{keV}$), which are in the X-ray spectral range.
In materials with a high degree of atomic order such as crystals, for certain wavelength and incident directions, intensity peaks of scattered radiation are observed. This was first explained by W. L. Bragg as the constructive interference of waves being reflected from parallel planes of atoms in the solid.
The condition for constructive interference is met for a path difference of $2\mathrm{d}\cdot\sin\theta$, where θ is the angle of incidence and d the planes' distance, equal to an integral number of wavelength $n\lambda$. This is known as the Bragg condition:

$$n\lambda = 2\mathrm{d}\cdot\sin\theta \tag{5.3}$$

In X-ray diffraction (XRD) measurements, the incident angle θ is scanned through a certain range while the reflection intensity is recorded. From the peaks measured, one can draw conclusions on the crystallinity of the material, the material composition and kind of the crystals, as well as the grain size derived from Scherrer equation,

$$t = \frac{K\cdot\lambda}{\beta\cdot\cos\theta} \tag{5.4}$$

where t is the grain size, β the peak width at half maximum and K a form factor. Results of XRD measurements on a-Si:H films are presented in chapter 7.2.3.

5.4 Raman spectroscopy

Raman spectroscopy is an optical measurement of phonon spectra.
In matter, photons are scattered due to the Raman effect, while phonons are emitted or absorbed. The energy shifts caused by phonon interaction are small, due to the relatively small phonon energies (range of tens of meV) compared to the photon energies (range of eV). On the other hand, the momentum of a photon is rather small compared to the phonon. Therefore, the interaction takes place only in the neighborhood of the center of the Brillouin zone ($\vec{\mathrm{k}} \approx 0$). A high intensity laser source for excitation, and interferometric techniques for detection of the effect are necessary.
Scattering with emission of a phonon is referred to as the Stokes component and

expressed by the negative sign in the laws of conservation of energy (5.5) and momentum (5.6). Absorption of a phonon is referred to as anti-Stokes component and expressed by the positive sign.

$$\hbar\omega_2 = \hbar\omega_1 \pm \hbar\omega_s(\vec{\mathrm{k}}) \tag{5.5}$$

The energy of the phonon is given by $\omega_s(\vec{\mathrm{k}})$ and the energies of the photon by $\hbar\omega_x$, where $x = 1$ represents the incoming and $x = 2$ the scattered photon.

$$\hbar n\vec{\mathrm{q}}_2 = \hbar n\vec{\mathrm{q}}_1 \pm \hbar(\vec{\mathrm{k}} + \vec{\mathrm{K}}) \tag{5.6}$$

The momentum of the phonon is given by $\hbar(\vec{\mathrm{k}} + \vec{\mathrm{K}})$ and the momentum of the photon by $\hbar n\vec{\mathrm{q}}_x$. Because the photon wave vectors $\vec{\mathrm{q}}_x$ are small in magnitude compared to the Brillouin zone, the momentum conservation law can only be obeyed, if the reciprocal lattice vector $\vec{\mathrm{K}}$ is zero and $\vec{\mathrm{k}}$ close to zero as mentioned above.
Usually, Raman spectra are plotted as intensity versus wavenumber of the wavelength or frequency shift. Information about degree of atomic order or stress in a material can be derived.
Results of measurements on a-Si:H thin films are presented in chapters 2.4 and 7.2.3.
The measurement system used in this work is a *Horiba Jobin-Yvon HR800* Raman spectrometer.

5.5 AFM

An atomic force microscope (AFM) creates a truly three-dimensional image of a sample surface by scanning a probe over it.
The probe usually consists of a cantilever with a sharp tungsten tip. The diameter of the tip defines the resolution and is usually in the order of nm. The forces between tip and sample surface bend the cantilever, and its deflection is optically measured by recording the position of a laser beam reflected from the cantilever with an array of photo-diodes.
The AFM is best suited to determine surface roughness, because it delivers accurate, three-dimensional data of the sample surface. Further advantages over scanning electron microscopes (SEM) are the relative low costs and ease of use, because no vacuum system and no special sample treatment is necessary. It also potentially provides a higher resolution than SEM.
An AFM (type *DME Rasterscope 3000*) is used in this work to determine surface morphology and roughness of amorphous Si layers (see chapter 6.1.4).

Chapter 6

a-Si:H thin films

In this chapter, the characteristics of a-Si:H layers deposited mainly by PECVD are presented. Important properties for the intended application in integrated optics are studied with respect to deposition parameters. For instance, intrinsic stress is relevant for process integration. Surface roughness may create optical scattering losses and must be minimized. The refractive index, which is sensitive to film composition, must be well controlled.
An optimum deposition process is determined by design of experiment. However, this is a trade-off between favorable and unfavorable effects for some deposition parameters.
The characteristics of LPCVD layers are also briefly described for comparison.

6.1 Effects of PECVD process parameters

6.1.1 Pressure

Process pressure has an influence on the resulting layer properties by different modes of action. Generally, the density of gas particles is reduced and mean free path length is increased for lower pressure. This leads to a higher kinetic energy obtained by the ions when accelerated in the electric field, which builds up at the substrates' surface ("self-bias"). Weak atomic bonds might be broken and re-arranged under this growth conditions. One may expect an influence on films stress as well as composition, especially on hydrogen content.
The lower density of reactive gas molecules simply leads to a lower deposition rate. On the other hand, other unfavorable effects, such as particle formation through gas phase reaction or micro-void formation in the layer must be avoided by finding an

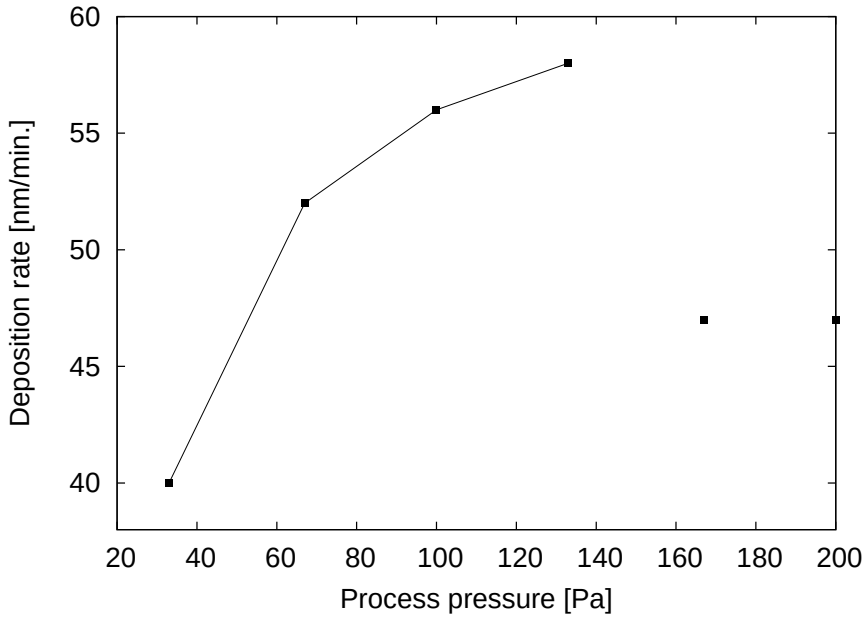

Figure 6.1: Dependence of deposition rate on process pressure.

optimum process pressure.

Effect on stress

Layer stress is determined qualitatively by measuring substrate bow after deposition.
The layers all show compressive stress, as can be expected from literature (see chapter 2). The stress was found to be minimal around a process pressure of 133 Pa (= 1 Torr).
The process window of the PECVD system used here is in the range of 25 to 165 Pa. This means, in order to sightly reduce the stress, the system would have to be operated close to its upper pressure limit, which is not favorable due to stability issues.

Effect on deposition rate

The deposition rate for processes at different pressures is presented in figure 6.1. One can see a non-linear increase with saturation towards higher pressures. The drop for pressures above 150 Pa is believed to be caused by plasma stability issues at the upper limit of the process window of the deposition system.

Effects on hydrogen content

The effect of process pressure on further characteristics of the layers are less pronounced. There is no significant impact found on the hydrogen content.

6.1.2 Temperature

The substrate temperature has an impact on the hydrogen content and the saturation of dangling bonds with hydrogen during growth.
Choosing an elevated temperature around 300 °C allows hydrogen diffusion, so that dangling bonds created at the growth interface can be saturated effectively (see chapter 2.2). Weak C-H bonds start to decompose and rearrange at higher temperatures, and the density of hydrogen decreases causing the dangling bond density to increase.
The dependence of hydrogen content measured by FTIR (see chapter 5.2) on process temperature is presented in figure 6.2. The density of bonded hydrogen is found to be reduced with temperature over the whole temperature range between 200 °C and 400 °C. This is believed to be caused by the minimized self-bias and ion energy in the system used here.
Creation of dangling bonds due to ion bombardment, which necessitates diffusion in order to saturate bonds, is not seen. Hence, the decomposition of weak C-H bonds at higher temperatures is the predominant effect.
Further significant effects of the process temperature on other material characteristics are not found.

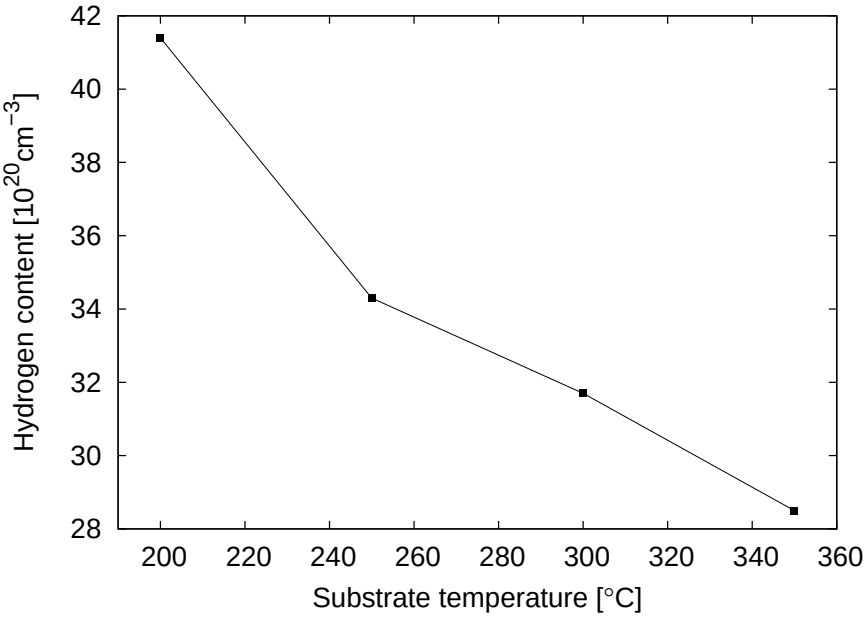

Figure 6.2: Dependence of hydrogen content on substrate temperature during deposition.

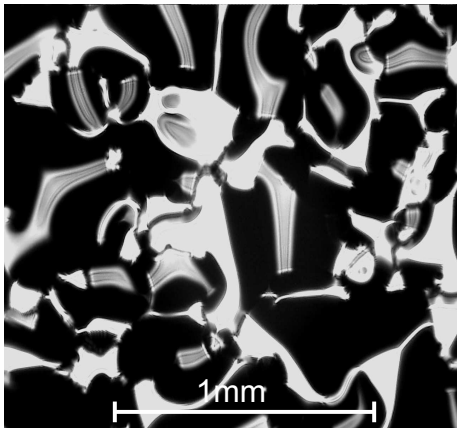

Figure 6.3: An optical microscope image of a layer surface deposited with pure silane shows macroscopic areas of delamination and cracks.

6.1.3 Gas composition

Usually a-Si:H films are deposited from pure SiH_4 or SiH_4 diluted with H_2 (see chapter 2.2). In the specific PECVD system used here (see chapter 4.1.2), with its low frequency power source and a reactor geometry designed to minimize ion bombardment, deposition processes with pure SiH_4 result in layers, which show delamination and cracks (see figure 6.1.3), because of a too high compressive stress. Therefore, a slight dilution of SiH_4 with Ar is chosen, because it results in films, which are mechanically stable, though they are still under significant compressive stress.

Effect on refractive index

When using Ar instead of H_2 to dilute the SiH_4 precursor gas, the possibility of creating more dangling bonds exist. This is because an increased concentration of unfavorable higher order radicals (SiH_2, SiH) can be caused by energy transfer mechanisms between Ar and SiH_4 in the plasma (see chapter 2.2.1). A possible effect on material properties could be a refractive index increase with Ar percentage.
Films are deposited with different SiH_4 to Ar ratios and their refractive index is measured by ellipsometry at $\lambda = 1534\,\text{nm}$ wavelength. Fig. 6.4 shows the refractive index of the a-Si:H. It is almost constant for a SiH_4 ratio greater than approximately 2%. Below that, the refractive index increases significantly, which points to a higher density of defects.

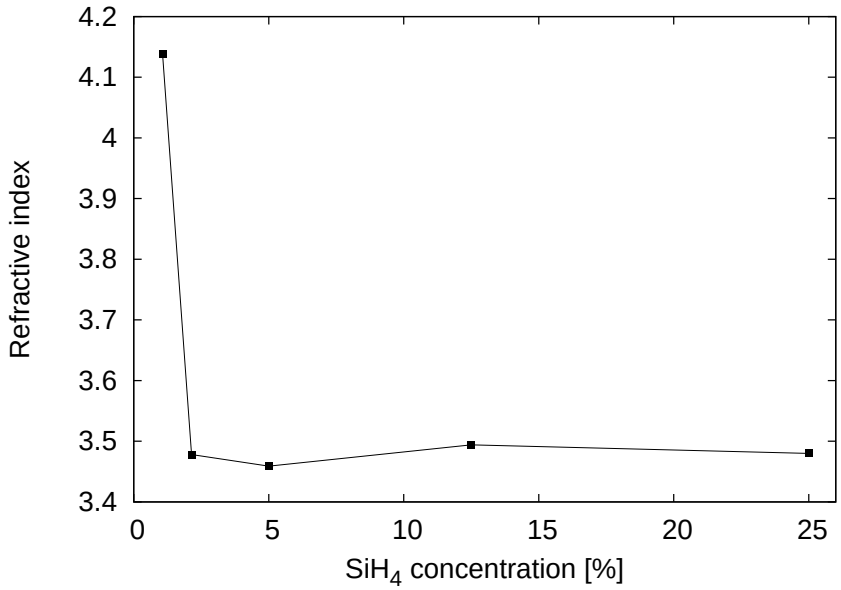

Figure 6.4: Dependence of refractive index on silane concentration in Ar.

Effect on hydrogen content

In addition, FTIR measurements are carried out on samples deposited with a SiH_4 ratio ranging from 100% to 25%.
A maximum hydrogen concentration was found at 50% SiH_4 ratio (see figure 6.5).

Effect on deposition rate

As it is shown in figure 6.6, the deposition rate increases non-linearly with a saturation towards higher SiH_4 ratio.
This is due to the effect of dilution with the less silan precursor available for film growth.

Effect on surface roughness

Being one of the most important parameters for the intended application in integrated optics, the obtained surface roughness is studied in detail.
In general, parameters with major influence on growth rate are believed to have potentially also an influence on the obtained surface roughness. Thus, effects of silane dilution and also RF power (see chapter 6.1.4) are investigated.

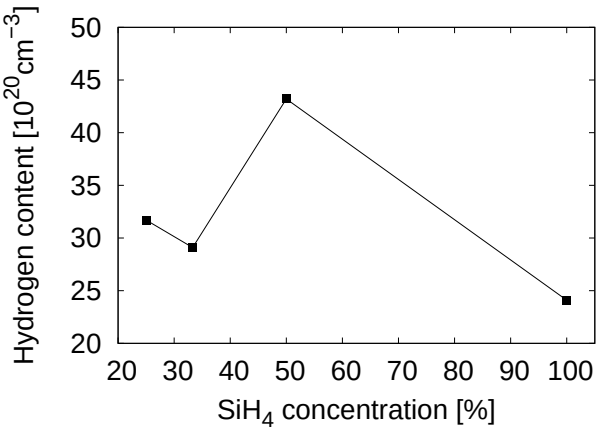

Figure 6.5: Dependence of bonded hydrogen on silane concentration in Ar.

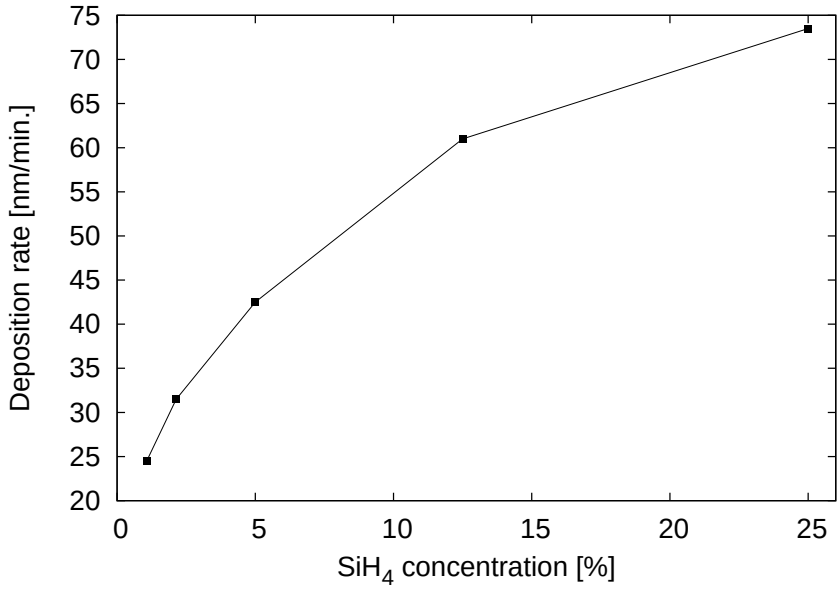

Figure 6.6: Deposition rate for silane dilution with argon (ellipsometric measurement).

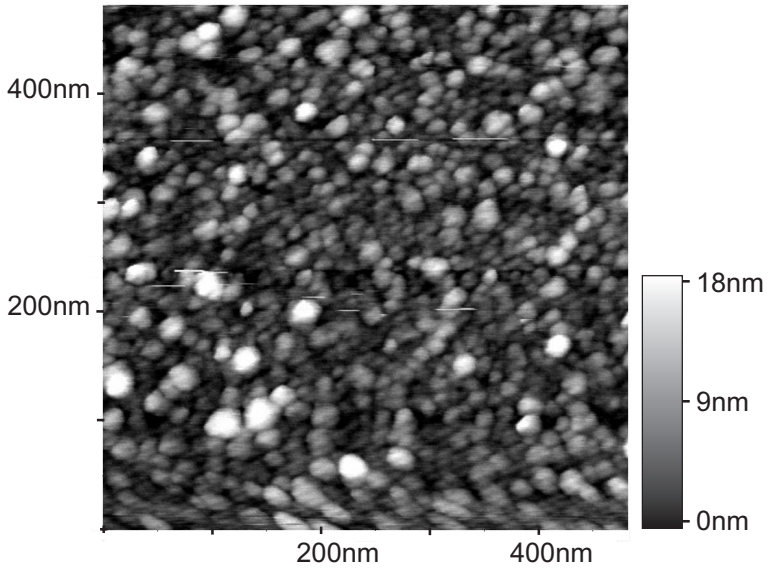

Figure 6.7: Typical surface profile from AFM measurement (sample deposited with 5% SiH_4 in Ar).

Surface profiles are obtained by scanning with an atom force microscope (AFM, see chapter 5.5). Figure 6.7 represents a typical surface profile of an as-deposited a-Si:H layer. One can see hillocks, which extend in the range of tens of nanometer in width, as well as in height. Between these hillocks some voids in the nm-range are found. The AFM surface profiles are measured for different silane ratios, and the RMS roughness and correlation length are determined from the data.
In figure 6.8, the result is presented. Roughness and correlation length are reduced for 5% and 12.5% silane content compared to 25% silane content. For gas compositions below 5% silane, the measured values are believed to be irrelevant. Due to the low deposition rate and the increased defect densities, these parameters cannot be used practically.

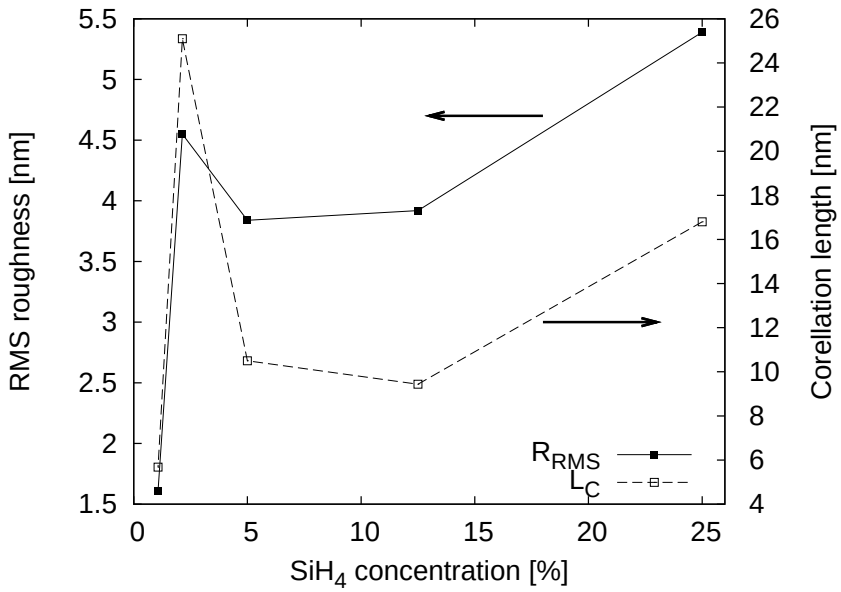

Figure 6.8: RMS roughness and correlation length dependence on SiH_4 concentration in Ar.

6.1.4 Plasma power

The PECVD system used here (see chapter 4.1.2) is equipped with a generator operating at a frequency of 380 kHz and a maximum power of 500 W.
Due to the lower mass of electrons compared to ions, they gain a higher speed in every half period of the voltage applied to the systems' electrodes. In consequence, more electrons reach the electrodes. A positive space charge in the plasma and an electric field perpendicular to the electrode and substrate surface results, which accelerates ions toward the substrate surface.
The applied AC voltage and the superimposed self bias change with power and frequency. In that way, by changing kinetic energy and density of different ions, both parameters influence the growth conditions and material properties of the film. The effect of plasma power on deposition rate, surface roughness and hydrogen content is studied.

Effect on deposition rate

Typically, a linear relation of deposition or etch rate with incoupled plasma power is found in plasma deposition or plasma etch processes. As seen in figure 6.9, this is the case up to a power of 250 W.
For higher powers this relation does not hold for the system used here. The reason for the lower than expected growth rate is believed to be the observed plasma instabilities, rather than a possible depletion of radicals. I.e. at high power levels, plasma is found to ignite not only between electrodes, but also between electrodes and sidewalls.

Effect on surface roughness

To measure the effect of plasma power on the surface roughness, two samples are compared. Figure 6.10 shows the surface profiles measured by AFM of samples deposited at a power of $P_1 = 100\,W$ and $P_2 = 250\,W$. The surface roughness increases slightly, but the correlation length increases significantly for the sample deposited at higher power.
This can be explained by the higher density of reactive particles in the plasma at higher powers, which leads to a faster growth of fewer hillocks resulting in the higher roughness observed here.

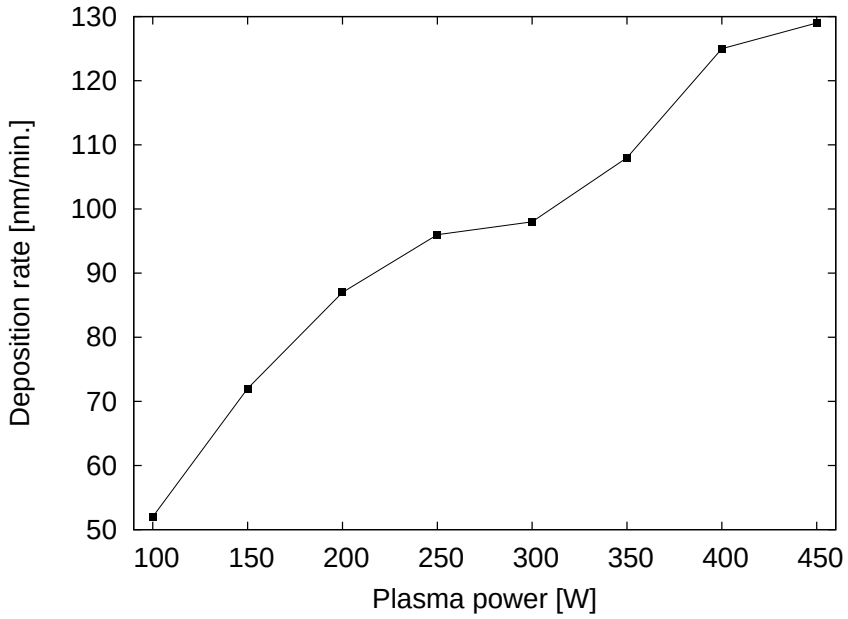

Figure 6.9: Dependence of deposition rate on plasma power.

Effect on hydrogen content

The hydrogen content is found to be roughly constant for plasma power less than 200 W. Above that, the hydrogen content drops by more than 50% and is again constant on the lower above 300 W.
A possible explanation for this is an increased ion bombardment and the higher growth rate, reducing the ability of hydrogen diffusion in saturating the defects.

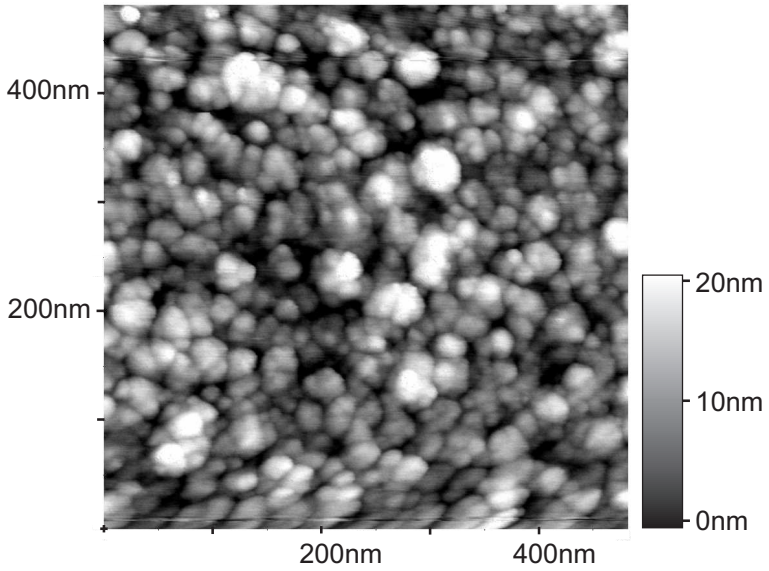

(a) Sample deposited at P_1=100W. The resulting RMS roughness and correlation length are 5.39nm and 16.8nm, respectively.

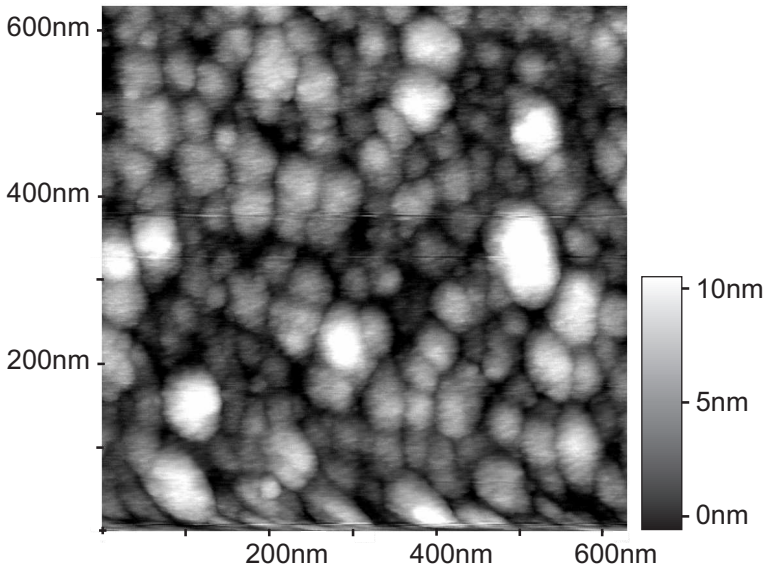

(b) Sample deposited at P_2=250W. The resulting RMS roughness and correlation length are 5.59nm and 46.2nm, respectively.

Figure 6.10: AFM surface scans of samples deposited at different plasma powers.

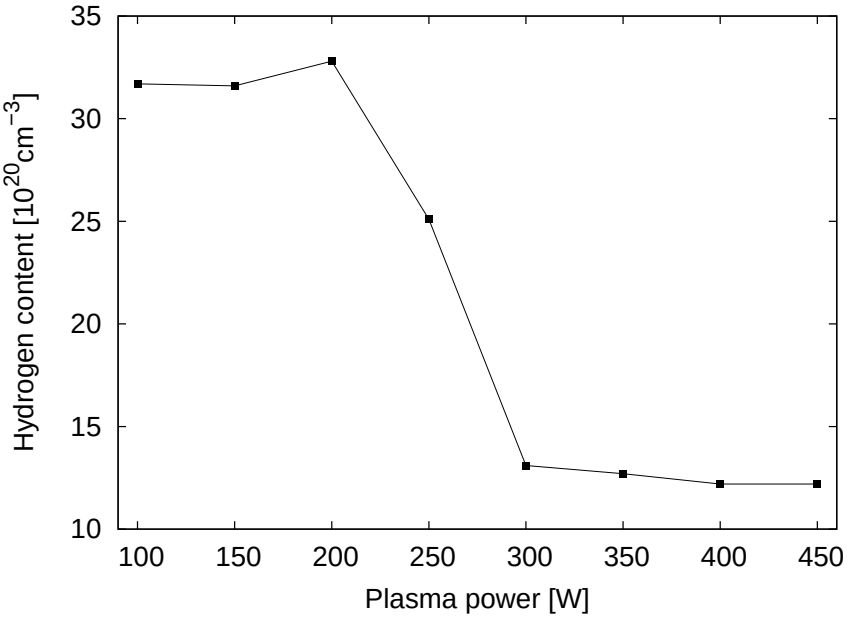

Figure 6.11: Dependence of hydrogen content on plasma power.

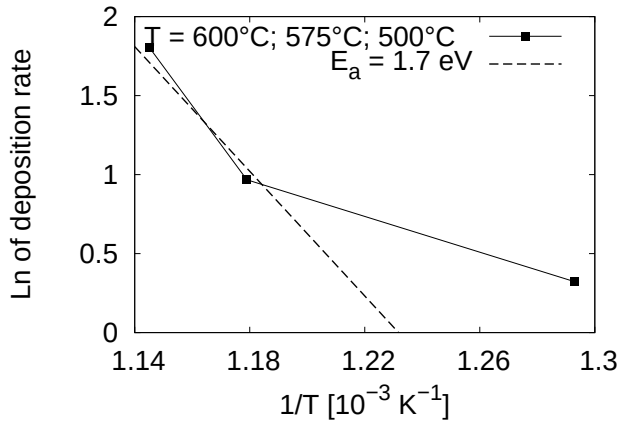

Figure 6.12: Arrhenius plot of the deposition rate of Si.

6.2 Properties of LPCVD thin films

The activation energy in LPCVD is provided by temperature only (see chapter 4.1.1). Hence, a main parameter to control layer properties is temperature.
Any dilution or mixture of the silan precursor with other gases would decrease the growth rate and more likely produce poly-crystalline layers.
The pressure also mainly reduces the growth rate and has a secondary effect on the morphology.
For a process temperature below 600 °C, the deposited silicon is usually amorphous but can also be mixed or polycrystalline, if the deposition rate is low [122, 123].
In this work, samples are deposited at temperatures below 600 °C, because poly-crystalline layers resulting at higher temperatures are, due to their grain boundaries and surface roughness, not suitable for application in passive devices.
The deposition rate in this temperature driven process has to obey the Arrhenius relation (see figure 6.12). However, in the given system, temperatures below approximately 550 °C could not be well controlled, which results in a higher than expected growth rate, probably due to a temperature above setpoint.
The measured hydrogen content of all samples is zero, which indicates a large density of unsaturated bonds. Also, a measured high refractive index of n $\approx$ 3.75 compared to PECVD a-Si:H (n $\approx$ 3.5) indicates this.
The low temperatures, which have to be used in order to obtain a suitable morphology, result in very low deposition rates.

Table 6.1: Standard deposition parameters.

Process parameter	PECVD	LPCVD
Temperature	300 °C	600 °C
Power, frequency	250 W (100 W), 380 kHz	-
SiH_4 flow	70 sccm	80 sccm
Ar flow	210 sccm	-
Pressure	66.7 Pa (= 500 mTorr)	64 Pa (= 480 mTorr)

6.3 Optimized process

For further investigation and fabrication of waveguides (as presented in chapter 8), the process parameters in table 6.1 are chosen.

PECVD process

The process temperature of 300 °C allows hydrogen diffusion, but on the other hand, is not too high so that weak hydrogen bonds are broken.
The RF power of 100 W is a trade-off between a high enough deposition rate and a low surface roughness. Furthermore, the hydrogen content at this value is high and the plasma conditions are stable.
The silan content of the process gas of 25% is a trade-off between reasonable deposition rate and surface roughness. It results in a relatively high hydrogen content and low refractive index, indicating a suitable optical quality.
A pressure of 66.7 Pa is chosen to obtain a high deposition rate, stable plasma conditions and a good uniformity.
The low frequency plasma is likely to reduce defects caused by ion impact. The measured drop of hydrogen content at higher plasma powers above 250 W (see figure 6.11) indicates an increased defect density.

LPCVD process

For the LPCVD process, both temperature and pressure are a trade-off between reasonable deposition rate and suitable film morphology.
In general, the obtained characteristics for LPCVD films indicate that these films are less suitable for the intended application in integrated optics than PECVD films.

6.3.1 Uniformity

The uniformity U of a parameter x is calculated according to the common definition:

$$\mathrm{U} = \frac{\max(x) - \min(x)}{2 \cdot \mathrm{mean}(x)} \cdot 100\% \tag{6.1}$$

For the optimized PECVD process (see Tab. 6.1), the uniformity over the surface of a 100 mm-wafer is $\leq 6\%$ for the deposition rate and resulting layer thickness, with one extremum usually at the wafer edge. The uniformity for the measured refractive index over the wafer is typically $\leq 2\%$. If the omitted radius at the wafer edge is increased from approximately 1.5 mm to 4 mm, the uniformity for the refractive index decreases to typically $\approx 1\%$.
Films deposited by LPCVD were significantly less uniform. This was mainly due to inhomogeneous silane flow in the space close to the wafer boat.

Chapter 7

Thermal postprocessing

The amorphous silicon layers deposited by PECVD or LPCVD as described in the previous chapter are annealed at temperatures above deposition temperatures. This is done to provoke structural and, as in the case of PECVD layers, also compositional changes. These can occur by the rearrangement of weak atomic bonds, the out-diffusion of hydrogen and, at temperatures above approximately 600 °C, by the onset of crystallization.
The focus is to study the impact on optical parameters such as refractive index, absorption and scattering, as well as the structural changes with influence on phonon spectra. This is done with respect to possible future applications, for instance of the Raman effect in integrated optical waveguides.

7.1 Methods of thermal annealing

The main parameters in thermal anneal processes are temperature ramping times, maximum temperature and holding time. The processes are carried out under inert gas atmosphere or vacuum to avoid oxidation or other chemical reactions.
Several methods of thermal annealing are applied in microelectronic or photovoltaic fabrication.
For instance, quartz tube ovens can be used for relatively slow ramping times.
Originally developed for the purpose of dopant activation and damage annealing after ion implant, the family of rapid thermal anneal processes (RTA, also referred to as rapid thermal processing RTP) aims to minimize the thermal budged by reducing time at temperature and increasing ramping rates. This is done to reduce a spread of doping profiles by diffusion in small-scale devices.
A common type of RTA systems uses arrays of tungsten-halogen lamps to evenly

heat the wafer. Other systems use light pulses or scanning of a high intensity light or electron beam from a high-power CO_2-laser or electron source, respectively. Because of defects caused by large lateral thermal gradients and also due to the systems' cost and complexity, the application is mainly restricted to research.

Oven annealing

Here, a horizontal quartz tube oven with nitrogen atmosphere was used for the standard anneal processes. The temperature ramp-up and -down rates are approximately 1 K/s.
A process with a minimum possible holding time at top temperature is chosen in order to suppress further growth of crystalline grains, which might be unfavorable for optical application. On the other hand, to allow for a sufficient temperature stabilization within the oven, this minimum holding time is 10 minutes.

Rapid thermal annealing

A RTP system type *AST SHS 100* is applied. In this system, the wafer rests on quartz pins and is heated by two arrays of tungsten-halogen lamps above and below the wafer. The temperature is controlled by a pyrometer. Processes are run under nitrogen atmosphere. The temperature ramp-up and ramp-down rates are set to $15 - 40$ K/s.
A minimum holding time at the top temperature is chosen. In order to allow for a sufficient stabilization, this interval is 5-10 seconds, depending on maximum temperature level.
First, control parameters are carefully set to avoid any temperature overshoot above setpoint.

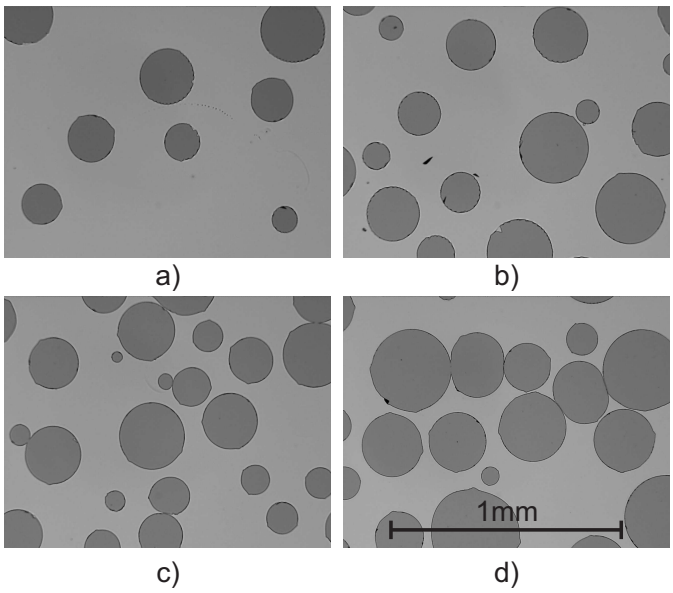

Figure 7.1: Circular delaminated areas of a 0.7 μm thick a-Si:H film after thermal postprocessing in a quartz oven. Hole density and size increases from (a)700 °C, (b)800 °C, (c)900 °C to (d)1000 °C.

7.2 Effects of thermal annealing

7.2.1 Effect on surface morphology

LPCVD films are temperature stable, and no damage is observed in the temperature range below 1000 °C used here.
PECVD films show cracks and holes at anneal temperatures above 650 °C, both for the standard as well as rapid thermal anneal processing. In figure 7.1, images of the surfaces of standard annealed samples are shown. The density of holes increases with temperature above 700 °C.
The degree of damage also depends on the film thickness, where thin films are found to be more stable.

7.2.2 Effect on hydrogen content

Hydrogen content is determined by FTIR (see chapter 5.2) both for the as-deposited, as well as oven-annealed samples.
The as-deposited LPCVD samples do not contain any measurable amount of hydrogen, whereas the hydrogen content in PECVD samples is relatively high (see chapter

6).
The oven anneal process at 600 °C substantially reduces the hydrogen content, and for anneal temperatures above 700 °C the hydrogen content is not measurable any more.
The hydrogen content in RTA samples is not measured. Here, the related optical parameters are studied (see chapter 7.2.5).

7.2.3 Effect on structural order

Main effects of thermal treatments on amorphous silicon films are the rearrangement of weak bonds and the onset of crystallization, with crystallite grain size increasing with thermal budget.
The degree of crystallinity is evaluated by x-ray diffraction (XRD, see chapter 5.3). Both quartz-tube oven as well as RTP processed samples are studied.

Oven annealing

On (100)-oriented substrate wafers with 3.0 μm thermal oxide, a-Si:H film with a thickness of 1.0 μm are grown by the PECVD process described in chapter 6.3. XRD spectra are recorded of as-deposited as well as oven-annealed samples.
From the data presented in figure 7.2, an estimation for the grain sizes is derived using the Scherrer equation (see chapter 5.3, equation 5.4).
To obtain the average crystallite grain size t, from the measurement data diffraction angles at center of peak ϑ and the full width of the peaks at half maximum intensity (FWHM) β are extracted. The wavelength of the x-ray emission line λ is $1.5405 \cdot 10^{-10}$ m, because the copper line Cu Kα_1 is used. The measurement dependent form factor K is assumed to be one.
The average crystallite grain sizes t calculated accordingly are presented in table 7.1.
In the XRD spectra, one can see peaks with increasing intensity toward higher anneal temperatures. These peaks can be related to the (111), (220) and (311) Si crystal planes. Position as well as relative intensities are in good agreement with literature [124].
The broad peak around 30-35 ° is attributed to the presence of SiO_2.
The as-deposited PECVD samples do not show any peaks and are believed to be completely amorphous. The crystallite sizes of a range < 30 nm is assumed to be caused by the high density of defects and crystal nuclei, in combination with the short annealing times used here.

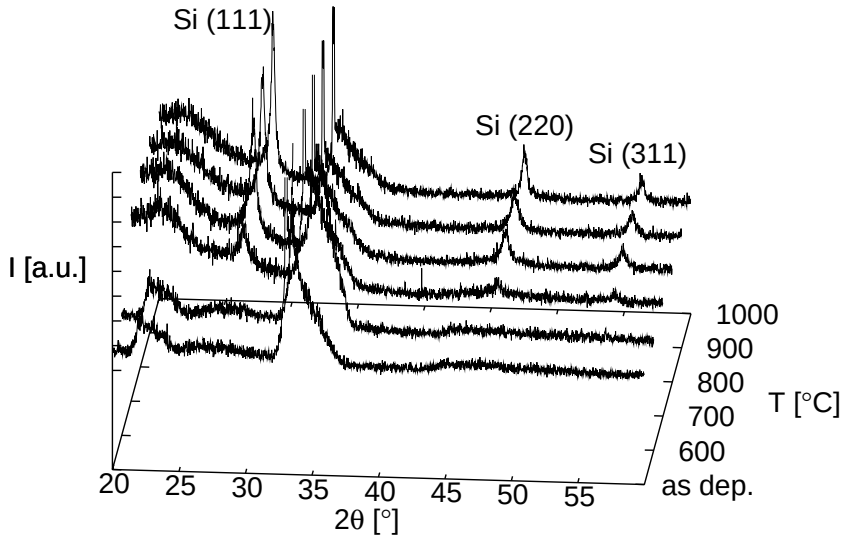

Figure 7.2: XRD measurement of PECVD a-Si:H layers after oven anneal.

Table 7.1: FWHM from the (111) and (220)-peaks in figure 7.2, and crystallite size calculated with Scherrer equation.

Temperature	(111)-peak		(220)-peak	
[°C]	FWHM [°]	t [nm]	FWHM [°]	t [nm]
700	0.7817	12.85	0.6630	19.74
800	0.5804	17.32	0.7127	18.33
900	0.5052	19.90	0.7759	16.83
1000	0.3771	26.68	0.5015	26.05

Rapid thermal annealing

Figures 7.3 a and b present extracts of XRD spectra measured on samples deposited by LPCVD and PECVD, respectively. The substrates are again (100)-oriented silicon with 3.0 μm of thermal oxide. The (as-deposited) film thickness is 380 nm. These thinner films are less prone to cracks or delamination than the films discussed in the previous paragraph.
The presented extracts focus on the (111)-peak, because it is the only detectable one in all RTP annealed samples.
As-deposited samples, both for the PECVD and also for LPCVD, again do not show any crystalline peaks.
In the case of LPCVD samples, the (111)-peak becomes detectable for anneal temperatures of 750 °C and above, whereas the anneal at 700 °C does not have any significant impact on the XRD-spectrum.
However, for PECVD samples the (111)-peak only appears at a higher temperatures compared to LPCVD samples. All measured spectra up to 850 °C anneal temperature do not show any significant change, but in the case of the 900 °C annealed sample, again the (111)-peak is detected.

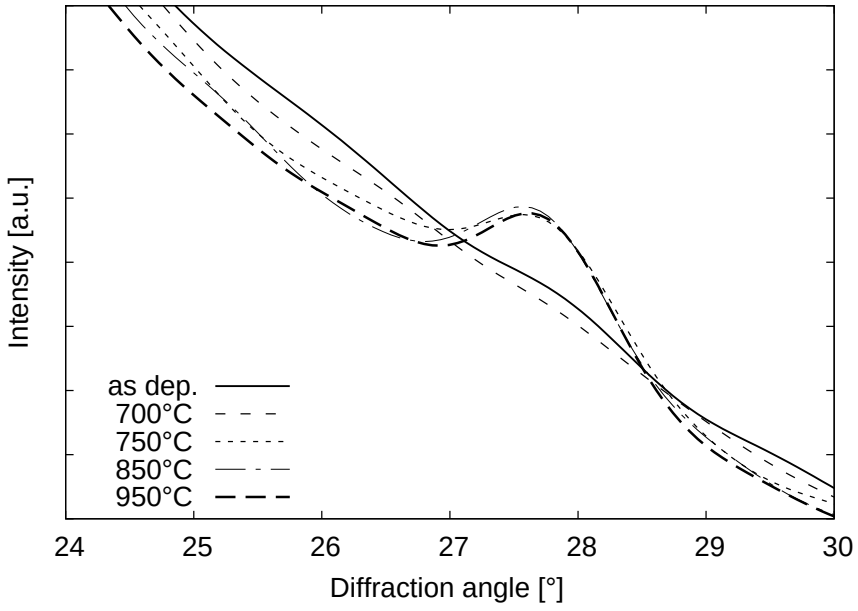

(a)

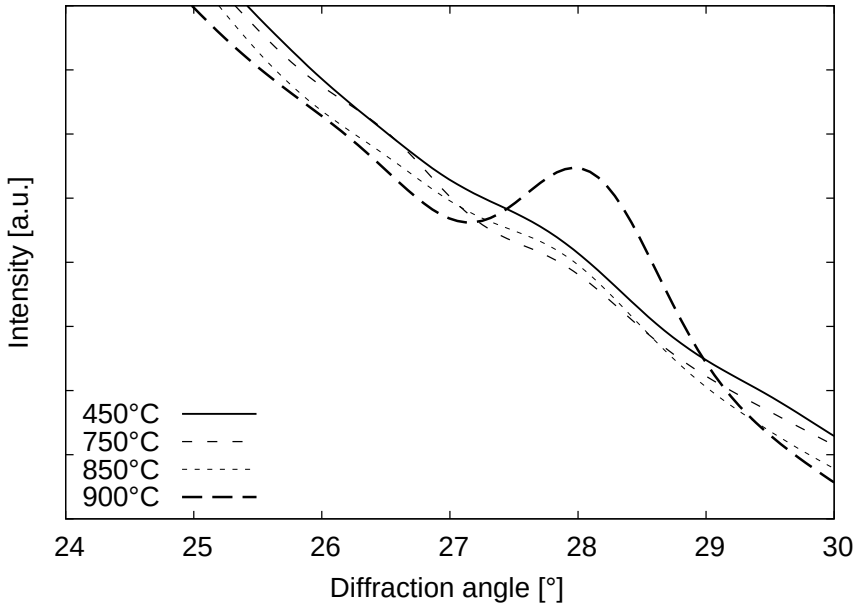

(b)

Figure 7.3: XRD measurement of LPCVD (a) and PECVD (b) a-Si layers after rapid thermal anneal.

7.2.4 Effect on Raman spectra

The film morphology is further investigated by Raman spectroscopy (see chapter 5.4) for all RTA processed samples.
In figure 7.4, Raman spectra for PECVD grown samples are presented.
The first order Raman peak of c-Si at $521\,\mathrm{cm}^{-1}$ is of dominant intensity. Here, it originates mainly from the c-Si substrate, which is present in all samples.
Next to this peak, a broad shoulder exists at around $480\,\mathrm{cm}^{-1}$, which is typical for amorphous Si and attributed to the transverse optical (TO) phonons (see chapter 2.4). Further broad peaks at around 180, 300 and $390\,\mathrm{cm}^{-1}$ can be assigned to the transverse acoustic (TA), longitudinal acoustic (LA) and optic (LO) modes, respectively.
The Raman spectra of as-grown PECVD and LPCVD films are similar (compare figures 7.4 and 7.5), but apparent differences are a lower and broader band at around $480\,\mathrm{cm}^{-1}$ for PECVD samples, and the TA-peak more clearly dropping off at around $210\,\mathrm{cm}^{-1}$ for LPCVD samples.
The effect of RTA on PECVD films is a continuous decrease of intensity around $210\,\mathrm{cm}^{-1}$ at temperatures from 500 °C to 800 °C. This is believed to be caused by hydrogen, because the effect is absent in LPCVD films.
The sample annealed at 900 °C shows a drastic change of the Raman spectrum. All phonon bands decrease significantly in intensity and width, and only the first order c-Si peak increases in intensity, so that the overall spectrum is more like c-Si. The measurement of this transition is well in line with the results obtained from XRD.
The actual phonon spectra of amorphous and crystalline silicon are not much different. The phonon density of states is broadened due to the disorder in bond strength and in the case of a-Si:H hydrogen bonding introduces additional phonon modes. However, the Raman spectra are very dissimilar, because of relaxed selection rules due to the absence of phonon wavevector conservation. This allows all phonons to contribute to the measured Raman spectrum, which then represents the shape of the phonon density of states in a-Si, but for c-Si gives a single peak at the upper point of the TO-band.
In LPCVD samples, the effect of RTP annealing on the Raman spectra becomes significant at temperatures above 750 °C, which also corresponds to the XRD results. The TA and TO-peaks are reduced in intensity, whereas the LA-peak is less broad and gains in intensity (see figure 7.5). Also, the first order c-Si peak increases, and also in this case the spectrum gets more c-Si like.

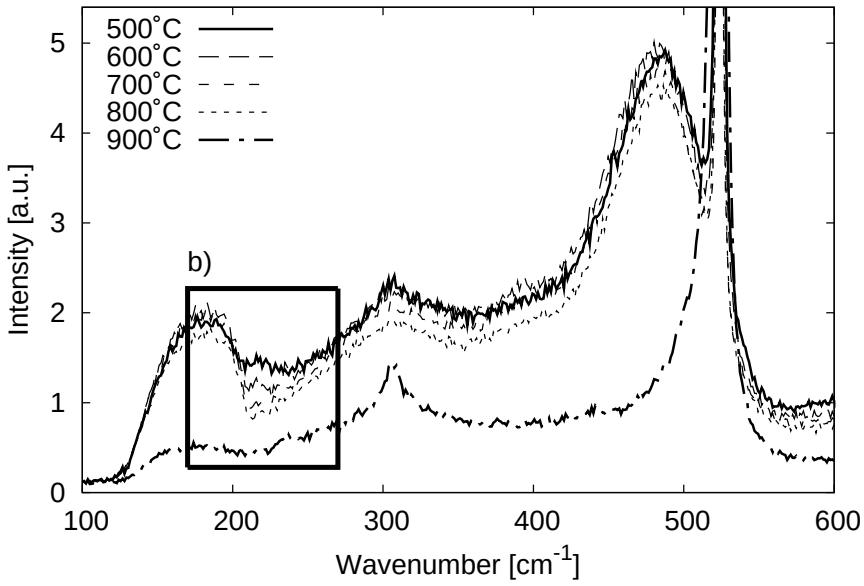

(a)

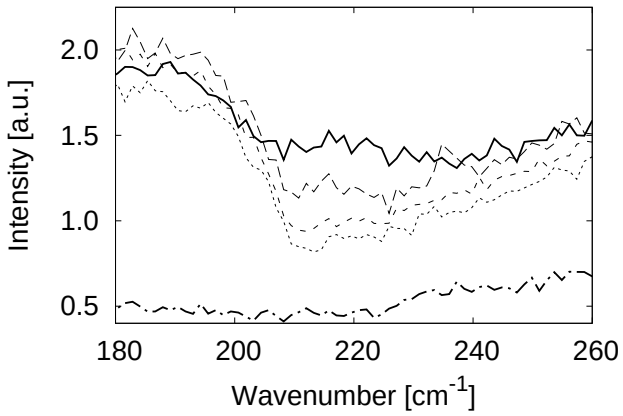

(b)

Figure 7.4: Overview (a) and section (b) of Raman spectra measured on PECVD deposited a-Si:H after RTA anneal.

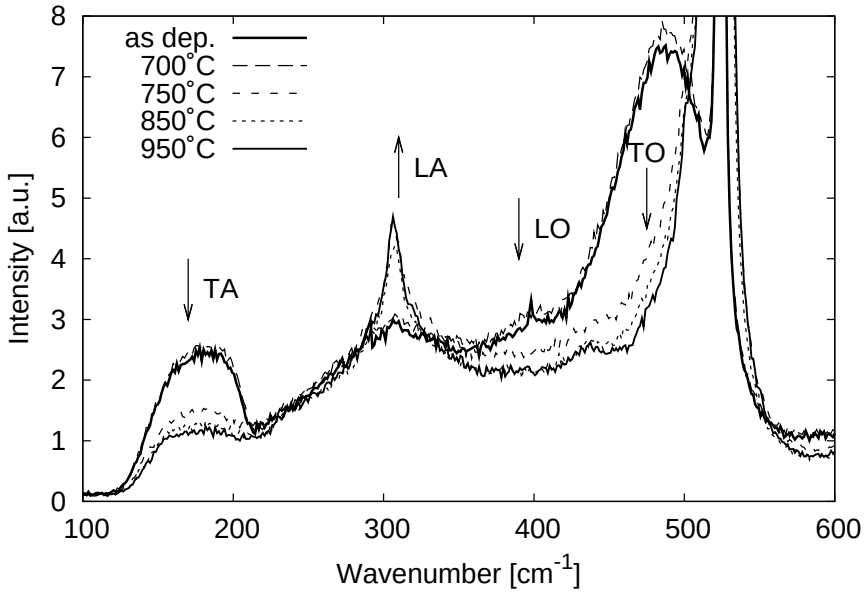

Figure 7.5: Raman spectra of LPCVD deposited a-Si:H after RTA anneal.

7.2.5 Impact on optical properties

Of essential importance for the intended application are the optical properties, namely refractive index and material absorption. These are studied in order to determine the effect of different annealing temperatures, which is is measured on RTA processed samples deposited by both PECVD and LPCVD.
The reactions of the amorphous matrix on thermal treatments, namely breaking and rearrangement of weak bonds, hydrogen outdiffusion and crystallization, have impact on both electronic and optical properties.
The refractive index of PECVD and LPCVD films is measured by ellipsometry. To reduce measurement error, the sample film thickness is chosen to be 110 nm. This represents approximately a quarter wavelength for $\lambda = 1534\,\text{nm}$ and $n = 3.5$ (see chapter 5.1).

PECVD films

The effect of RTP annealing at different temperatures on the measured refractive index and layer thickness is shown in figure 7.6.
The values measured at 1303 nm and 1534 nm wavelength are corresponding. The refractive index is not changed significantly for temperatures below 550 °C.
At higher temperatures, a significant increase of the refractive index of $\Delta n \approx 0.24$ is observed. A refractive index maximum is reached for a temperature of 800 °C. Even higher temperatures result in a refractive index, which in the case of the 900 °C annealed sample is nearly as-deposited. The measured film thickness decreases almost continuously with temperature.
When compared with the results from Raman spectroscopy (see chapter 7.2.4), XRD (see chapter 7.2.3) and FTIR (see chapter 7.2.2), the two refractive index changes agree with changes observed in the corresponding data.
Therefore, the initial increase of refractive index is attributed to the breaking of weak Si-H bonds. The involved loss of hydrogen increases defect density, which then results in an increase of both real and imaginary part of the refractive index.
The index reduction at even higher temperatures is attributed to the onset of crystallization, because of structural changes observed in XRD and Raman spectroscopy at corresponding temperatures. Crystallization reduces defect density due to a rearrangement of the silicon matrix.
To further investigate the suspected impact on material absorption, samples with multiple waveguides are fabricated. For details on waveguide design and fabrication see chapters 8.1 and 8.2, respectively.

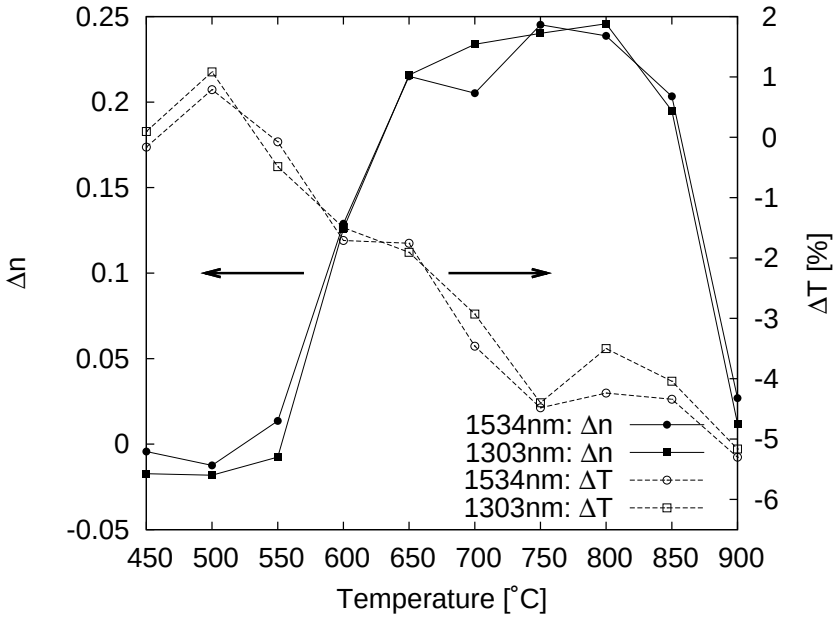

Figure 7.6: Changes of refractive index (Δn) and layer thickness (ΔT) caused by RTA postprocessing.

To facilitate the measurement of material absorption at a minimum of scattering and coupling losses, 4 μm-wide multi-mode waveguides are used.
By comparison of the transmitted intensity of waveguides before and after RTP annealing, the change in transmission loss is calculated. In order to reduce error from in- and outcoupling losses, multiple waveguides are measured to obtain a reliable mean value for each data-point in figure 7.7, and the double standard deviation is indicated by the error bars. The data shows an increase in transmission loss at temperatures, which correspond to the measured increase in (real) refractive index, as expected.
Waveguides annealed at temperatures above 650 °C are destroyed due to cracks an delamination.

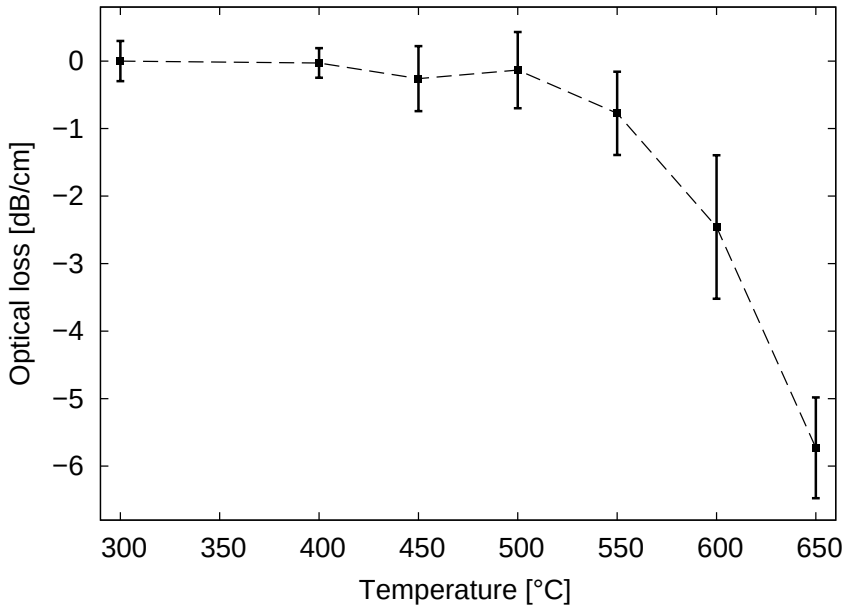

Figure 7.7: Total transmission losses caused by RTA postprocessing.

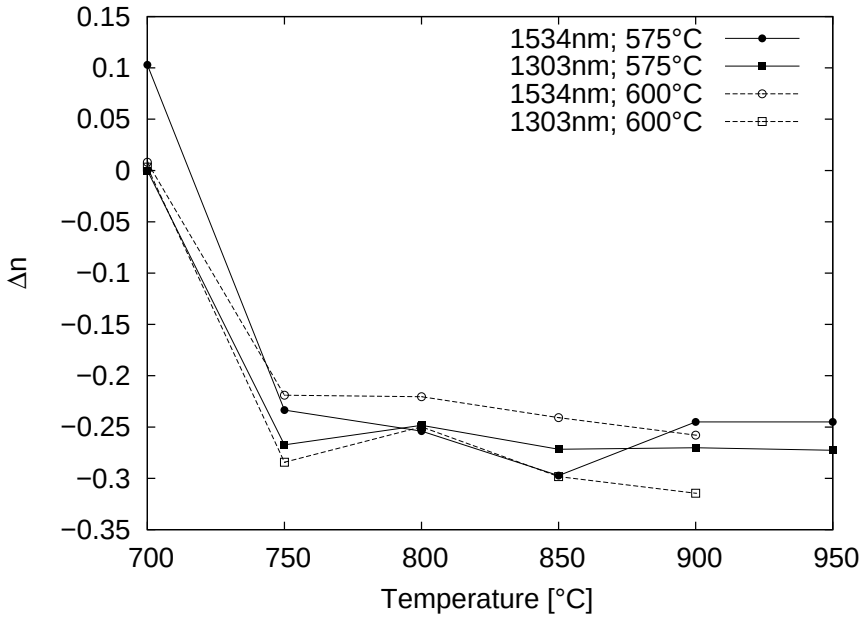

Figure 7.8: Changes by RTA in refractive index of LPCVD a-Si deposited at 575°C and 600°C.

LPCVD films

LPCVD samples are annealed at temperatures starting at 700 °C, i.e. well above deposition temperature. Again a decrease in refractive index is measured, which corresponds to the onset of crystallization detected in Raman as well as XRD measurements.

Though this refractive index decrease is expected to also indicate a decreasing absorption, attempts to measure propagation losses in optical waveguides made from LPCVD films failed. The propagation losses due to scattering, as well as material absorption is too high to obtain any measurable waveguides from both, the as-deposited as well as annealed samples.

Also, results from Liao et al. [125] show high losses (>20 dB/cm) in poly-Si waveguides, and high temperature anneal at 1100 °C in oxygen free ambient in combination with hydrogen plasma treatment are reported to reduce losses to a minimum of 9 dB/cm.

Chapter 8

Application in integrated optics

While the previous chapters are mainly focused on material properties and how these are influenced by deposition and post-treatment, this chapter describes the fields of application for amorphous silicon in integrated optics.
First, waveguide design and process flow for fabrication is briefly presented.
Then, the waveguides are characterized by various methods, such as cut-back or Fabry-Perot.
Novel fields of application are developed with the intention to utilize special features of amorphous silicon:
Three-dimensional taper structures are fabricated with shadow masks by the low-temperature, plasma-enhanced deposition process described in chapter 6.
A process for fabrication of horizontal slot waveguides filled with electrooptic polymers is demonstrated, which exploits the flexibility of the PECVD process to deposit a sequence of different materials in one step.
The feasibility of stacking waveguides in multiple layers above each other using planarization techniques is studied, and vertical coupling of stacked waveguides is simulated.
This potential of amorphous silicon enables back-end electronic-photonic integration. It would allow more flexibility in design, as active areas in the front-end can be separated from waveguides, filters and taper structures, which could also be integrated into the back-end of a electronic-photonic circuit.

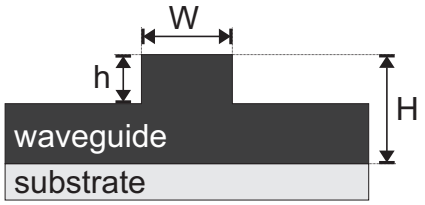

Figure 8.1: Denotation of characteristic waveguide dimensions (for strip waveguides: H = h).

8.1 Waveguide design

Three different waveguide designs are applied in this work for various experiments or applications. The designs are:

a) Multimode strip waveguides (MMSWG), which have a width of W = 4 μm and a height of H = 2.5 μm. (Please refer to Figure 8.1 for the denomination of dimensions.) The main advantage of this design is a relatively low influence of scattering on propagation losses due to a large cross section. Further advantages are relaxed demands on lithography process, due to the width of the waveguides. This also facilitates efficient butt or end-fire coupling.
Materials' influence on propagation losses can more easily be measured than with other waveguide designs.

b) Monomode rib waveguides (SMRWG), with a width of W = 1.1 μm, a total height of H = 1.3 μm and a rib height of h = 380 nm. The design obeys the monomode condition 3.7 on page 27.
Advantages of the design are a relaxed lithography specification and efficient coupling without taper structures compared to monomode strip waveguides.

c) Monomode strip waveguides (SMSWG, also termed "photonic wires"), which have a width of W = 0.5 μm and a height of H = 220 nm. This design presents a challenge for lithographic accuracy, as well as for all other fabrication processes. The possible influence of any roughness, either on the sidewalls, created by the etch process, or on horizontal interfaces, created by deposition processes, is huge. Efficient in- and outcoupling is challenging and requires special taper structures.
However, the monomode strip waveguide design allows for the lowest curvature losses, and hence highest integration densities can be achieved. This type of design is state of the art in silicon photonics.

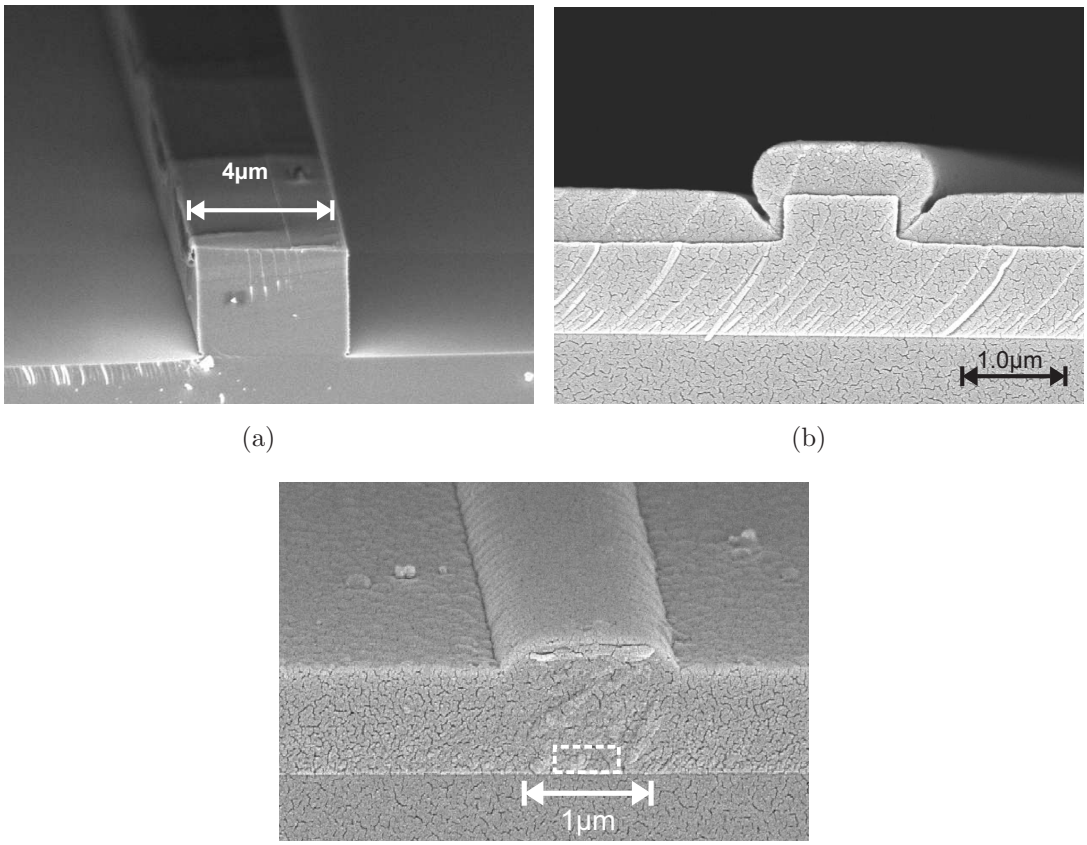

(a) (b)

(c)

Figure 8.2: SEM images of the cross sections of (a) multimode strip waveguides without cladding, (b) monomode rib waveguides with cladding and (c) single mode strip waveguide with taper.

SEM-images of waveguides' cross sections of all design options are presented in figure 8.1. The larger waveguides in images (a) and (b) have an additional cladding layer (see chapter 4.4), which serve mainly as scratch protection. The photonic wire (c) is covered with an a-Si:H three dimensional taper (see chapter 8.4.1).

8.2 Waveguide fabrication

All different waveguide designs presented can be fabricated using the same process flow.
As the single process steps are discussed in detail in chapter 4, here the overall process flow and process integration is presented.

Substrate

As a substrate for a-Si deposition in this work (as not stated otherwise), single-side polished Si-wafers with 100 mm diameter and (100)-orientation are used. The thickness of the wafers is specified as $500-550\,\mu$m, and they are n-type (phosphorus doped) with a resistance of $1-10\,\Omega$cm.
Other substrate materials such as polished glasses are thinkable, if PECVD at low temperature is used for the subsequent deposition steps.
Still, silicon wafers generally offer better stability, surface quality and compatibility with successive process steps, while costs are comparable or even lower than e.g. for polished glass wafers.

Thermal oxidation

On the substrate a layer of $3\,\mu$m SiO_2 is grown by wet thermal oxidation. Because the growth rate of oxide is limited by the diffusion of oxygen through the barrier of SiO_2, which has already been build up, the growth rate decreases over time.
Hence, the oxide thickness used here represents a maximum value, which can be obtained with a still reasonable process time of 1.5 days.
This layer with its refractive index of $n = 1.45$ acts as the lower waveguide interface. With a refractive index difference of $\Delta n \approx 2$ to the a-Si ($n \approx 3.5$) and an oxide thickness of $3\,\mu$m, any optical losses into the substrate can be neglected.

Photolithography

The photoresist masking for the subsequent etch step is then fabricated by contact photolithography (see chapter 4.2.4). A resolution of ≥ 500 nm is achieved with the present process.
To obtain smaller structure sizes in future in a cost-effective way, different available lithography techniques have been assessed (see chapter 4.2).

Etching

Then, the etch process described in chapter 4.3 is carried out.
To obtain the different waveguide designs, etch parameters have to be carefully adapted, because even though etch depth and process time are linear as a first approximation, secondary effects such as photoresist coverage and an initial breakthrough influence the etch result.
After etching, the remaining photoresist needs to be removed along with sidewall passivation, which is build up during the etch process. Here, a sequence of acetone, iso-propanol and DI-water ultrasonic-bath is used.
As organic solvents are known to be less effective for sidewall passivation removal, an additional oxygen plasma process is applied to enhance surface cleanliness prior to next deposition steps.

Cladding and facet preparation

A cladding layer is deposited mainly for scratch protection (see chapter 4.4).
The waveguides are then cleaved to permit light coupling. To reduce reflection at the cleaved coupling sites, facet polishing, cleaning and anti-reflective coating can be applied (see chapter 4.5).
The process flow from this step onwards varies for different experiments, as described in the following paragraphs.

Process flow overview

An overview of the fabrication process is shown in figure 8.3. In summary, the subsequent process steps are:

a) A SiO_2 layer is grown by wet thermal oxidation on the Si wafer.

b) The waveguiding layer is deposited, which can be either a-Si:H by PECVD or a-Si/poly-Si by LPCVD.

c) A waveguide structure is masked by photoresist.

d) The waveguide structure is dry etched.

e) The remaining photoresist is removed by organic solvents.

f) Finally, a cladding layer is deposited and the waveguides' facets are prepared.

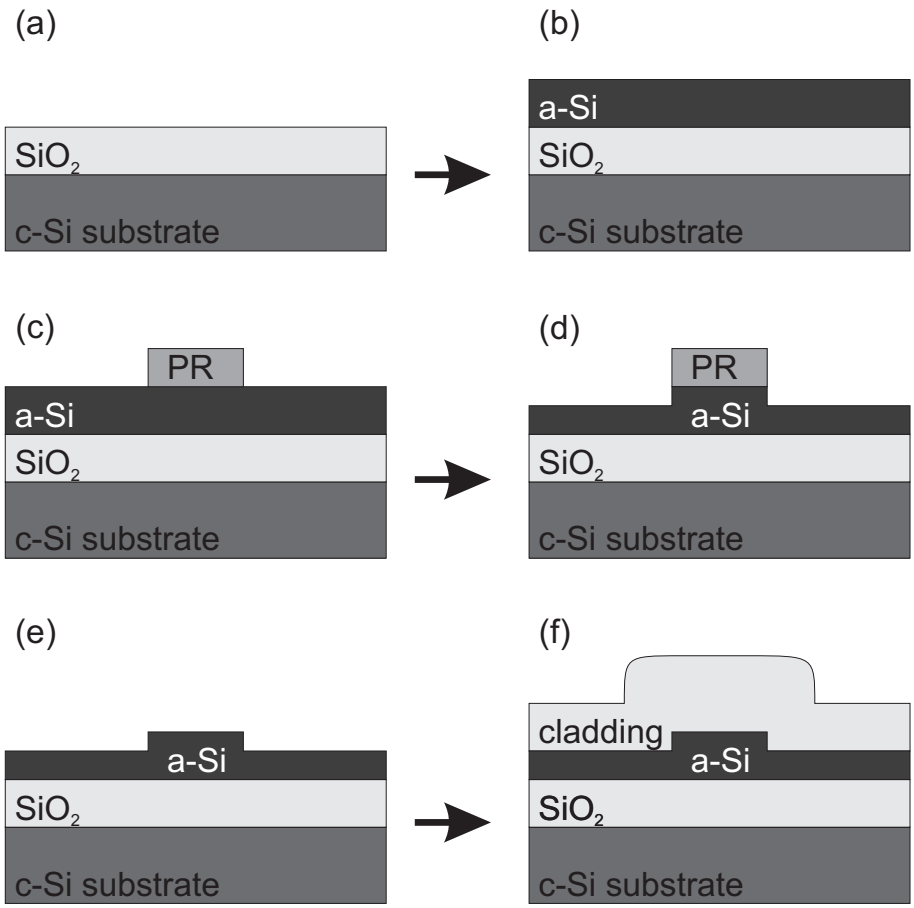

Figure 8.3: Process flow for waveguide fabrication.

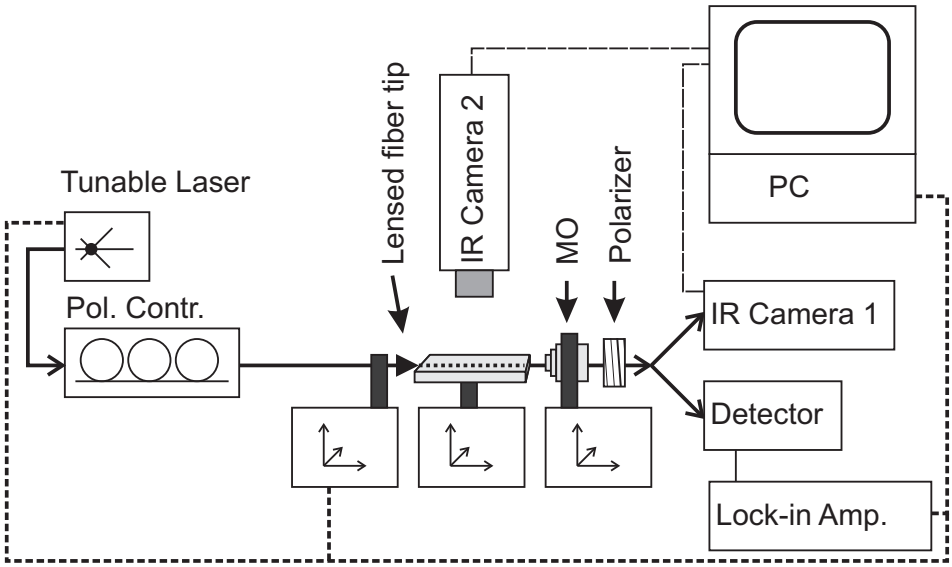

Figure 8.4: Measurement setup used for waveguide characterization.

8.3 Waveguide characterization

The waveguides are characterized primarily in order to obtain the losses and also to differentiate the contribution of different loss mechanisms (see chapter 3.2.2).
For instance, contributions to scattering loss originate mainly in surface roughness, which is created by the etch process.
Data on material losses may help to evaluate the deposition processes and post treatments.
The measurement setup used is presented in figure 8.4. The light source is a tunable laser module (*Agilent 81640A*) with a wavelength range of $1510 - 1640\,\text{nm}$. Via a manual polarization controller, light is coupled into the waveguide with a lensed fiber (obtained from *SOLITON GmbH*), which is chosen because its small spot-size of $1.7\,\mu\text{m}$ allowing reasonable coupling efficiencies. Due to the necessary alignment precision in nm-range, the lensed fiber end is mounted on an optical table with three axial Piezo-driven positioning. At the outcoupling facet of the tested device, light is collected by a microscope objective (20x, NA=0.35) and, after passing through a polarizer, is detected either by an IR camera or an InGaAs photodetector (*ThorLabs PDA10CF-EC*).
The camera is used to make alignment easier and is also applied for near-field measurements (see chapter 8.3.4). For cut-back or Fabry-Perot measurements, the camera is replaced by the photodetector.

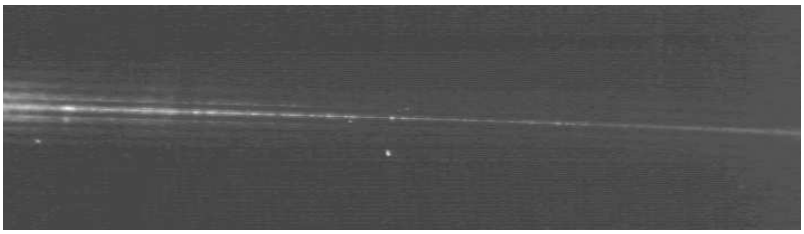

(a)

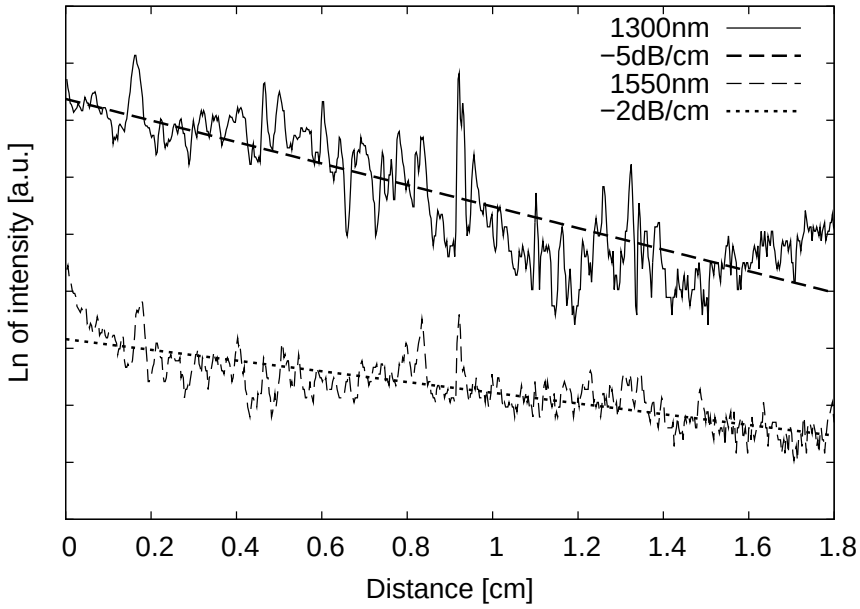

(b)

Figure 8.5: From an infrared camera image (a) the scattering light intensity (b) is extracted (SMRWG at 1300 nm and 1550 nm wavelength).

The detector signal was enhanced by phase sensitive detection with a lock-in amplifier (*EG&G5210*) for some measurements.
A second IR camera is mounted above the tested device. It helps to find a coarse alignment for coupling and allows scattering light measurements (see chapter 8.3.1). By application of a manual polarization controller in combination with an analyzing polarizer at the detector side, always the quasi-TE mode is selected.

8.3.1 Scattering light method

The scattering light method is based on the assumption that the intensity of scattering itself does not change along the propagation direction in a waveguide. Therefore, the intensity of scattered light only depends on the guided light intensity in the waveguide. The median intensity decrease of scattered light along the waveguide then represents the intensity decrease of light guided in the waveguide, and the propagation loss can be easily obtained by measuring the scattered intensity.
Usually, the fraction of light, which is scattered vertically up, is collected by a camera. The camera image is analyzed in order to extract the propagation loss.
However, this methods has two limitations:
Due to the limited dynamic range of the camera and the fact, that only a very small fraction of the guided light is actually detected, the method does in practice only apply for waveguides with losses dominated by scattering rather than material absorption.
Low-loss waveguides cannot be measured also because the assumption of a statistically equal distribution of scattering centers does not always hold.
From practical experience, only waveguides with propagation losses above 0.5 dB/cm dominated by scattering could be characterized.
An infrared camera image of a rib waveguide from PECVD a-Si:H with the dimensions W=1.1 μm, H=1.3 μm and h=380 nm is shown in figure 8.5a. The slope in the corresponding intensity plot (Fig. 8.5b) gives a value of the propagation loss of -2 dB at 1550 nm wavelength and -5 dB at a wavelength of 1300 nm. The higher loss at shorter wavelength can be attributed to both, an increase in material loss as well as scattering.
By comparison with measurements of larger multimode waveguides, where material losses dominate, an estimation for an upper limit of the material losses of 0.5 dB/cm at 1550 nm wavelength and 1.6 dB/cm at 1300 nm can be obtained [47].

8.3.2 Cut-back method

In the cut-back method, propagation loss is determined by measuring the light output intensities of waveguides with different length, based on the assumption of a constant incoupled intensity.
Practically, this can be done by implementation of appropriate test structures on a single chip, or also by literally cutting a single waveguide and doing repeated measurements.
The advantage compared to the scattered light method is a higher sensitivity, be-

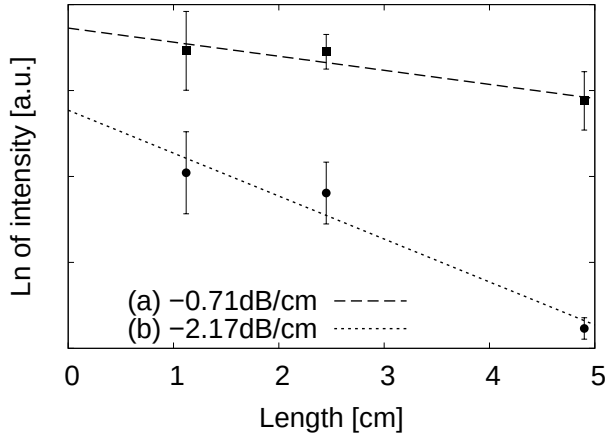

Figure 8.6: Total waveguide losses determined by cut-back measurement at 1550 nm wavelength from 4.0 μm wide multi-mode (a) and 1.1 μm wide mono-mode (b) waveguides.

cause almost the full intensity of light guided in the waveguide is measured, rather than a small fraction of light scattered vertically up.
On the other hand, the method is more complex and time-consuming. The assumption of a constant incoupling intensity cannot be met in practice. Due to misalignment or imperfect interfaces the incoupling intensities vary. To obtain reliable data, multiple measurements have to be made, so that a relevant mean value and variation for each measurement point can be calculated.
Figure 8.6 shows the result of cut-back measurements on monomode and multimode waveguides with the MMWG and SMRWG designs presented in chapter 8.1. Each data-point represents the average of 24 measurements.
The result is in good agreement with scattered light measurements.

8.3.3 Fabry - Perot method

The waveguide interfaces, namely the in- and outcoupling facets, reflect a certain fraction of light and a Fabry - Perot cavity is formed.
As in any other optical setup, such a parasitic cavity can result in an undesired frequency dependence of the transfer function. Therefore, care has to be taken in order to minimize reflections, for instance by application of anti-reflective coatings. On the other hand, this effect can be exploited to obtain additional information on the waveguides.

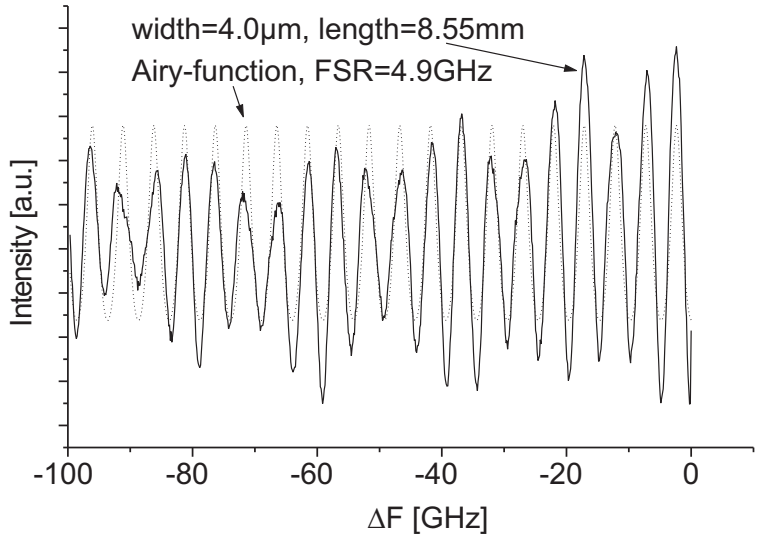

(a)

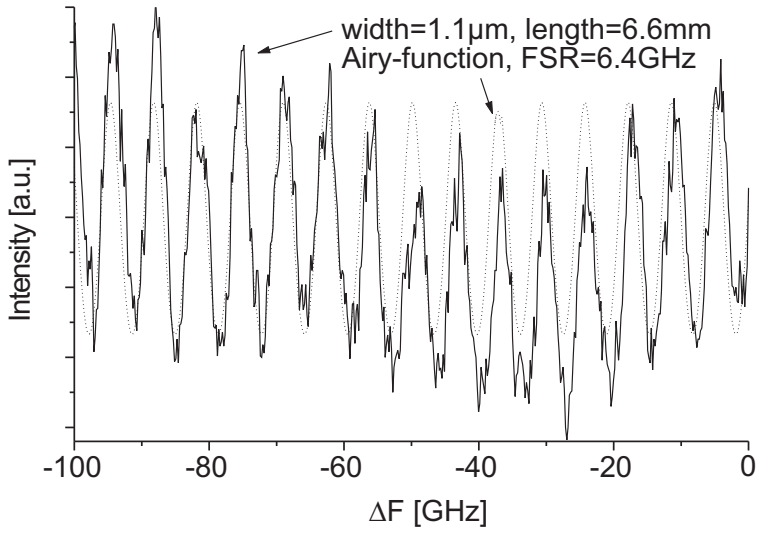

(b)

Figure 8.7: Fabry - Perot resonances within a multi-mode 4 μm wide (a) and a mono-mode 1.1 μm wide (b) waveguide.

If an attenuation within the cavity is considered, the spectral transmitted power can be expressed by expanding the Airy-function (see equation 3.9 on page 31):

$$\frac{\mathrm{I}_T}{\mathrm{I}_0} = \frac{(1-R)^2 \cdot \exp(-\alpha l)}{(1-R\exp(-\alpha l))^2 + 4R\exp(-\alpha l)\sin^2(\Delta\Phi/2)} \tag{8.1}$$

Where α is the attenuation coefficient and l is the cavity length.
The function shows a periodicity with minima and maxima at wavelength, where successive waves within the resonator interfere constructively or destructively.
The ratio between minima and maxima is obtained from the intensities at positions $\Delta\Phi_1 = 0$ and $\Delta\Phi_2 = \pi$.

$$\frac{\mathrm{I}_{max}}{\mathrm{I}_{min}} = \left(\frac{1+R\exp(-\alpha l)}{1-R\exp(-\alpha l)}\right)^2 \tag{8.2}$$

The ratio can be measured in order to determine the attenuation coefficient. In addition, from the free spectral range (see equation 3.10), a value for the refractive index can be obtained.
In practice, the Fabry-Perot method can only be applied for low-loss waveguides, if the interface reflectivity R is precisely known.
The measurement setup of figure 8.4 is used. A tunable laser is swept starting from 193.4 THz (equivalent to 1550 nm wavelength) for in total 100 GHz towards longer wavelength, while the transmitted intensity is detected.
The results for a MMWG and a SMRWG type of waveguides (see chapter 8.1) are shown in Figure 8.7. As the reflectivities are not known precisely due to imperfections in the facets, the attenuation could not reliably be determined for low-loss waveguides.
With the given length of the devices, the FSR corresponds to a group refractive index of n= 3.55 in both cases.
A beat frequency can be found in the spectral data of the multimode waveguide.
However, for waveguides with higher losses, such as the SMSWG type, calculated losses from Fabry-Perot measurements correspond with data obtained by the cut-back method (see table 8.1). This is attributed to the insignificance of an error in reflectivity, in the case where the attenuation in a resonator cycle is dominated by propagation loss, rather than reflection at end facets.

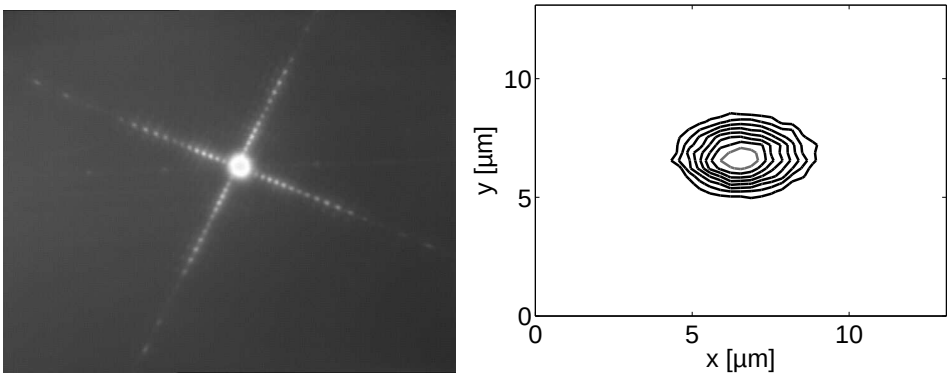

(a) (b)

Figure 8.8: Infrared camera image of outcoupled light from a waveguide end facet.

8.3.4 Near-field measurements

Near-field characterization can be applied for optical waveguides to extract information about the guided modes and therefore also the refractive index profile of the waveguide itself [126].
The outcoupled light from the waveguide facet is collected by a microscope objective and displayed by an IR camera. The resulting image of the outcoupling facet represents a superposition of intensity profiles of all guided modes in the waveguide. By analysis of its contour, one can decide whether the waveguide is mono- or multimode, or conclusions on the profile of the waveguide can be drawn, if one or the other information is known.
However, the method is usually applied for waveguides larger than a few microns. Results obtained here from small ($W < 2\,\mu m$), strongly guiding silicon waveguides with high numerical aperture are found to be not reliable enough to extract such information.
Figure 8.8(a) shows an IR camera image of the outcoupling facet of a waveguide.
Care has to be taken to match the dynamic range of the camera.
To increase effective resolution with the given camera, a microscope objective is used to depict the facet, and the beam path between objective and camera is extended to 1.5 meters.
A close-up image obtained in that way is presented in figure 8.8(b). Because of the single peak, which can be fitted to the expected intensity profile of the fundamental mode, monomode operation is suggested.
In this example, the waveguide is of the SMRWG type (see chapter 8.1) and has a

width of 1.1 μm.
The measurement is carried out at a wavelength of $\lambda = 1550$ nm.

8.3.5 Summary waveguide performance

A summary of results from propagation loss measurements is presented in Table 8.1. (Please refer to chapter 8.1 for the different waveguide types.)
The results for larger MMSWGs can be seen as an upper limit for material losses of a-Si:H deposited with the process presented in chapter 6.3.
The developed process flow also yields compact, low-loss (≈-2 dB/cm) rib waveguides.
However, if dimensions are further reduced and monomode strip waveguides are produced, limitations of the given processes are revealed by the high losses obtained.
The lithography process used is at its resolution limit. To get a better process capability, advanced lithography processes must be applied.
The sidewall roughness caused by the dry etch process used here, with its alternating etch and passivation steps, can still be improved, if a suitable single step process is developed.
Also, the surface roughness of the amorphous silicon layers might still be improved by further optimization of the deposition process. A possible approach could be hydrogen addition in combination with plasma power variation.
Furthermore, planarization methods such as CMP, could be applied.

Table 8.1: Propagation losses for different a-Si:H waveguide types at a wavelength of $\lambda = 1550$ nm.

Waveguide type	W; H; h [μm]	Loss [dB/cm]	Method
MMSWG	4; 2.5	0.7	cut-back
SMRWG	1.1; 1.3; 0.4	2.0	scattering light
	1.1; 1.3; 0.4	2.2	cut-back
	2.1; 2.0; 0.9	2.0	scattering light
	2.1; 2.0; 0.9	2.0	cut-back
SMSWG	2.0; 0.2	14.2	cut-back
	2.0; 0.2	14.5	Fabry-Perot
	0.5; 0.2	≥20	cut-back

8.4 Taper concepts

Light coupling into waveguides with small dimensions as presented in the previous chapter is a challenge. Differences in mode-field diameters (MFD) of a standard fiber (SMF-28, MFD=10 μm) and "photonic wires" are almost two orders of magnitude. As presented in chapter 3.2.4, a wide range of solutions to this problem have been developed.
In the following, the possibility to take advantage of low temperature deposition of highly transparent a-Si:H in order to create a novel taper concept is exploited.

8.4.1 Taper fabricated with shadow masks

The concept of this approach is to locally expand the profile of a photonic wire in width, as well as in height by an additional process step, where amorphous Si is deposited by PECVD [60].
For an efficient coupling, a number of constraints have to be considered.
The expanded profile should still represent a monomode waveguide, because higher order modes with off-centered intensity peaks could further decrease coupling efficiency.
A steady transition in both height and width of the waveguide over a sufficiently long tapered area has to be created. All interfaces must have a low roughness.

Fabrication method

To create a smooth transition of profiles, a shadow mask technique is chosen. Other approaches, by etching with gray-scale masks and/or isotropic etch processes, tend to generate rough surfaces and are difficult to control, because a number of subsequent steps can potentially influence the local etch rate.
For shadow masks usually sacrificial layers on the wafer are applied. Here, the mask material has to withstand a process temperature of 300 °C during a-Si:H deposition. This constraint excludes photoresists and other polymers, which are commonly used, because they can easily be spin-coated and are readily structured by lithography.
To influence the deposition profile over a length in the range of mm, the mask has to be relatively thick, which is difficult to achieve by deposited layers. Therefore, a hard mask made from a double-side polished (DSP) Si wafer is chosen. The DSP wafer with a thickness of 500 μm and (100)-orientation is covered by a SiN hard mask deposited by LPCVD. Structures are then etched through the wafer by hot KOH. The preferential etching of KOH along the (111)-planes of the silicon results

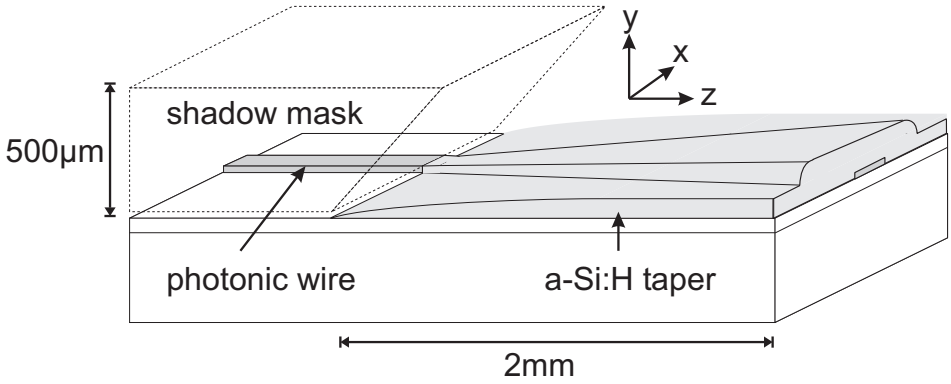

Figure 8.9: Schematic representation of the taper concept.

in slanted sidewalls at an angle of 54.7°. After mask removal the wafer is ready to be used as a shadow mask.
Prior to PECVD deposition, the mask is placed on a wafer, which is readily furnished with monomode strip waveguides fabricated by the process flow presented in chapter 8.2. For proof of concept, the alignment was done manually. To apply the method for complex integrated devices, a bond aligner could be used instead.
During a-Si:H deposition the 54.7° overhang partially shadows the waveguide and creates a 3D-taper. The taper concept is schematically presented in the drawing in Fig. 8.9.
After deposition, the mask is detached and the waveguides can then be prepared for end-fire coupling by cleaving within the deposited areas, optionally followed by polishing and anti-reflective coating deposition to further improve coupling efficiency.

Simulation of deposition profiles

To check and verify whether the geometry of the mask finally results in a taper, which is adiabatic and monomode, the deposition profile of the taper is simulated using a line-of-sight model. This model has been successfully applied for modeling profiles of silicon-oxinitride deposited in trenches by PECVD in order to fabricate trench-bulge waveguides [40]. Calculated and grown a-Si:H profiles are also in good agreement.
The calculated profiles for deposition on top of a photonic wire are presented in Figure 8.10. In comparison to the actual profile obtained from a SEM image, deviations are apparent at the abrupt edges of the profile, if the thickness of deposited layer exceeds the dimensions of the start profile.
The resulting profiles all resemble those of rib waveguides. All profiles for different

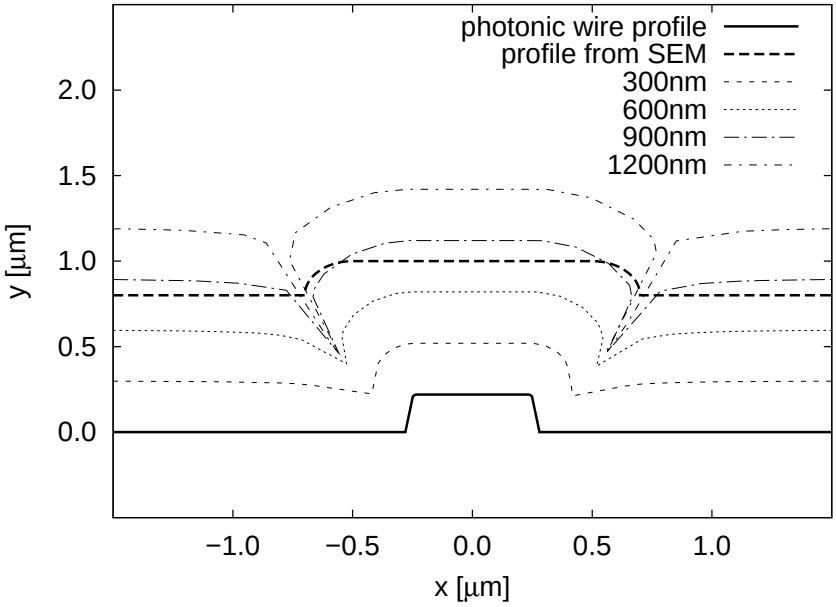

Figure 8.10: Simulated and measured deposition profiles perpendicular to the waveguide.

deposition thickness are analyzed for a wavelength of $\lambda = 1550\,\text{nm}$ using a full-vectorial mode-solver [8].
The results of this analysis show, that all profiles are monomode, and that with increasing layer thickness, the fundamental mode is guided ever less well in the horizontal dimension. Because of the decreasing relative step height, horizontal guidance is lost at a deposition thickness of 800 nm. Hence, to expand the modal field as much as possible without compromising vertical guidance, a deposition thickness of 800 nm is chosen.
Furthermore, calculations predict that this 3D-taper method is not applicable to larger rib waveguides with μm-dimensions, because with increasing taper thickness the total loss of horizontal guidance occurs already before any significant enlargement of the modal fields widths can be achieved.
The calculated deposition profiles along propagation direction (z) is presented in Figure 8.11. A steady increase of layer thickness is calculated for $z > 0$ along a distance of $\approx 2\,\text{mm}$. The point at $z = 0$ represents the end of the undercut of the shadow mask, which is assumed to be directly on the wafer surface at $y = 0$. A remaining thickness of 21% of the deposition thickness is calculated at this point.
To calculate coupling efficiencies, the modal fields for a bare photonic wire and for the

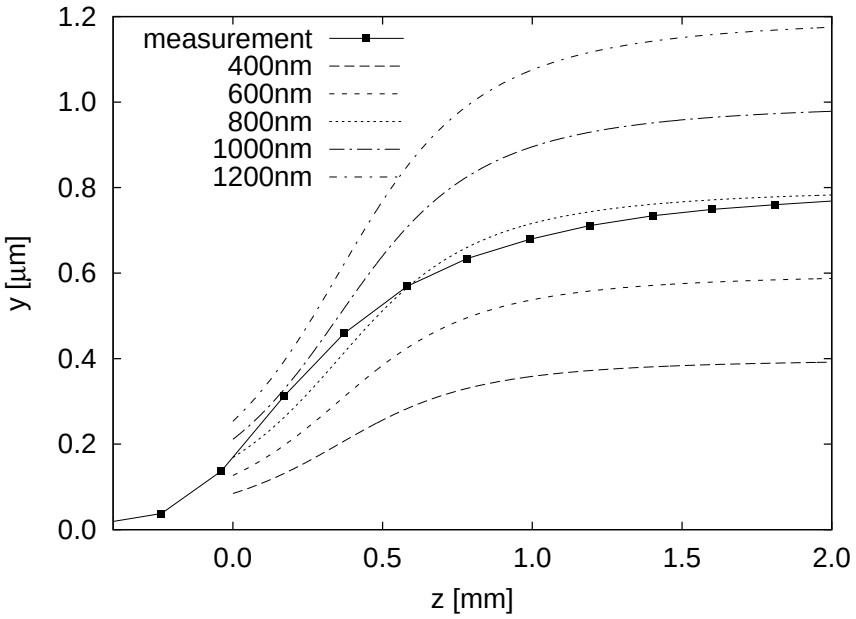

Figure 8.11: Simulated and measured deposition profiles along the propagation direction.

maximum taper width are calculated. Figure 8.12 shows the simulated transverse-magnetic-field profiles of the fundamental quasi-TE mode.
From the wider modal field one can already expect an increase in coupling efficiency. To obtain quantified estimations, the standard scalar overlap integral applied to the vertical magnetic-field component of the mode and a Gaussian input field is calculated. As input, a butt-coupled standard SMF-28 fiber with a mode-field diameter (MFD) of 10 μm, as well as a lensed fiber with an MFD of 1.7 μm are assumed.
Table 8.2 summarizes the $1/e$ field widths from figure 8.12 and lists the estimates for coupling efficiencies. Due to the taper coupling efficiencies improve by 11 and 5.7 dB for SMF-28 and lensed fibers, respectively.
Because the method of calculation gives reliable results only for weakly guiding waveguides, a more accurate simulation and optimization of the present high-index-contrast taper, especially of the input-coupling efficiency at the cleaved taper end, can be obtained by a more rigorous method such as finite-difference time-domain or bidirectional beam propagation.
Finally, the coupling loss due to reflection at the air-silicon interface is not taken into account here. This can be reduced by appropriate anti-reflection coatings.

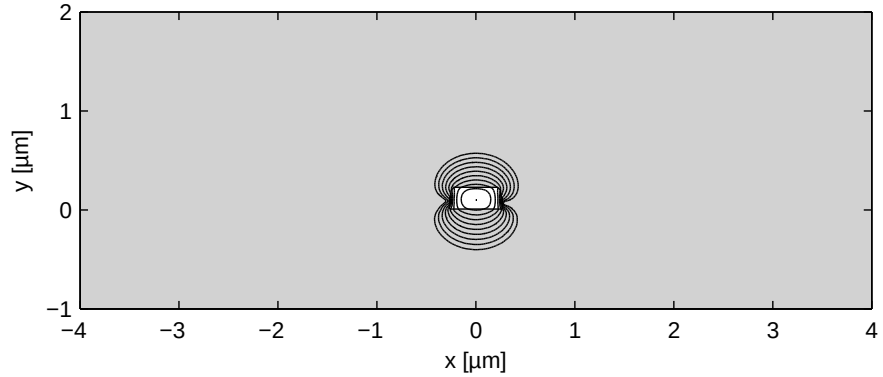

(a) non-tapered photonic wire profile

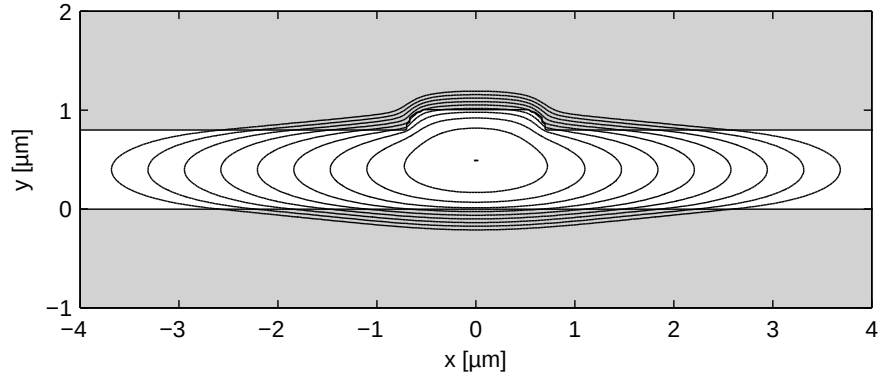

(b) tapered photonic wire profile

Figure 8.12: H-field of fundamental TE-mode in contour lines with 2 dB spacing calculated for the photonic wire.

Table 8.2: Simulated $1/e$ field widths $W_{x,y}$ and coupling efficiencies η.

	non-tapered	tapered
$W_x \times W_y$ (μm^2)	0.40×0.32	2.3×0.86
η (SMF28)	-22 dB	-11 dB
η (lensed fiber)	-7.2 dB	-1.5 dB

Experimental Results

The taper profile along z-direction is measured with an ellipsometer (*Horiba Jobin-Yvon PZ2000* equipped with micro-focus optics). The measured profile (see figure 8.11) is in good agreement with the simulations.
However, as in practice a gap between mask and substrate wafer occurs due to wafer bow, a steady decrease in thickness is measured also for $z \leq 0$.
In future process concepts, the distance between mask and substrate could be designed in a controlled way by implementation of a separation layer and bonding and release processes.
Using the measurement set-up described in chapter 8.3, light with a wavelength of $\lambda = 1550\,\text{nm}$ was coupled into the tapered and non-tapered photonic wires via a lensed fiber (obtained from *Soliton GmbH*, $1.7 - 2.0\,\mu\text{m}$ spot-size), with parameters as in the calculations. The intensity of the transmitted light was measured with the InGaAs-photodetector.
To obtain a reference, waveguides which were tapered and not tapered at the incoupling facet are compared. The length of the bare photonic wires was shorter by the length of the taper, in order to cancel out all loss mechanisms except for the propagation loss in the taper.
The total transmission-losses were reduced by $(3.0 \pm 0.8)\,\text{dB}$ due to the taper. The difference to the higher calculated value is believed to be explained by the propagation losses in the taper.
As explained in chapter 8.3.5, transmission losses for the waveguides increase significantly for the small dimensions used here.
Also, the unpolished end facets as well as the NA-mismatch at the outcoupling end-face cause additional losses.

8.5 Stacked waveguides

One potential of waveguides made from PECVD a-Si:H is the option to stack them on top of each other in multiple layers. Integration of passive photonic devices into the back-end of IC processes becomes feasible this way (see chapter 3.7).
Here, the feasibility of waveguide integration on top of each other is studied.
Directional coupling between stacked waveguides is simulated to determine, if critical parameters for the couplers can be met with standard IC process technology.

8.5.1 Vertical coupling

In directional couplers, light is exchanged periodically between waveguides, which are in close proximity to each other (see chapter 3.3.1). Because these are fabricated by thin film processes, these waveguides are usually made in one lithography step in one level next to each other.
If waveguides are to be positioned on top of each other, the most critical dimension of the coupler, which is the distance between waveguides, is determined by a number of processes, rather than one lithography and etch step.

8.5.2 Simulation

The two waveguides are regarded as one waveguiding structure and are analyzed with a full-vectorial mode solver [8]. Two orthogonal eigenmodes are obtained for each structure, and the power exchange length L_C of the coupler is calculated with expression 3.8 on page 29.
Monomode rib waveguides with different geometries (please refer to denomination in figure 8.1) and different distances to each other are simulated at a wavelength of λ=1550 nm. The refractive indices are set to n=3.5 for the waveguides, n=1.0 for the cladding and n=1.46 for substrate and separation layers.
Figure 8.13 gives one example of an eigenmode obtained for a vertical coupler.
For a common horizontal directional coupler, the power exchange length is calculated for different waveguide geometries and different distances (see figure 8.14).
As for the fabrication of vertical stacking of waveguides, the distance in the horizontal dimension is determined mainly by alignment accuracy of the second photo mask layer. From the slope of the graphs, one can estimate the tolerances which have to be met.
For weakly confining waveguides, the variation of the power exchange length with

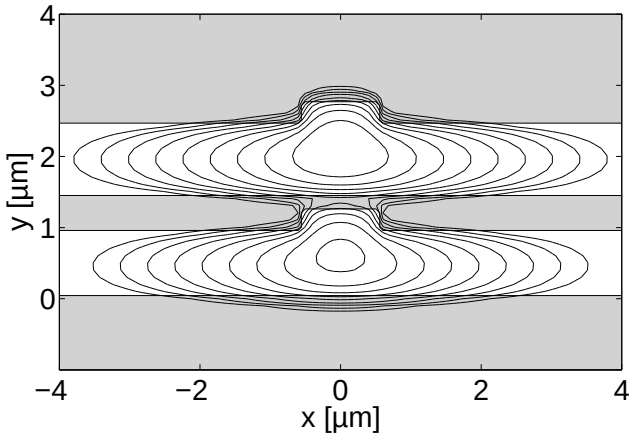

Figure 8.13: H-field of a orthogonal eigenmode in contour lines with 2 dB spacing calculated for a vertical coupler.

distance is lower. As a consequence, the alignment tolerance of the used mask alignment system also determines the possible waveguide design and finally the possible integration density.
The dependence of power exchange length on waveguide separation in the vertical dimension is shown in figure 8.15. The outline of the simulated structure is as presented in figure 8.13.
For the given waveguide design, the separation should be less than 300 nm, because the power exchange length significantly increases beyond that point.
At a separation distance of $100 - 300$ nm, the power exchange length is in the range of $0.1 - 2$ mm.
The necessary process steps for fabrication of stacked waveguides are deposition and structuring of the buried waveguide layer, deposition of the separation layer, planarization of the separation layer and polishing, in order to prepare the substrate for second waveguide layer deposition. Finally, the second waveguide is structured by lithography and etching and a cladding is deposited.
Hence, the vertical distance between the waveguides is determined by the deposition process of the separation layer and the subsequent planarization step. Specifications resulting from the change in power exchange length can be met by the tolerances of available back-end processes, namely PECVD and chemical mechanical polishing (CMP).

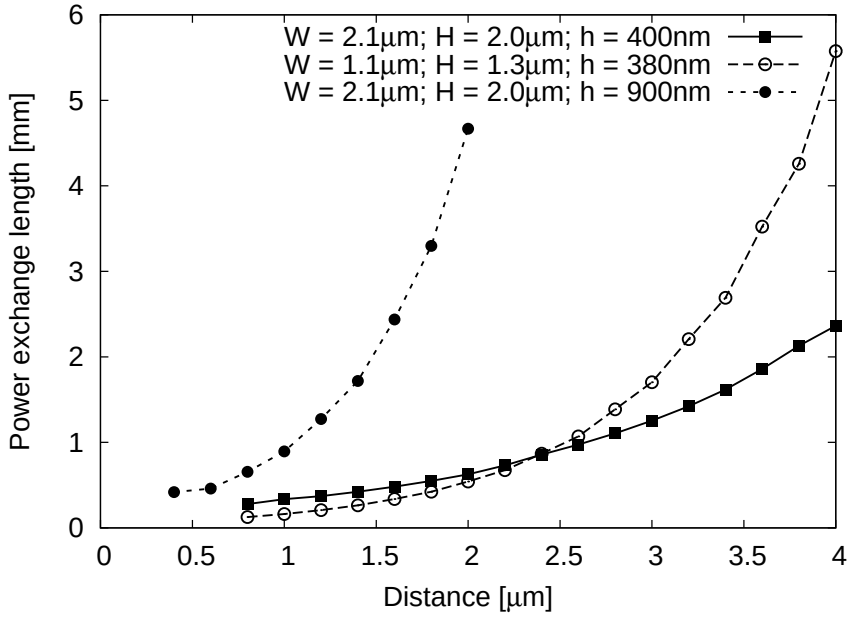

Figure 8.14: Dependence of power exchange length on distance between waveguides for horizontal coupler.

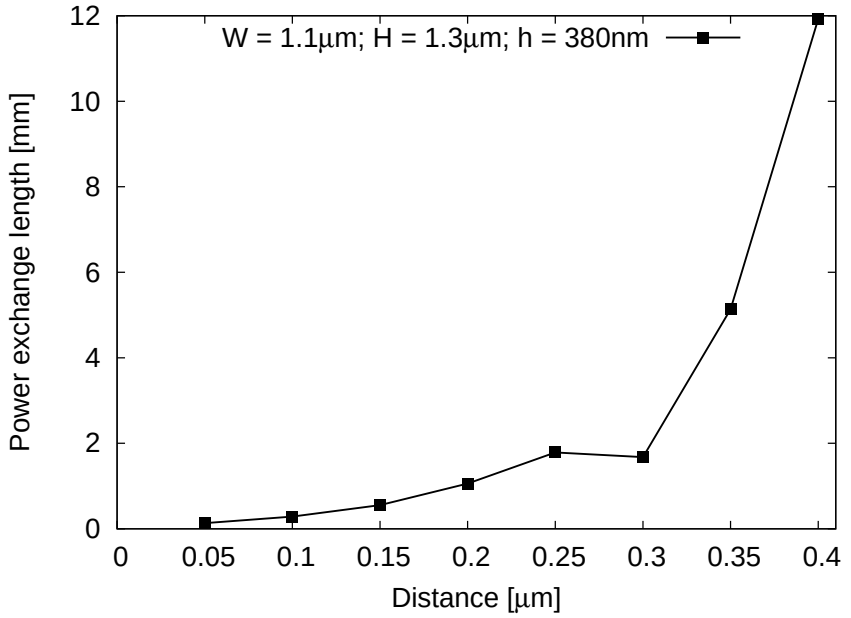

Figure 8.15: Dependence of power exchange length on distance between waveguides for vertical coupler.

8.5.3 Fabrication

Stacked waveguides have been fabricated using the following process flow:

1. Deposition and structuring of the buried waveguide layer
   as described in chapter 8.2.

2. Deposition of a separation layer.
   Silicon oxide is deposited by PECVD (see table 8.3).

3. Planarization of the separation layer by CMP.
   The samples were processed at the Institute for Microtechnology,
   Leibniz University Hannover.

4. Deposition and structuring of the top waveguide layer
   as described in chapter 8.2.

5. Deposition of a cladding layer as described in chapter 4.4.

The layer stack is analyzed by SEM. Figure 8.16 shows images of the profile of the complete wafer stack as well as a buried waveguide.
To enhance the contrast between layers, the samples were dipped in buffered oxide etch (BOE) and sputtered with a thin gold film prior to SEM imaging.
The overall planarization is successful, as the top interface of the separation layer is depicted as a straight line above the buried waveguide.
However, in AFM scans performed on the cladding layer (see figure 8.17), the buried waveguides show as slots at the side of the waveguides. This originates from an insufficient step coverage of the separation layer deposition process.
The scan shows a 1.1 μm wide waveguide in the top layer running from left to right and crossing a 4 μm wide waveguide in the buried layer running from top to bottom. As expected due to the given step coverage of the cladding layer, the top waveguide has indentations on its flanks. Also giving an indicating to an insufficient step coverage, voids appear at the sides of the buried waveguide after BOE preparation (see figure 8.16).
At the surface, scrub marks can be found in the AFM scan, which originate from the planarization process. To obtain low loss devices, a further optimization of the CMP process parameters, as well as the deposition process is necessary. The RMS roughness of the cladding surface is 8 nm.
Though generally the feasibility of stacked waveguide fabrication is demonstrated, these experiments did not yield operational waveguides and directional couplers, because of high scattering losses caused by the above mentioned imperfections.

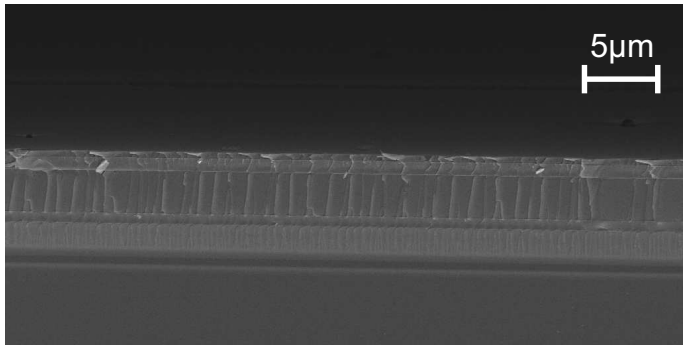

(a)

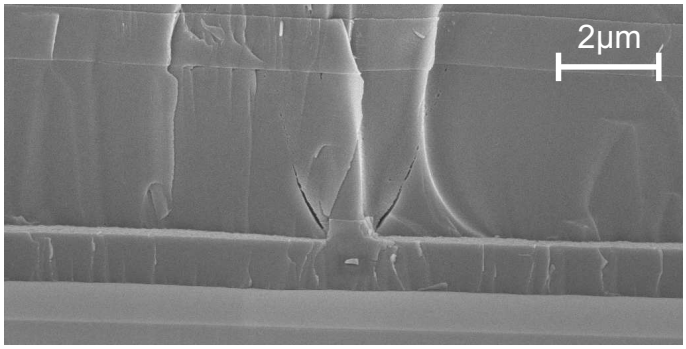

(b)

Figure 8.16: Cleaved edge of a waveguide stack (SEM image). (a) Overview of the layer stack, (b) close-up on a buried waveguide.

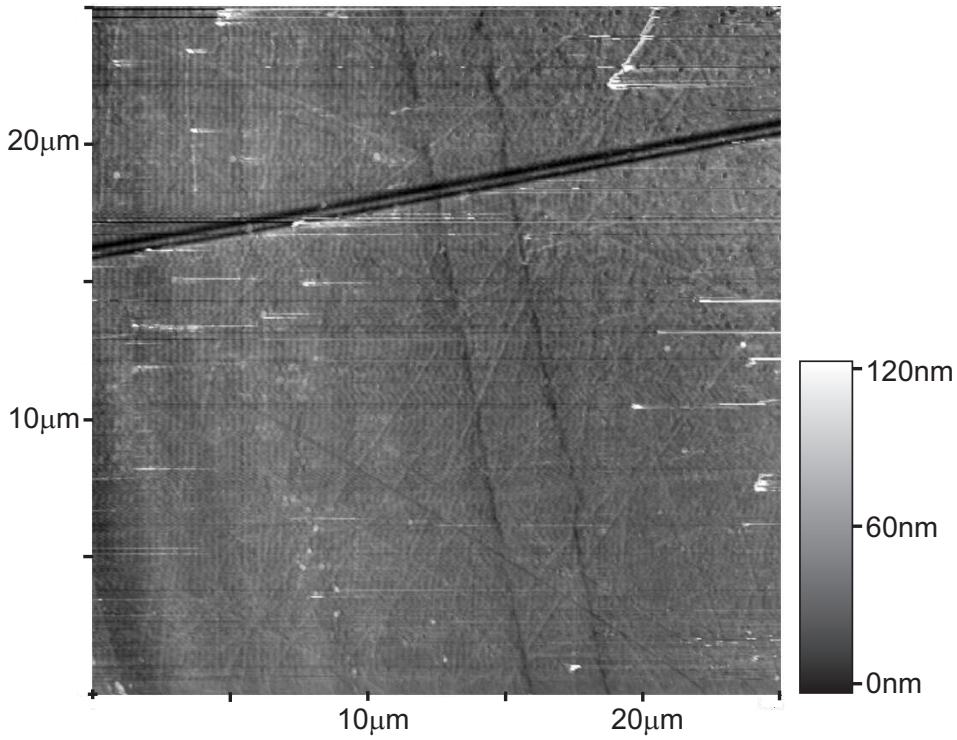

Figure 8.17: AFM scan of the top cladding layer on a stacked waveguide.

8.6 Slotted waveguides

Slotted waveguides consist of one or more low-index regions embedded in a high-index waveguide. A slotted waveguide can be designed in a way, that the optical field is enhanced in the low index regions due to the field discontinuities at the interfaces to the high index material [127].
In combination with hybrid material approaches, such as the application of electro-optical polymers, this effect can be utilized to enhance non-linear effects and to create modulators or detectors [50].
Completely etched horizontal slot waveguides have been characterized as waveguides and ring resonators by Sun et al. [128].
In order to create field enhancement, the low index regions need to be small ($\leq$ 100 nm). To fabricate such small-scale structures in the c-Si layer of SOI wafers, a vertical approach is usually applied, which requires high-resolution electron beam lithography and dry etching.
The additional interfaces necessary for field enhancement have significant impact on scattering loss due to their given roughness.
Here, a method to fabricate horizontally slotted waveguides with 100 nm low index regions based on deposition of a-Si:H is developed, which does not require high-resolution lithography and etch processes.
The PECVD deposition system described in chapter 4.1.2 can be used not only for the deposition of a-Si:H, but also for silicon-oxinitrides (SiO_xN_y). Adjusting the composition of the precursor gas by setting the flows for SiH_4, N_2O, N_2 and Ar, allows to create a wide range of compositions resulting in different refractive indices in the range between a-Si:H (n = 3.5) and oxide rich SiON (n $\geq$ 1.48).
As diffusion can be neglected at the relatively low process temperature, almost any layer sequence can be deposited in a single vacuum step.
To meet the specifications for a thin low index layer of a slotted waveguide, a process with parameters presented in table 8.3 is developed. It produces an SiON layer with a refractive index of n = 1.48, which is as low as possible with the given set-up. The low refractive index indicates a stoichiometry close to pure SiO_2, which is chosen in order to achieve a high selectivity when removing the layer in a subsequent wet-etch step.
Because of the low RF-power and low silane concentration, the deposition rate is relatively low, which is necessary to achieve the targeted film thickness of 100 nm in a controlled way.
In a sequence of a-Si:H deposition (see chapter 6.3) and SiON deposition, a layer

Table 8.3: Deposition parameters for silicon oxide.

Process parameter	PECVD
Temperature	300 °C
RF power, frequency	75 W, 380 kHz
SiH_4 flow	8 sccm
N_2O flow	500 sccm
Pressure	66.7 Pa (= 500 mTorr)

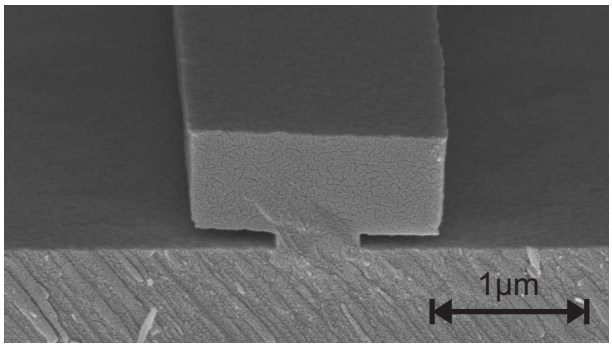

(a)

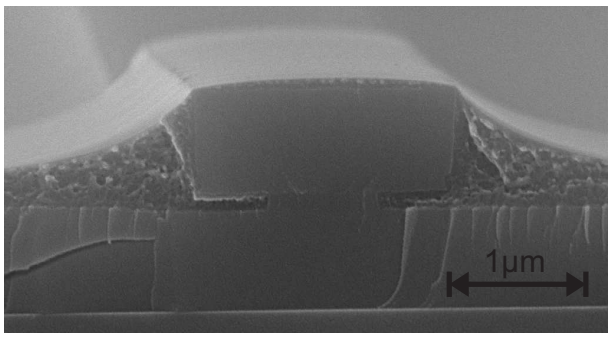

(b)

Figure 8.18: SEM images of the cross sections of a slotted waveguide (a) before and (b) after deposition of electrooptic polymer.

Table 8.4: Temperature sequence for electrooptic polymer vacuum oven bake.

Step No.	1	2	3	4	5
Temperature [°C]	94	134	170	190	slow ramp down
Time [h]	22	8	22	2	

stack of 750 nm a-Si:H, 100 nm SiON and 750 nm a-Si:H is deposited.
The top a-Si:H layer is then structured by lithography and dry etching.
The etch process based on SF_6 gas (see chapter 4.3) is stopped SiON, where the layer proved to be a sufficient etch stop.
After stripping the photoresist, the SiON layer is removed by a BOE wet-chemical etch. The selective and isotropic etch allows to remove the SiON in between the a-Si:H, as it can be seen in the SEM images of the profile in figure 8.18(a).
Care must be taken to leave a base of SiON, in order not to detach the top a-Si:H layer completely. At room temperature, the underetching U of SiON under the a-Si:H is found to follow roughly the expression
$U\,[\mathrm{nm}] \approx (t\,[\mathrm{s}] - 60\,\mathrm{s}) \cdot 2.9\,\mathrm{nm/s}$.

After SiON etch, the feasibility to fill the gaps with electrooptic polymer has been tested by the Institute of Optical and Electronic Materials, Hamburg University of Technology.
A polymer solution (PMMA/DR-1 dissolved in hexahydrophenol) is spin coated on the wafer.
Then, a sequence of heating steps in a vacuum oven with temperatures up to 190 °C and slow temperature ramp rates (see table 8.4) is used to remove the solvent and at the same time move the polymer into the gaps by capillary forces.
As shown in the SEM image in figure 8.18(b), the polymer is concentrated at the sidewalls and fills the gaps, whereas on open areas only a thin polymer layer remains.
Thus, the feasibility of fabricating polymer filled gaps using a process flow with sequential deposition of SiON and a-Si:H is demonstrated.

Chapter 9

Conclusions

The short range order of atoms in amorphous silicon results in semiconducting properties, with a band structure and a band gap energy of approximately 1.8 eV. However, high scattering of charge carriers due to the missing long range order of a crystal causes localized energetic states of charge carriers. Band tails, which consist of localized and extended states, rather than sharp band edges exist.
The rule of momentum conservation is relaxed due to scattering with impact on carrier generation and recombination. Raman spectra represent the full phonon spectra, rather than a single peak as in the case of crystalline silicon. The carrier mobility is much lower than in c-Si, and carrier lifetime remains relatively high.
Amorphous silicon can be doped with an efficiency sufficient for a number of applications. As the possibility of depositing large area substrates with the low temperature plasma process exists, the material is widely used for thin film photovoltaic cells or thin film transistor liquid crystal displays.
In this work, the potential of amorphous silicon for applications in silicon photonics is evaluated.

Amorphous hydrogenated silicon deposited by PECVD generally possesses a low defect density, because the majority of dangling bonds is saturated with hydrogen. The low defect density results in a low material absorption at an infrared wavelength range, which matches the relevant windows for optical communication. Its refractive index is in the same range as c-Si.
Refractive index, as well as further material properties are strongly influenced by the deposition parameters. For instance, film stress is mainly influenced by precursor gas composition. Hydrogen contents depends on a number of parameters, but primarily on deposition temperature.

However, the thermal stability of a-Si:H is not comparable to c-Si or poly-Si. Two main effects are found in thermal post-treatment of a-Si:H films:
At temperatures above 400 °C, Si-H bonds break and hydrogen is finally driven out of the material. As a consequence, the defect density increases and causes the absorption and (real) refractive index to increase as well.
At even higher anneal temperatures, a lowering of the refractive index is observed, which can be attributed to structural changes in the Si matrix, i.e. the onset of crystallization.
Amorphous or poly-crystalline films deposited by LPCVD show an initially high refractive index and absorption. Also, a reduction of refractive index is observed for high temperature annealing processes, which can, according to the corresponding XRD and Raman spectra, be attributed to crystallization.

Low-loss monomode waveguides are fabricated from a-Si:H deposited by PECVD [47]. Remaining optical propagation losses are found to be dominated by scattering at the etched waveguide sidewalls, as well as surface roughness caused by the deposition process.
The propagation losses in waveguides made from LPCVD films are found to be too high for practical application in passive devices in both as-deposited and annealed samples.

The availability of a material with a transparency and refractive index comparable to crystalline silicon, which is depositable at relatively low temperature, is further exploited for novel concepts of application.
Low-loss amorphous silicon is implemented in three dimensional tapers fabricated with shadow masks [60]. The application of Si wafers structured by KOH-etching as shadow masks facilitates the fabrication of mm-long three dimensional tapers by plasma deposition of highly transparent a-Si:H.
Also, the feasibility of vertical directional couplers is studied. Possible process tolerances are evaluated by simulations and stacked waveguide layers are produced by application of a planarization step.
Waveguides with 100 nm wide horizontal slots are created by deposition of a-Si:H and SiON layer stacks in a single process. Selective etching of the SiON film is used subsequently to create the 100 nm wide gap for field enhancement. The feasibility of filling such slots with electrooptic polymer is studied.

Outlook

Several applications of a-Si:H for passive devices have already been demonstrated, even ultra-compact photonic wires and ring resonators [107] are reported.
The back-end integration of waveguides into IC processes is being pursued [106], but still a functional back-end integrated electronic-photonic chip remains to be realized.
The flexibility of depositing a-Si:H on a wide range of substrates can possibly be exploited for new passive and also active devices.
Hybrid approaches to build optical modulators with electro-optical polymers, as they are already being realized based on SOI technology, could also be implemented in combination with a-Si:H, possibly gaining from the flexibility of the depositable material.
More research will be necessary to study the feasibility of an application of microcrystalline Si or also Si alloys for Raman amplification. The gain spectrum could be expanded, or other important material parameters, which are limiting the performance of Raman amplifiers or lasers, such as carrier lifetime, could be engineered.
Photonic crystals could be realized using a-Si:H in combination with low-index substrates.

Bibliography

[1] R. Soref, J. Schmidtchen, and K. Petermann, "Large single-mode rib waveguides in gesi-si and si-on-sio," *IEEE J. Quantum Electron.*, vol. 27, no. 8, pp. 1971–1974, Aug. 1991.

[2] A. Liu, R. Jones, L. Liao, D. Samara-Rubio, D. Rubin, O. Cohen, R. Nicolaescu, and M. Paniccia, "A high-speed silicon optical modulator based on a metal-oxide-semiconductor capacitor," *Nature*, vol. 427, pp. 615–618, 2004.

[3] O. Boyraz and B. Jalali, "Demonstration of a silicon raman laser," *Opt. Express*, vol. 12, no. 21, pp. 5269–5273, 2004.

[4] M. Haurylau, G. Chen, H. Chen, J. Zhang, N. A. Nelson, D. H. Albonesi, E. G. Friedman, and P. M. Fauchet, "On-chip optical interconnect roadmap: Challenges and critical directions," *IEEE J. Sel. Topics Quantum Electron.*, vol. 12, no. 6, pp. 1699–1705, 2006.

[5] R. Siebert and J. Mueller, "Infrared integrated optical evanescent field sensor for gas analysis: Part i: System design," *Sensors and Actuators A*, vol. 119, no. 1, pp. 138–149, 2005.

[6] ——, "Infrared integrated optical evanescent field sensor for gas analysis: Part ii. fabrication," *Sensors and Actuators A*, vol. 119, no. 2, pp. 584–592, 2005.

[7] R. Claps, V. Raghunathan, O. Boyraz, P. Koonath, D. Dimitropoulos, and B. Jalali, "Raman amplification and lasing in sige waveguides," *Opt. Express*, vol. 13, no. 7, pp. 2459–2466, 2005.

[8] M. Krause, *Efficient Raman Amplifiers and Lasers in Optical Fibers and Silicon Waveguides: New Concepts.* Cuvillier Verlag Göttingen, 2007.

[9] R. A. Street, *Hydrogenated Amorphous Silicon.* Cambridge University Press, 1991.

[10] K. Tanaka, E. Maruyama, T. Shimada, and H. Okamoto, *Amorphous Silicon*. John Wiley & Sons, 1999.

[11] W. Luft and Y. S. Tsuo, *Hydrogenated Amorphous Silicon Alloy Deposition Processes*. Marcel Dekker, 1993.

[12] J. S. Lannin, "Structural order and dynamics of amorphous si and ge," *J. Non-Cryst. Solids*, vol. 97-98, no. Part 1, pp. 39 – 46, 1987, amorphous and liquid semiconductors.

[13] W. E. Spear and P. G. L. Comber, "Substitutional doping of amorphous silicon," *Solid State Commun.*, vol. 17, pp. 1193–1196, 1975.

[14] H. Okamoto, H. Kida, and Y. Hamakawa, "Spectroscopic characterization of material and junction in amorphous silicon solar cells," *J. Non-Cryst. Solids*, vol. 77-78, pp. 1441–1449, 1985.

[15] S. Yamasaki, "Optical absorption edge of hydrogenated amorphous silicon studied by photoacoustic spectroscopy," *Phil. Mag. B*, vol. 56, pp. 79–97, 1987.

[16] W. B. Jackson and N. M. Amer, "Direct measurement of gap-state absorption in hydrogenated amorphous silicon by photothermal deflection spectroscopy," *Phys. Rev.*, vol. B25, p. 5559, 1982.

[17] W. B. Jackson, R. J. Nemanich, M. J. Thompson, and B. Wacker, "Schottky barriers on phosphorus-doped hydrogenated amorphous silicon: The effects of tunneling," *Phys. Rev. B*, vol. 33, no. 10, pp. 6936–6945, May 1986.

[18] G. H. Döhler, "Electron states in crystals with nipi-superstructure," *Phys. Stat. Sol. B*, vol. 52, p. 79, 1972.

[19] D. E. Carlson and C. W. Magee, "A sims analysis of deuterium diffusion in hydrogenated amorphous silicon," *Appl. Phys. Lett.*, vol. 33, no. 1, pp. 81–83, 1978.

[20] S. Matsuo, H. Nasu, C. Akamatsu, R. Hayashi, T. Imura, and Y. Osaka, "Dsc studies of glassy behavior in p-doped a-si:h," *Jap.J.Appl.Phys.*, vol. 27, pp. L132–133, 1988.

[21] D. L. Staebler and C. R. Wronski, "Reversible conductivity changes in discharge-produced amorphous si," *Appl. Phys. Lett.*, vol. 31, no. 4, pp. 292–294, 1977.

[22] R. Soref and J. Lorenzo, "Single-crystal silicon: a new material for 1.3 and 1.6 μm integrated-optical components," *Electron. Lett.*, vol. 21, no. 21, pp. 953–954, 10 1985.

[23] W. Bogaerts, V. Wiaux, D. Taillaert, S. Beckx, B. Luyssaert, P. Bienstman, and R. Baets, "Fabrication of photonic crystals in silicon-on-insulator using 248-nm deep uv lithography," *IEEE J. Sel. Topics Quantum Electron.*, vol. 8, no. 4, pp. 928–934, 2002.

[24] B. Jalali, V. Raghunathan, R. Shori, S. Fathpour, D. Dimitropoulos, and O. Stafsudd, "Prospects for silicon mid-ir raman lasers," *IEEE J. Sel. Topics Quantum Electron.*, vol. 12, no. 6, pp. 1618–1627, 2006.

[25] J. Liu, D. Pan, S. Jongthammanurak, D. Ahn, C. Hong, M. Beals, L. Kimerling, J. Michel, A. Pomerene, C. Hill, M. Jaso, K. Tu, Y. Chen, S. Patel, M. Rasras, A. White, and D. Gill, "Waveguide-integrated ge p-i-n photodetectors on soi platform," in *Group IV Photonics*, 2006, pp. 173–175.

[26] L. C. Kimerling, D. Ahn, A. B. Apsel, M. Beals, D. Carothers, Y.-K. Chen, T. Conway, D. M. Gill, M. Grove, C.-Y. Hong, M. Lipson, J. Liu, J. Michel, D. Pan, S. S. Patel, A. T. Pomerene, M. Rasras, D. K. Sparacin, K.-Y. Tu, A. E. White, and C. W. Wong, "Electronic-photonic integrated circuits on the cmos platform," in *Silicon Photonics*, J. A. Kubby and G. T. Reed, Eds., vol. 6125, no. 1. SPIE, 2006, p. 612502.

[27] Pavesi and Lockwood, Eds., *Silicon Photonics*. Springer, 2004.

[28] G. T. Reed and A. P. Knights, *Silicon Photonics*. Wiley, 2004.

[29] M. Lipson, "Guiding, modulating, and emitting light on silicon-challenges and opportunities," *J. Lightwave Technol.*, vol. 23, no. 12, pp. 4222–4238, 2005.

[30] B. Jalali and S. Fathpour, "Silicon photonics," *J. Lightwave Technol.*, vol. 24, no. 12, pp. 4600–4615, 2006.

[31] Z. Gaburro, P. Bettotti, N. Daldosso, M. Ghulinyan, D. Navarro-Urrios, M. melchiorri, F. Riboli, M. Saiani, F. Sbrana, and L. Pavesi, *Nanostructured Silicon for Photonics*. Trans Tech Publications, 2006.

[32] K. Wada, D. Ahn, D. Lim, J. Michel, and L. Kimerling, "Si microphotonics for optical interconnection," *Thin Solid Films*, vol. 508, pp. 418–421, 2006.

[33] L. Pavesi and G. Guillot, Eds., *Optical Interconnects*. Springer, 2006.

[34] R. Soref, "The past, present, and future of silicon photonics," *IEEE J. Sel. Topics Quantum Electron.*, vol. 12, no. 6, pp. 1678–1687, Nov.-dec. 2006.

[35] P. Ross, "Silicon photonics," *Spectrum, IEEE*, vol. 43, no. 1, pp. 54–54, Jan. 2006.

[36] G. T. Reed, Ed., *Silicon Photonics: The state of the Art*. John Wiley & Sons, Ltd, 2008.

[37] K. Worhoff, L. T. H. Hilderink, A. Driessen, and P. V. Lambeck, "Silicon oxynitride," *J. Electrochem. Soc.*, vol. 149, no. 8, pp. F85–F91, 2002.

[38] K.-J. Ebeling, *Integrated Optoelectronics*. Springer, 1993.

[39] C. Pollock and M. Lipson, *Integrated Photonics*. Kluwer, 2003.

[40] M. Krause, H. Renner, A. Harke, J. Muller, and E. Brinkmeyer, "Leakage loss in trench-bulge waveguides," *J. Lightwave Technol.*, vol. 23, no. 5, pp. 1890–1895, May 2005.

[41] R. Soref and J. Larenzo, "All-silicon active and passive guided-wave components for $\lambda = 1.3$ and 1.6 μm," *IEEE J. Quantum Electron.*, vol. 22, no. 6, pp. 873–879, Jun 1986.

[42] R. Soref and B. Bennett, "Electrooptical effects in silicon," *IEEE J. Quantum Electron.*, vol. 23, no. 1, pp. 123–129, Jan 1987.

[43] R. Claps, V. Raghunathan, D. Dimitropoulos, and B. Jalali, "Influence of nonlinear absorption on raman amplification in silicon waveguides," *Opt. Express*, vol. 12, pp. 2774–2780, 2004.

[44] F. P. Payne and J. P. R. Lacey, "A theoretical analysis of scattering loss from planar optical waveguides," *Optical and Quantum Electronics*, vol. 26, pp. 977–986, 1994.

[45] J. Schmidtchen, A. Splett, B. Schuppert, K. Petermann, and G. Burbach, "Low loss singlemode optical waveguides with large cross-section insilicon-on-insulator," *Electron. Lett.*, vol. 27, pp. 1486–1488, 1991.

[46] G. Cocorullo, F. G. D. Corte, I. Rendina, C. Minarini, A. Rubino, and E. Terzini, "Amorphous silicon waveguides and light modulators for integrated photonics realized by low-temperature plasma-enhanced chemical-vapor deposition," *Opt. Lett.*, vol. 21, no. 24, pp. 2002–2004, 1996.

[47] A. Harke, M. Krause, and J. Mueller, "Low-loss singlemode amorphous silicon waveguides," *Electron. Lett.*, vol. 41, no. 25, pp. 1377– 1379, 2005.

[48] G. T. Reed, G. Z. Mashanovich, W. R. Headley, B. Timotijevic, F. Y. Gardes, S. P. Chan, P. Waugh, N. G. Emerson, C. E. Png, M. J. Paniccia, A. Liu, D. Hak, and V. M. N. Passaro, "Issues associated with polarization independence in silicon photonics," *IEEE J. Sel. Topics Quantum Electron.*, vol. 12, no. 6, pp. 1335–1344, Nov.-dec. 2006.

[49] S. P. Chan, C. E. Png, S. T. Lim, G. T. Reed, and V. M. N. Passaro, "Singlemode and polarization-independent silicon-on-insulator waveguides with small cross section," *J. Lightwave Technol.*, vol. 23, no. 6, p. 2103, 2005.

[50] T. Baehr-Jones, M. Hochberg, G. Wang, R. Lawson, Y. Liao, P. Sullivan, L. Dalton, A. Jen, and A. Scherer, "Optical modulation and detection in slotted silicon waveguides," *Opt. Express*, vol. 13, no. 14, pp. 5216–5226, 2005.

[51] G. Roelkens, D. V. Thourhout, and R. Baets, "High efficiency grating coupler between silicon-on-insulator waveguides and perfectly vertical optical fibers," *Opt. Lett.*, vol. 32, no. 11, pp. 1495–1497, 2007.

[52] T. Shoji, T. Tsuchizawa, T. Watanabe, K. Yamada, and H. Morita, "Low loss mode size converter from 0.3 μm square si wire waveguides to singlemode fibres," *Electron. Lett.*, vol. 38, no. 25, pp. 1669–1670, 2002.

[53] V. R. Almeida, R. R. Panepucci, and M. Lipson, "Nanotaper for compact mode conversion," *Opt. Lett.*, vol. 28, no. 15, pp. 1302–1304, 2003.

[54] M. Fritze, J. Knecht, C. Bozler, C. Keast, J. Fijol, S. Jacobson, P. Keating, J. LeBlanc, E. Fike, M. Kessler, B.and Frish, and C. Manolatou, "3d mode converters for soi integrated optics," in *IEEE SOI Conference*, 2002.

[55] A. Sure, T. Dillon, J. Murakowski, C. Lin, D. Pustai, and D. Prather, "Fabrication and characterization of three-dimensional silicon tapers," *Opt. Express*, vol. 11, no. 26, pp. 3555–3561, 2003.

[56] S. Janz, B. Lamontagne, A. Delage, A. Bogdanov, D.-X. Xu, and K. Xu, "Single layer a-si grin waveguide coupler with lithographically defined facets," in *Group IV Photonics*, 2005.

[57] K. Shiraishi and C. Tsai, "A micro light-beam spot-size converter using a hemicylindrical grin-slab tip with high-index contrast," *J. Lightwave Technol.*, vol. 23, no. 11, pp. 3821–3826, 2005.

[58] H. Yoda, H. Ikedo, T. Ketsuka, A. Irie, K. Shiraishi, and C. Tsai, "A high-performance micro-grin-chip spot-size converter formed with focused ion beam," *IEEE Photon. Technol. Lett.*, vol. 18, no. 14, pp. 1554–1556, 2006.

[59] K. Shiraishi, H. Yoda, A. Ohshima, H. Ikedo, and C. S. Tsai, "A silicon-based spot-size converter between single-mode fibers and si-wire waveguides using cascaded tapers," *Appl. Phys. Lett.*, vol. 91, no. 14, p. 141120, 2007.

[60] A. Harke, T. Lipka, J. Amthor, O. Horn, M. Krause, and J. Muller, "Amorphous silicon 3-d tapers for si photonic wires fabricated with shadow masks," *IEEE Photon. Technol. Lett.*, vol. 20, no. 17, pp. 1452–1454, 2008.

[61] D. Marcuse, "Directional couplers made of nonidentical asymmetric slabs. part i: Synchronous couplers," *J. Lightwave Technol.*, vol. 5, no. 1, pp. 113–118, Jan 1987.

[62] P. Trinh, S. Yegnanarayanan, and B. Jalali, "Integrated optical directional couplers in silicon-on-insulator," *Electron. Lett.*, vol. 31, no. 24, pp. 2097–2098, Nov 1995.

[63] H. Yamada, T. Chu, S. Ishida, and Y. Arakawa, "Optical directional coupler based on si-wire waveguides," *IEEE Photon. Technol. Lett.*, vol. 17, no. 3, pp. 585–587, March 2005.

[64] L. Soldano and E. Pennings, "Optical multi-mode interference devices based on self-imaging: principles and applications," *J. Lightwave Technol.*, vol. 13, no. 4, pp. 615–627, Apr 1995.

[65] U. Fischer, T. Zinke, and K. Petermann, "Integrated optical waveguide switches in soi," *SOI Conference*, pp. 141–142, Oct 1995.

[66] Y. Zuo, R. Mao, Y. Zheng, X. Shi, L. Zhao, W. Shi, B. Cheng, J. Yu, and Q. Wang, "A si-based tunable narrow-band flat-top filter with multiple-step-type fabry-perot cavity structure," *IEEE Photon. Technol. Lett.*, vol. 17, no. 10, pp. 2134–2136, Oct. 2005.

[67] M. Iodice, G. Cocorullo, F. G. D. Corte, and I. Rendina, "Silicon fabry-perot filter for wdm systems channels monitoring," *Optics Communications*, vol. 183, no. 5-6, pp. 415 – 418, 2000.

[68] I. Kiyat, A. Aydinli, and N. Dagli, "High-q silicon-on-insulator optical rib waveguide racetrack resonators," *Opt. Express*, vol. 13, no. 6, pp. 1900–1905, 2005.

[69] J. Niehusmann, A. Vörckel, P. H. Bolivar, T. Wahlbrink, W. Henschel, and H. Kurz, "Ultrahigh-quality-factor silicon-on-insulator microring resonator," *Opt. Lett.*, vol. 29, no. 24, pp. 2861–2863, 2004.

[70] P. Dumon, W. Bogaerts, V. Wiaux, J. Wouters, S. Beckx, J. V. Campenhout, D. Taillaert, B. Luyssaert, P. Bienstman, D. V. Thourhout, and R. Baets, "Low-loss soi photonic wires and ring resonators fabricated with deep uv lithography," *IEEE Photon. Technol. Lett.*, vol. 16, no. 5, pp. 1328–1330, May 2004.

[71] V. R. Subramanian, R. G. DeCorby, J. N. McMullin, C. J. Haugen, and M. Belov, "Fabrication of aperiodic gratings on silicon-on-insulator (soi) rib waveguides using e-beam lithography," *Silicon-based and Hybrid Optoelectronics IV*, vol. 4654, no. 1, pp. 45–53, 2002.

[72] T. E. Murphy, J. T. Hastings, and H. I. Smith, "Fabrication and characterization of narrow-band bragg-reflection filters in silicon-on-insulator ridge waveguides," *J. Lightwave Technol.*, vol. 19, no. 12, p. 1938, 2001.

[73] T. Chu, H. Yamada, S. Ishida, and Y. Arakawa, "Reconfigurable optical add-drop multiplexer based on silicon nano-wire waveguides," *ECOC*, vol. 2, pp. 245–246 vol.2, Sept. 2005.

[74] D. Taillaert, F. V. Laere, M. Ayre, W. Bogaerts, D. V. Thourhout, P. Bienstman, and R. Baets, "Grating couplers for coupling between optical fibers and nanophotonic waveguides," *Jpn. J. Appl. Phys.*, vol. 45, no. 8A, pp. 6071–6077, 2006.

[75] G. J. Lee, J. Park, E. Kim, Y. Lee, K. Kim, H. Cheong, C. Yoon, Y.-D. Son, and J. Jang, "Microstructure of femtosecond laser-induced grating in amorphous silicon," *Opt. Express*, vol. 13, no. 17, pp. 6445–6453, 2005.

[76] L. Liao, A. Liu, S. Pang, and M. J. Paniccia, "Tunable bragg grating filters in soi waveguides," *Integrated Photonics Research*, p. IThE2, 2004.

[77] W. Bogaerts, R. Baets, P. Dumon, V. Wiaux, S. Beckx, D. Taillaert, B. Luyssaert, J. Van Campenhout, P. Bienstman, and D. Van Thourhout, "Nanophotonic waveguides in silicon-on-insulator fabricated with cmos technology," *J. Lightwave Technol.*, vol. 23, no. 1, pp. 401–412, Jan. 2005.

[78] D. W. Prather, S. Shi, J. Murakowski, G. J. Schneider, A. Sharkawy, C. Chen, and B. Miao, "Photonic crystal structures and applications: Perspective, overview, and development," *IEEE J. Sel. Topics Quantum Electron.*, vol. 12, no. 6, pp. 1416–1437, Nov.-dec. 2006.

[79] Z. Zhang, M. Dainese, L. Wosinski, S. Xiao, M. Qiu, M. Swillo, and U. Andersson, "Optical filter based on two-dimensional photonic crystal surface-mode cavity in amorphous silicon-on-silica structure," *Appl. Phys. Lett.*, vol. 90, no. 4, p. 041108, 2007.

[80] G. T. Reed and C. J. Png, "Silicon optical modulators," *Materials Today*, vol. 8, no. 1, pp. 40 – 50, 2005.

[81] A. Liu, L. Liao, D. Rubin, H. Nguyen, B. Ciftcioglu, Y. Chetrit, N. Izhaky, and M. Paniccia, "High-speed optical modulation based on carrier depletion in a silicon waveguide," *Opt. Express*, vol. 15, no. 2, pp. 660–668, 2007.

[82] J. Liu, D. Pan, S. Jongthammanurak, K. Wada, L. C. Kimerling, and J. Michel, "Design of monolithically integrated gesi electro-absorption modulators and photodetectors on a soi platform," *Opt. Express*, vol. 15, no. 2, pp. 623–628, 2007.

[83] J. Liu, M. Beals, A. Pomerene, S. Bernardis, R. Sun, J. Cheng, L. C. Kimerling, and J. Michel, "Waveguide-integrated, ultralow-energy gesi electro-absorption modulators," *Nature Photonics*, vol. 2, pp. 433 – 437, 2008.

[84] S. A. Clark, B. Culshaw, E. J. Dawnay, and I. E. Day, "Thermo-optic phase modulators in simox material," *Integrated Optics Devices IV*, vol. 3936, no. 1, pp. 16–24, 2000.

[85] G. Cocorullo, F. Della Corte, R. de Rosa, I. Rendina, A. Rubino, and E. Terzini, "Amorphous silicon-based guided-wave passive and active devices for silicon integrated optoelectronics," *IEEE J. Sel. Topics Quantum Electron.*, vol. 4, no. 6, pp. 997–1002, Nov.-Dec. 1998.

[86] E. Friedrich, M. Oberg, B. Broberg, S. Nilsson, and S. Valette, "Hybrid integration of semiconductor lasers with si-based single-mode ridge waveguides," *J. Lightwave Technol.*, vol. 10, no. 3, pp. 336–340, Mar 1992.

[87] T. Bestwick, "Asoc^{TM}-a silicon-based integrated optical manufacturing technology," in *IEEE Electronic Components & Technol. Conference*, May 1998, pp. 566–571.

[88] H. J. Heider, U.-P. Dahms, M. Mahnke, M. Bludszuweit, and J. Mueller, "Optical transceiver in integrated and micro-optics on silicon," in *Optoelectronic Integrated Circuits IV*, Y.-S. Park and R. T. Chen, Eds., vol. 3950, no. 1. SPIE, 2000, pp. 12–21.

[89] L. Colace, G. Masini, F. Galluzzi, G. Assanto, G. Capellini, L. D. Gaspare, E. Palange, and F. Evangelisti, "Metal–semiconductor–metal near-infrared light detector based on epitaxial ge/si," *Appl. Phys. Lett.*, vol. 72, no. 24, pp. 3175–3177, 1998.

[90] M. Morse, F. Dosunmu, E. Ginsburg, Y. Chetrit, and G. Sarid, "850 nm germanium photodetector performance," in *Group IV Photonics*, 2006, pp. 170–172.

[91] S. Fama, L. Colace, G. Masini, G. Assanto, and H.-C. Luan, "High performance germanium-on-silicon detectors for optical communications," *Appl. Phys. Lett.*, vol. 81, no. 4, pp. 586–588, 2002.

[92] G. Masini, L. Colace, and G. Assanto, "2.5 gbit/s polycrystalline germanium-on-silicon photodetector operating from 1.3 to 1.55 mu m," *Appl. Phys. Lett.*, vol. 82, no. 15, pp. 2524–2526, 2003.

[93] S. J. Koester, J. D. Schaub, G. Dehlinger, and J. O. Chu, "Germanium-on-soi infrared detectors for integrated photonic applications," *IEEE J. Sel. Topics Quantum Electron.*, vol. 12, no. 6, pp. 1489–1502, Nov.-dec. 2006.

[94] P. Kik, A. Polman, S. Libertino, and S. Coffa, "Design and performance of an erbium-doped silicon waveguide detector operating at 1.5 μm," *J. Lightwave Technol.*, vol. 20, no. 5, pp. 862–867, May 2002.

[95] J. D. B. Bradley, P. E. Jessop, and A. P. Knights, "Silicon waveguide-integrated optical power monitor with enhanced sensitivity at 1550 nm," *Appl. Phys. Lett.*, vol. 86, no. 24, p. 241103, 2005.

[96] Y. Liu and H. K. Tsang, "Nonlinear absorption and raman gain in helium-ion-implanted silicon waveguides," *Opt. Lett.*, vol. 31, pp. 1714–1716, 2006.

[97] M. W. Geis, S. J. Spector, M. E. Grein, R. T. Schulein, J. U. Yoon, D. M. Lennon, S. Deneault, F. Gan, F. X. Kaertner, and T. M. Lyszczarz, "Cmos-compatible all-si high-speed waveguide photodiodes with high responsivity in near-infrared communication band," *IEEE Photon. Technol. Lett.*, vol. 19, no. 3, pp. 152–154, Feb.1, 2007.

[98] P. M. Fauchet, "Light emission from si quantum dots," *Materials Today*, vol. 8, no. 1, pp. 26 – 33, 2005.

[99] L. Pavesi, "Routes toward silicon-based lasers," *Materials Today*, vol. 8, no. 1, pp. 18 – 25, 2005.

[100] W. L. Ng, M. A. Lourenco, R. M. Gwilliam, S. Ledain, G. Shao, and K. P. Homewood, "An efficient room-temperature silicon-based light-emitting diode," *Nature*, vol. 410, pp. 192–194, 2001.

[101] J. Michel, J. L. Benton, R. F. Ferrante, D. C. Jacobson, D. J. Eaglesham, E. A. Fitzgerald, Y.-H. Xie, J. M. Poate, and L. C. Kimerling, "Impurity enhancement of the 1.54-μm er[$^{3+}$] luminescence in silicon," *J. Appl. Phys.*, vol. 70, no. 5, pp. 2672–2678, 1991.

[102] H. Rong, R. Jones, A. Liu, O. Cohen, D. Hak, A. Fang, and M. Paniccia, "A continuous-wave raman silicon laser," *Nature*, vol. 433, pp. 725–728, 2005.

[103] A. Huang, C. Gunn, G.-L. Li, Y. Liang, S. Mirsaidi, A. Narasimha, and T. Pinguet, "A 10gb/s photonic modulator and wdm mux/demux integrated with electronics in 0.13μm soi cmos," in *IEEE Solid-State Circuits Conference*, Feb. 2006, pp. 922–929.

[104] C. Gunn, D. Guckenberger, T. Pinguet, D. Gunn, D. Eliyahu, B. Mansoorian, D. Van Blerkom, and O. Salminen, "A low phase noise 10ghz optoelectronic rf oscillator implemented using cmos photonics," in *IEEE Solid-State Circuits Conference*, Feb. 2007, pp. 570–622.

[105] B. Analui, D. Guckenberger, D. Kucharski, and A. Narasimha, "A fully integrated 20-gb/s optoelectronic transceiver implemented in a standard 0.13-μm cmos soi technology," *IEEE J. Solid-State Circuits*, vol. 41, no. 12, pp. 2945–2955, Dec. 2006.

[106] J. Fedeli, M. Migette, L. Di Cioccio, L. El Melhaoui, R. Orobtchouk, C. Seassal, P. RojoRomeo, F. Mandorlo, D. Marris-Morini, and L. Vivien, "Incorporation of a photonic layer at the metallizations levels of a cmos circuit," in *Group IV Photonics*, 2006, pp. 200–202.

[107] S. Selvaraja, E.Sleeckx, W. Bogaerts, M. Schaekers, P. Dumon, D. V. Thourhout, and R. Baets, "Low loss amorphous silicon photonic wire and ring resonator fabricated by cmos process," in *Proceedings ECOC*, 2007.

[108] S. Jiang and M. J. Digonnet, Eds., *Simulation and fabrication of amorphous silicon rib-type arrayed waveguide grating*, vol. 5723, no. 1. SPIE, 2005.

[109] F. Della Corte, M. Nigro, C. Summonte, F. Cantore, M. Gagliardi, and S. Rao, "Amorphous silicon based active photonic devices," in *Group IV Photonics*, 21-23 Sept. 2005, pp. 71–73.

[110] M. Iodice, G. Mazzi, and L. Sirleto, "Thermo-optical static and dynamic analysis of a digital optical switch based on amorphous silicon waveguide," *Opt. Express*, vol. 14, no. 12, pp. 5266–5278, 2006.

[111] S. Y. Chou, P. R. Krauss, and P. J. Renstrom, "Imprint of sub-25 nm vias and trenches in polymers," *Appl. Phys. Lett.*, vol. 67, no. 21, pp. 3114–3116, 1995.

[112] J. Haisma, M. Verheijen, K. van den Heuvel, and J. van den Berg, "Mold-assisted nanolithography: A process for reliable pattern replication," *Int. conf. on electron, ion, and photon beam technol. nanofabrication*, vol. 14, no. 6, pp. 4124–4128, 1996.

[113] M. D. Austin, H. Ge, W. Wu, M. Li, Z. Yu, D. Wasserman, S. A. Lyon, and S. Y. Chou, "Fabrication of 5 nm linewidth and 14 nm pitch features by

nanoimprint lithography," *Appl. Phys. Lett.*, vol. 84, no. 26, pp. 5299–5301, 2004.

[114] N. Chaix, S. Landis, C. Gourgon, S. Merino, V. Lambertini, G. Durand, and C. Perret, "Nanoimprinting lithography on 200mm wafers for optical applications," *Microelectronic Engineering*, vol. 84, pp. 880–884, 2007.

[115] M. Belotti, J. Torres, E. Roy, A. Pépin, Y. Chen, D. Gerace, L. C. Andreani, and M. Galli, "Replication of photonic crystals by soft ultraviolet-nanoimprint lithography," *J. Appl. Phys.*, vol. 99, no. 2, p. 024309, 2006.

[116] P. I. Borel, B. Bilenberg, L. H. Frandsen, T. Nielsen, J. Fage-Pedersen, A. V. Lavrinenko, J. S. Jensen, O. Sigmund, and A. Kristensen, "Imprinted silicon-based nanophotonics," *Opt. Express*, vol. 15, no. 3, pp. 1261–1266, 2007.

[117] A. M. Hynes, H. Ashraf, J. K. Bhardwaj, J. Hopkins, I. Johnston, and J. N. Shepherd, "Recent advances in silicon etching for mems using the ase^{TM} process," *Sensors and Actuators A*, vol. 74, no. 1-3, pp. 13–17, 1999.

[118] S. A. McAuley, H. Ashraf, L. Atabo, A. Chambers, S. Hall, J. Hopkins, and G. Nicholls, "Silicon micromachining using a high-density plasma source," *J. Phys. D: Appl. Phys.*, vol. 34, no. 18, pp. 2769–2774, 2001.

[119] H. G. Tompkins, *A User's Guide to Ellipsometry*. Academic Press, 1993.

[120] C. J. Fang, K. J. Gruntz, L. Ley, M. Cardona, F. J. Demond, G. Müller, and S. Kalbitzer, "The hydrogen content of a-ge:h and a-si:h as determined by ir spectroscopy, gas evolution and nuclear reaction techniques," *J. Non-Cryst. Solids*, vol. 35-36, no. Part 1, pp. 255 – 260, 1980.

[121] H. Shanks, C. J. Fang, L. Ley, M. Cardona, F. J. Demond, and S. Kalbitzer, "Infrared spectrum and structure of hydrogenated amorphous silicon," *physica status solidi (b)*, vol. 100, no. 1, pp. 43–56, 1980.

[122] T. I. Kamins, "Structure and properties of lpcvd silicon films," *J. Electrochem. Soc.*, vol. 127, no. 3, pp. 686–690, 1980.

[123] A. T. Voutsas and M. K. Hatalis, "Structure of as-deposited lpcvd silicon films at low deposition temperatures and pressures," *J. Electrochem. Soc.*, vol. 139, no. 9, pp. 2659–2665, 1992.

[124] "Silicon," *Natl. Bur. Stand. (U.S.) Monogr.*, vol. 25, 13, 35, 1976.

[125] L. Liao, D. R. Lim, A. M. Agarwal, X. Duan, K. K. Lee, and L. C. Kimerling, "Optical transmission losses in polycrystalline silicon strip waveguides: Effects of waveguide dimensions, thermal treatment, hydrogen passivation, and wavelength," *Journal of Electronic Materials*, vol. 29, no. 12, pp. 1380–1386, 2000.

[126] K. Morishita, "Refractive-index-profile determination of single-mode optical fibers by a propagation-mode near-field scanning technique," *J. Lightwave Technol.*, vol. 1, no. 3, pp. 445–449, Sep 1983.

[127] Q. Xu, V. R. Almeida, R. R. Panepucci, and M. Lipson, "Experimental demonstration of guiding and confining light in nanometer-sizelow-refractive-index material," *Opt. Lett.*, vol. 29, no. 14, pp. 1626–1628, 2004.

[128] R. Sun, P. Dong, N. ning Feng, C. yin Hong, J. Michel, M. Lipson, and L. Kimerling, "Horizontal single and multiple slot waveguides: optical transmission at $\lambda = 1550$ nm," *Opt. Express*, vol. 15, no. 26, pp. 17 967–17 972, 2007.

Abbreviations

AFM	atom force microscope
ARC	anti-reflective coating
ASE^{TM}	advanced silicon etch
a-Si	amorphous silicon
a-Si:H	hydrogenated amorphous silicon
BOE	buffered oxide etch
CMOS	complementary metal oxide semiconductor
CMP	chemical mechanical polishing
c-Si	crystalline silicon
CVD	chemical vapor deposition
DI-water	deionized water
DSP	double side polished
EPIC	electronic-photonic integrated circuit
F	finesse
FCA	free-carrier absorption
FSR	free-spectral range
FTIR	Fourier transform infrared spectroscopy
FWHM	full width at half maximum
HF	high frequency
ICP	inductively coupled plasma
IR	infrared
LF	low frequency
LPCVD	low pressure chemical vapor deposition
MFD	modal field diameter
MMI	multimode interference
MMSWG	multimode strip waveguide
MOS	metal oxide semiconductor
MZI	Mach - Zehnder interferometer
NA	numerical aperture

PECVD	plasma enhanced chemical vapor deposition
PhC	photonic crystal
poly-Si	poly crystalline silicon
PVD	physical vapor deposition
RF	radio frequency
RMS	root mean square
RTA	rapid thermal anneal
RTP	rapid thermal processing
SMRWG	monomode rib waveguide
SMSWG	monomode strip waveguide
SOI	silicon on insulator
SSP	single side polished
STS	Surface Technology Systems
TE	transversal electric
TM	transversal magnetic
UV	ultraviolet
WG	waveguide
XRD	x-ray diffraction